UC San Diego

UC San Diego Electronic Theses and Dissertations

Title

Grain Boundary Engineering in Li-ion Batteries and Ceramic Materials

Permalink

https://escholarship.org/uc/item/3zn0b82m

Author

Yan, Qizhang

Publication Date

2022

Peer reviewed|Thesis/dissertation

eScholarship.org Powered by the California Digital Library
University of California

UNIVERSITY OF CALIFORNIA SAN DIEGO

Grain Boundary Engineering in Li-ion Batteries and Ceramic Materials

A Dissertation submitted in partial satisfaction of the requirements
for the degree Doctor of Philosophy

in

Nanoengineering

by

Qizhang Yan

Committee in charge:

Professor Jian Luo, Chair
Professor Javier Garay
Professor Ping Liu
Professor Yu Qiao
Professor Kesong Yang

2022

Copyright

Qizhang Yan, 2022

All rights reserved.

The Dissertation of Qizhang Yan is approved, and it is acceptable in quality and form for publication on microfilm and electronically.

University of California San Diego

2022

TABLE OF CONTENTS

LIST OF FIGURES

ACKNOWLEDGEMENTS

I would like to thank my PhD advisor Professor Jian Luo. He has been a wonderful supervisor in guiding my PhD journey, overseeing my research topics, and providing all the resources that I need. I would also like to thank all my committee members, Prof. Ping Liu, Prof. Javier Garay, Prof. Yu Qiao, and Prof. Kesong Yang for their valuable advice and time.

Secondly, I would like to acknowledge the support from my group members, Shu-Ting Ko, Dawei Zhang, Dr. Chongze Hu, and Yumin Zhao. I am also thankful to Dr. Jiuyuan Nie for his training in electron microscopy and sintering experiment setups.

Lastly, I would like to thank my family members and my partner, Yiming Chen for their love, support, and constant encouragement.

Chapter 1, in part, is a reprint of the materials "Thermodynamics-driven interfacial engineering of alloy-type anode materials", Q. Yan, S. Ko, A. Dawson, D. Agyeman-Budu, G. Whang, Y. Zhao, M. Qin, B. Dunn, J. Weker, S. Tolbert, and J. Luo, as it appears in Cell Reports Physical Science, 2022, 3, 1.

Chapter 2, in full, is a reprint of the material "Thermodynamics-driven interfacial engineering of alloy-type anode materials", Q. Yan, S. Ko, A. Dawson, D. Agyeman-Budu, G. Whang, Y. Zhao, M. Qin, B. Dunn, J. Weker, S. Tolbert, and J. Luo, as it appears in Cell Reports Physical Science, 2022, 3, 1. The dissertation author was the primary investigator and author of this paper.

Chapter 3, in full, is a reprint of the material "Cryogenic Milling Method to Fabricate Nanostructured Anodes", Q. Yan, S. Ko, Y. Zhao, G. Whang, A. Dawson, S. Tolbert, B. Dunn,

and J. Luo, as it appears in ACS Applied Energy Materials, 2020, 3, 11. The dissertation author was the primary investigator and author of this paper.

Chapter 4, in full, is a reprint of the material “Electric-Field-Assisted Bi Migration in Bi_2O_3-doped ZnO Polycrystalline Specimens”, coauthored with J. Luo. It is currently being prepared for submission for publication of the material. The dissertation author was the primary researcher and author of this material.

Chapter 5 contains unpublished material coauthored with J. Luo. The dissertation author was the primary author of this chapter.

VITA

2017 Bachelor of Science in Chemical Engineering, University of California San Diego

2018 Master of Science in Nanoengineering, University of California San Diego

2022 Doctor of Philosophy in Nanoengineering, University of California San Diego

PUBLICATIONS

(1) **Yan, Q**.; Ko, S.-T.; Dawson, A.; Agyeman-Budu, D.; Whang, G.; Zhao, Y.; Qin, M.; Dunn, B. S.; Weker, J. N.; Tolbert, S. H.; others. Thermodynamics-Driven Interfacial Engineering of Alloy-Type Anode Materials. *Cell Reports Phys. Sci.* **2022**, *3* (1), 100694.

(2) **Yan, Q**.; Ko, S.-T.; Zhao, Y.; Whang, G.; Dawson, A.; Tolbert, S. H.; Dunn, B. S.; Luo, J. Cryogenic Milling Method to Fabricate Nanostructured Anodes. *ACS Appl. Energy Mater.* **2020**, *3* (11), 11285--11292. https://doi.org/10.26434/chemrxiv.13128026.v1.

(3) **Yan, Q**.; Whang, G.; Wei, Z.; Ko, S.-T.; Sautet, P.; Tolbert, S. H.; Dunn, B. S.; Luo, J. A Perspective on Interfacial Engineering of Lithium Metal Anodes and Beyond. *Appl. Phys. Lett.* **2020**, *117* (8), 80504.

(4) Whang, G.; **Yan, Q**.; Li, D.; Wei, Z.; Butts, D.; Sautet, P.; Luo, J.; Dunn, B. Avoiding Dendrite Formation by Confining Lithium Deposition underneath Li--Sn Coatings. *J. Mater. Res.* **2021**, 1–15.

(5) Shivakumar, S.; Qin, M.; Zhang, D.; Hu, C.; **Yan, Q**.; Luo, J. A New Type of Compositionally Complex M5Si3 Silicides: Cation Ordering and Unexpected Phase Stability. *Scr. Mater.* **2022**, *212*, 114557.

(6) Vincent, R. C.; Luo, Y.; Andrews, J. L.; Zohar, A.; Zhou, Y.; **Yan, Q**.; Mozur, E. M.; Preefer, M. B.; Weker, J. N.; Cheetham, A. K.; others. High-Rate Lithium Cycling and Structure Evolution in Mo4O11. *Chem. Mater.* **2022**.

(7) Kim, S. S.; Agyeman-Budu, D. N.; Zak, J. J.; Dawson, A.; **Yan, Q**.; Cában-Acevedo, M.; Wiaderek, K. M.; Yakovenko, A. A.; Yao, Y.; Irshad, A.; others. Promoting Reversibility of Multielectron Redox in Alkali-Rich Sulfide Cathodes through Cryomilling. *Chem. Mater.* **2022**.

(8) Holoubek, J.; **Yan, Q**.; Liu, H.; Hopkins, E. J.; Wu, Z.; Yu, S.; Luo, J.; Pascal, T. A.; Chen, Z.; Liu, P. Oxidative Stabilization of Dilute Ether Electrolytes via Anion Modification. *ACS Energy Lett.* **2022**, *7*, 675–682.

(9) Nie, J.; Hu, C.; **Yan, Q**.; Luo, J. Discovery of Electrochemically Induced Grain Boundary Transitions. *Nat. Commun.* **2021**, *12* (1), 1–10.

(10) Wang, D.; **Yan, Q**.; Li, M.; Gao, H.; Tian, J.; Shan, Z.; Wang, N.; Luo, J.; Zhou, M.; Chen, Z. Boosting Cycling Stability of Ni-Rich Layered Oxide Cathode by Dry Coating of Ultrastable Li3V2 (PO4) 3 Nanoparticles. *Nanoscale* **2021**.

(11) Liu, H.; Holoubek, J.; Zhou, H.; Chen, A.; Chang, N.; Wu, Z.; Yu, S.; **Yan, Q**.; Xing, X.; Li, Y.; others. Ultrahigh Coulombic Efficiency Electrolyte Enables Li|| SPAN Batteries with Superior Cycling Performance. *Mater. Today* **2021**, *42*, 17–28.

(12) Qin, M.; **Yan, Q**.; Wang, H.; Vecchio, K. S.; Luo, J. High-Entropy Rare Earth Tetraborides. *J. Eur. Ceram. Soc.* **2021**, *41* (4), 2968–2973.

(13) Qin, M.; **Yan, Q**.; Liu, Y.; Wang, H.; Wang, C.; Lei, T.; Vecchio, K. S.; Xin, H. L.; Rupert, T. J.; Luo, J. Bulk High-Entropy Hexaborides. *J. Eur. Ceram. Soc.* **2021**, *41* (12), 5775–5781.

(14) Gonzalez, M. S.; Wu, Z.; Holoubek, J.; **Yan, Q**.; Liu, H.; Liu, P. Mitigating Internal Shorting to Enhance Battery Safety with Gradient-Conductivity Cathodes. *J. Power Sources* **2021**, *511*, 230412.

(15) Qin, M.; **Yan, Q**.; Liu, Y.; Luo, J. A New Class of High-Entropy M3B4 Borides. *J. Adv. Ceram.* **2021**, *10* (1), 166–172.

(16) Gonzalez, M. S.; **Yan, Q**.; Holoubek, J.; Li, M.; Wu, Z.; Zhou, H.; Kim, S.; Liu, H.; Jung, B.-Y.; Lee, S.; others. Reversible Switching of Battery Internal Resistance Using Iongate Separators. *Adv. Funct. Mater.* **2021**, 2102198.

(17) Holoubek, J.; **Yan, Q**.; Liu, H.; Wu, Z.; Xing, X.; Zhou, H.; Luo, J.; Chen, Z.; Liu, P. Low-Cost Li||SPAN Batteries Enabled by Sustained Additive Release. *ACS Appl. Energy Mater.* **2021**, *4* (7), 6422–6429.

(18) Qin, M.; **Yan, Q**.; Wang, H.; Hu, C.; Vecchio, K. S.; Luo, J. High-Entropy Monoborides: Towards Superhard Materials. *Scr. Mater.* **2020**, *189*, 101–105.

(19) Liu*, H.; Zhu*, Z.; **Yan, Q**.; Yu, S.; He, X.; Chen, Y.; Zhang, R.; Ma, L.; Liu, T.; Li, M.; others. A Disordered Rock Salt Anode for Fast-Charging Lithium-Ion Batteries. *Nature* **2020**, *585* (7823), 63–67.

(20) Lei, Y.; Chen, Y.; Zhang, R.; Li, Y.; **Yan, Q**.; Lee, S.; Yu, Y.; Tsai, H.; Choi, W.; Wang, K.; Luo, Y.; Gu, Y.; Zheng, X.; Wang, C.; Wang, C.; Hu, H.; Li, Y.; Qi, B.; Lin, M.; Zhang,

Z.; Dayeh, S. A.; Pharr, M.; Fenning, D. P.; Lo, Y.-H.; Luo, J.; Yang, K.; Yoo, J.; Nie, W.; Xu, S. A Fabrication Process for Flexible Single-Crystal Perovskite Devices. *Nature* **2020**, *583* (7818), 790–795.

(21) Gonzalez, M. S.; **Yan, Q**.; Holoubek, J.; Wu, Z.; Zhou, H.; Patterson, N.; Petrova, V.; Liu, H.; Liu, P. Draining Over Blocking: Nano-Composite Janus Separators for Mitigating Internal Shorting of Lithium Batteries. *Adv. Mater.* **2020**, *32* (12), 1906836.

(22) Gao, H.; **Yan, Q**.; Xu, P.; Liu, H.; Li, M.; Liu, P.; Luo, J.; Chen, Z. Efficient Direct Recycling of Degraded LiMn2O4 Cathodes by One-Step Hydrothermal Relithiation. *ACS Appl. Mater. \& Interfaces* **2020**, *12* (46), 51546–51554.

(23) Liu, H.; Yue, X.; Xing, X.; **Yan, Q**.; Huang, J.; Petrova, V.; Zhou, H.; Liu, P. A Scalable 3D Lithium Metal Anode. *Energy Storage Mater.* **2019**, *16*, 505–511.

(25) Liu, H.; Wang, X.; Zhou, H.; Lim, H.-D.; Xing, X.; **Yan, Q**.; Meng, Y. S.; Liu, P. Structure and Solution Dynamics of Lithium Methyl Carbonate as a Protective Layer for Lithium Metal. *ACS Appl. Energy Mater.* **2018**, *1* (5), 1864–1869.

ABSTRACT OF THE DISSERTATION

Grain Boundary Engineering in Li-ion Batteries and Ceramic Materials

by

Qizhang Yan

Doctor of Philosophy in Nanoengineering

University of California San Diego, 2022

Professor Jian Luo, Chair

Alloy-type anodes are promising next-generation electrodes for Li-ion batteries because of their high specific capacity, but the severe volume expansion causes fast capacity decay. Here, two methods were explored to improve alloy-type anodes. First, a thermodynamically driven grain boundary engineering was proposed as a potential strategy. SnSb with Bi addition fabricated through ball milling and annealing was selected as a model system. The Bi-doped SnSb demonstrated improved cycling performance with < 1% porosity. Transmission electron microscopy shows grain boundaries Bi segregation, and thermodynamic modeling further

indicates the stabilization of a nanoscale liquid-like interfacial phase. In situ X-ray microscopy shows the crack suppression effect for the Bi-doped sample, suggesting a potential grain boundary sliding as a stress relief mechanism. Second, cryogenic milling was demonstrated as a novel method to engineer alloy-type anodes. This process can suppress cold welding, exfoliate bulk graphite into multilayer graphene, and evenly disperse them between the grains to form nanostructured electrodes. Based on the cross-section electron microscopy and X-ray microscopy, the dispersed graphene between the nanosized grains can effectively alleviate the volume expansion upon lithiation. Compared to the traditional ball milling methods under room temperature, the cryomilled SnSb-C composite anode showed improved cycling stability and rate capability.

For ceramic processing methods, electric field assisted sintering process can have a lower sintering temperature and faster sintering time compared to conventional sintering. For the second part of the thesis, nonthermal electric field effects on ZnO polycrystalline specimen was investigated. In undoped ZnO, electric field can induce defect polarization and subsequently alter the grain boundary structure. We also demonstrated the possibility of creating and controlling graded microstructure via electric fields. In Bi_2O_3-doped ZnO, electric field can drive the migration of Bi-rich secondary liquid phase.

In summary, the first part of the dissertation introduces grain boundary engineering and cryogenic milling as two novel approaches to improve alloy-type battery electrodes. The second part of the dissertation investigated electric field effects on ceramic microstructure evolution. The feasibility of tailoring ceramic microstructure with electric field was demonstrated.

Chapter 1. Introduction

Grain Boundary and Nanostructure Engineering for Alloy-Type Anodes

Lithium-ion batteries (LIB) have become one of the main energy storage solutions for our modern society.[1,2] However, the current generation batteries cannot satisfy the fast-growing demand for energy density. The theoretical capacity of graphite, 372 mAh/g or 756 Ah/L, is one of the limitations to achieving high battery energy density, and this drives researchers to study alternative options. Li-alloying reactions with various metal and intermetallic compounds (such as Si, Sn, and SnSb) have attracted recent research attention because of their high specific capacities.[3,4] However, the cycling stability of alloy-type anodes is typically poor due to the high volumetric changes during lithiation and delithiation. For example, Sn can expand by more than 300% after complete lithiation.[5] During the lithiation process, the expanded lithiated phase from the particle surface generates high compressive stress on large particles.[6,7] For micron-sized Sn particles, the surface hoop tension can cause crack nucleation and propagation. During the delithiation process, void channels were also found to form within the particle through percolation dissolution.[8–10] Electrolyte decomposition can repeatedly occur on the newly exposed electrode surfaces, which leads to continuous solid electrolyte interphase (SEI) growth.[11] Fractured fragments of active material can also become electrically isolated, causing capacity decay.

To overcome these challenges, various strategies have been proposed in past studies, including carbon/metal composites,[12–15] nanoporous structures,[5,16,17] novel binders/electrolyte additives,[18–20] and surface coatings[21–23]. For cycling stability improvements, a second metal species can be introduced. For example, SnSb lithiates via a two-step reaction: Sb first reacts with Li^+ at ~0.8 V to form a Li_3Sb matrix, then Sn starts to lithiates at 0.7 V. The two-step reaction can

alleviate the strain upon lithiation,[24] but the micrometer-sized SnSb can still crack during cycling, resulting in fast irreversible capacity decay.[25]

Kinetically controlled interfacial engineering, particularly various surface coating methods, have been widely used to improve alloy electrode cycling stability.[3] Generally, coatings can act as a barrier to stabilize the electrochemical interface. For example, Kohandehghan *et al.* [26] discovered 3-nm Sn coating on Si nanowires made by physical vapor deposition can improve cycling stability. The compressive stress from the lithiated Sn coating can confine the radial expansion of the Si nanowires. Ye *et al.* [27] showed that atomic layer deposition of Al_2O_3 and TiO_2 on Si micropillars led to thinner SEI and enhanced structural stability. To date, most interfacial engineering studies focus on surface modification, utilizing kinetically controlled coatings. In contrast, grain boundary (GB) engineering has not been widely investigated. Moreover, thermodynamically driven interfacial engineering has emerged as a new route to tailor batteries,[28] which has not yet been applied to alloy-type anodes.

In Chapter 2, grain boundary engineering on alloy-type anodes was explored to improve high-volume expansion anodes. More specifically, we report a thermodynamically driven grain boundary engineering method to improve alloy-type anodes via the spontaneous formation of 2D interfacial phases (complexions). Notably, the 2.8 at% Bi-doped SnSb achieves improved cycling stability and rate capability, even though it is 99% dense and has a mean crystallite size 2.7× larger than the undoped SnSb reference sample. Cryogenic transmission electron microscopy reveals Bi segregation at grain boundaries. Thermodynamic modeling further suggests the stabilization of a nanoscale liquid-like interfacial phase. Synchrotron transmission X-ray microscopy shows the suppressed intergranular cracking upon cycling with Bi addition. It suggests that the liquid-like interfacial phase serves as a stress relief mechanism for the high volumetric expansion anode via

improved grain boundary sliding and Coble creep, akin to room-temperature superplasticity observed in Sn-Bi.

In Chapter 3, we report cryogenic milling as a new and facile route to fabricate nanostructured battery electrode materials. SnSb intermetallic compound with 1.2 wt% bulk graphite were picked as the model system to test the benefits of this method. Cryogenic milling is able to suppress cold-welding of the grains, exfoliate graphite into multi-layer graphene, and effectively forming a carbon host structure for SnSb. Transmission electron microscopy revealed the refined grains and the evenly distributed multi-layer graphene between the SnSb. This electrode structure can stabilize the nanostructure upon lithiaion. The cryomilled carbon composite electrode demonstrated a volumetric capacity of 1842 Ah/L, averaged Coulombic efficiency of 99.6%, and capacity retention of 90% over 100 cycles. The cryomilled electrode materials showcased an improved cycling stability compared to the conventional ball milled electrodes.

Electric field effects on ceramic microstructure evolution

Sintering, where the specimen microstructure and properties are dominated by the temperature and time, is one of the main ceramic fabrication processes for thousands of years.[29] For the development of sintering technology, lower sintering temperature and shorter sintering time are always preferred, as these can increase the production rate and decrease the energy consumption. In recent years, factors such as external applied pressure and electric field have a growing importance in ceramic fabrication.[30–32] Spark plasma sintering (SPS), or field-assisted sintering technology (FAST) was developed back in 1960s,[33] where powder is placed in a conducting die under applied uniaxial pressure being rapidly heated with current (Joule heating of the die).[34–36] SPS/FAST is being demonstrated as a versatile consolidation method with generally decreased sintering time and temperature.[37,38] More recently, flash sintering was developed by Raj

and colleagues in 2010 where electric field/current is applied onto the specimen to trigger rapid densification in 5 – 10 s at low furnace temperature,[39] and a broad range of ceramic materials was demonstrated to be compatible with this method. In general, the external applied electric field enable fast kinetics and low temperature process, which makes ceramics sintering become more energy-saving and cost-effective.

Electric field can also have many nonthermal effects onto the specimen. For flash sintering, researchers have found electric field can induce anisotropic lattice expansion,[40] produce metastable phase,[41] and facilitate phase transformation[42] in selected systems. Aside from faster sintering, electric field can also induce microstructure evolution when applied on dense specimens. Chen and colleagues have found the residual pores could migrate in the opposite direction of the applied electric field in 8 mol% Y2O3-stabilized ZrO2 (8YSZ).[43,44] Asymmetrical grain growth has also been observed in various systems, such as 3YSZ,[45] $SrTiO_3$,[46] and ZnO [47,48] after annealing under electric field. On the atomic level, Luo and colleagues have recently discovered that the applied electric current can change the microstructural evolution of Bi_2O_3-doped ZnO through an electrochemically induced grain boundary transition.[48] Specifically, when the electric field is applied onto the sample, electrochemical reduction can occur on the negative electrode side and cause a grain boundary disorder-to-order transition to increase grain boundary diffusivities and induce abnormal grain growth. These interesting electric field effects can potentially enable new methods to tailor ceramic microstructure and grain boundaries.

In Chapter 4, we show that in Bi_2O_3-doped ZnO polycrystalline samples, electric field can drive the migration of bismuth oxide liquid phase toward the negative electrode. After sufficiently long annealing under electric field, the positive electrode side becomes Bi-free based on the low-magnification scanning electron microscopy and nanoscale aberration-corrected electron

microscopy. Preferential Bi migration along ZnO grain boundaries due to field-induced electrochemical potential gradient was proposed.

In Chapter 5, we demonstrate the feasibility of creating and controlling graded microstructures through the applied electric fields. With aberration-corrected electron microscopy, spatially resolved photoluminescence spectroscopy mapping, defects chemistry calculation, and first-principles calculations, we found electric field can induce defects polarization in ZnO and subsequently cause a grain boundary oxidation reaction on the anode side to increase grain boundary mobilities. Consequently, enhanced grain growth takes place from the anode side and forming a uniform grain size gradient across the sample. This work brings fundamental knowledge on both GB complexion (phase-like) transitions and electric field effects on microstructure, thereby pointing to a new direction of physical properties control via electrochemically induced GB transformation.

Chapter 2. Thermodynamics-driven interfacial engineering of alloy-type anode materials

Introduction

Here, we use the GB segregation of Bi and the associated spontaneous formation of a liquid-like interfacial phase to improve the performance SnSb Li-ion battery anodes. Bi was selected as the GB modification element with the following considerations: (1) The Sn-Sb-Bi ternary system has limited solubility of Bi in SnSb,[49,50] suggesting GB segregation of Bi. (2) Sn-Bi alloys have been reported to show superplasticity, with stable elongation up to ~1950% under tensile stress at room temperature.[51,52] We hypothesize that Bi-segregated SnSb GBs can stabilize the grain structure upon cycling as well as enabling stress release through GB sliding and Coble creep in a mechanism akin to the room-temperature superplasticity observed in Sn-Bi.[51,52] We added 2.8 at% (5 wt%) Bi to SnSb and confirmed the Bi segregation at SnSb GBs using cryogenic scanning transmission electron microscopy (cryo-STEM). Notably, this method can substantially improve the SnSb cycling stability and rate capability, even though the addition of Bi leads to dense micrometer-sized secondary particles with only 1% porosity, thereby pointing to a new direction of thermodynamics driven interfacial engineering.

Results

Thermodynamics driven interfacial engineering can be achieved via a facile ball milling and annealing method. Samples with 48.6 at% Sn, 48.6 at% Sb, and 2.8 at% of Bi were first planetary ball milled for 8 hours, and then annealed at 250 °C under Ar for 3 hours. A benchmark SnSb specimen was processed using the same method, but without Bi, for comparison. Supplementary Figure 2.6 b shows the XRD patterns of the SnSb and SnSb+Bi alloy anodes. The diffraction peaks could be indexed with SnSb (ICSD-154085) in the $R\bar{3}m$ space group for both samples. Since only 2.8 at% of Bi was added, diffraction peaks from Bi could not be observed in

the SnSb+Bi specimen. The solid solubility limit of Bi in SnSb is < 2 at% at room temperature;[49,50] thus, the extra Bi should be located at GBs and triple-grain junctions.

The averaged as-synthesized (secondary) particle sizes of SnSb and SnSb+Bi were both about 3 μm, as shown in Figure 2.1 a, d, and Supplementary Figure 2.7. We note that each of the secondary particle consisted of many crystalline grains and a small fraction of pores. Figure 2.1 b, e, and Supplementary Figure 2.9 show cryo-STEM images of SnSb and SnSb+Bi. The SnSb sample showed an averaged grain size of 32 ± 12 nm and ~6% porosity (Supplementary Figure 2.8 b, c). In contrast, the sample with Bi showed an averaged grain size of 81 ± 12 nm (Supplementary Figure 2.8 f), which was more than doubled the grain size of the undoped SnSb annealed under the same conditions. Moreover, the SnSb+Bi sample showed less porosity (only ~1%), as shown in Supplementary Figure 2.8 e. Overall, the addition of 2.8 at% Bi led to a ~2.7× increase in grain size with a substantially reduced porosity, while the same secondary particle size of 2 μm and morphology were maintained. These differences can be explained by the presence of a Bi-enriched liquid interfacial phase at the annealing temperature of 250 °C (Figure 2.10), which led to liquid-phase sintering and grain growth.

Given the low melting point of the Bi-rich interfacial phase, cryogenic STEM was used to prevent/reduce damage of specimens by electron beam at high magnifications. The specimens were kept at approximately -170°C during cryo-STEM imaging. We note that the calculated phase diagram based on NIST database[53] (Figure 2.18) suggests no phase transformation for SnSb + 2.8 at. % Bi below room temperature. Moreover, we believe that the Bi-enriched liquid-like interfacial structure can be quenched to the cryogenic temperature for STEM characterization. For the SnSb+Bi sample, bright contrast was observed at GBs in the high-angle annular dark-field image (HAADF) shown in Figure 2.1 e. The Z contrast can be correlated to atomic number in HAADF;

therefore, Figure 2.1 e indicates Bi segregation at GBs. In comparison, such bright contrast was not observed at the SnSb GBs (Figure 2.1 b). Note that grain boundaries exhibit different contrasts in Figure 2.1 e. This is because the five macroscopic (crystallographic) degrees of freedom of the grain boundaries result in significant boundray-to-boundary variation in a polycrystal. In addition, the boundaries can be at different angles with the electron beam in STEM, thereby affecting their contrasts and apparent widths in the projected images.

To quantitatively evaluate the GB segregation at 250 °C, a dense SnSb pellet with 2.8 at% of Bi was fabricated. This dense pellet allows the sample to have larger grain sizes, which are needed for quantitative GB elemental characterization in an edge-on geometry in STEM, while maintaining the same heat treatment temperature profile used to produce the electrode powder. The high-resolution bright-field (BF) image in Figure 2.2 a shows an interplanar spacing of 0.307 nm for both grains, which corresponds to the $(01\bar{1})$ planes of SnSb. Dark contrast was observed in at the GB the BF image, indicating Bi segregation at the SnSb GB (Figure 2.2 a and 2d). Cryo-STEM EDS was also carried out to determine the GB element composition. As shown in Figure 2.2 c, the EDS acquisition area was placed between two SnSb grains that have different zone axis. Figure 2.2 d, e, f shows the atomic percentage mapping of Sn, Sb, and Bi, respectively. There are decreases in intensities for Sn and Sb at the GB and obvious increased contrast for Bi at GB. Cryo-STEM EDS maps of three other GBs randomly selected from the dense SnSb+Bi pellet are shown in Supplementary Figure 2.20. All three GBs showed Bi enrichments. The composition of Sn, Sb, and Bi was extracted from the EDS elemental map as shown in Figure 2.2 g. Bulk SnSb+Bi grain composition was measured to be 48.1 at% Sn, 49.3 at% Sb, and 2.6 at% Bi (Supplementary Figure 2.17). The composition of the bulk grain was then set as the reference, and atomic composition change was plotted against the distance from the GB. Bi composition increased by ~15% at the

GB compared to bulk regions, while Sn and Sb decreased by ~ 5% and ~10%, respectively. The chemical width (full width half maximum) of the Bi-rich interfacial phase measured from EDS profile was 0.9 ± 0.1 nm thick (Figure 2.2 e). The nominal composition at the center the GB was measured to have 44.6 at% Sn, 38.9 at% Sb, and 16.5 at% Bi. However, this measured elemental composition has some contributions from the bulk grains due to the beam smearing effects and slight deviation from the exact edge-on condition. Thus, the GB core is likely more enriched with Bi (and more depleted with Sb).

Calculation of phase diagram (CALPHAD) simulations based on a NIST database[53] (Supplementary Figure 2.10) suggest the formation of a small fraction of (<3 at%) a Bi-enriched liquid phase in the SbSn+Bi materials at the annealing temperature of 250 °C (Figure 2.2 h; Supplementary Figure 2.10 c). This bulk liquid phase vanishes at the solidus temperature T_S = ~172 °C via a ternary invariant reaction: SnSb + Liquid → $(Bi, Sb)_{Rhombo}$ + $(Sn)_{BCT}$. This bulk liquid phase is enriched in Bi and depleted in Sb (43.8 at% Bi and 1.4 at% Sb at T_S); this is coincident with the observed GB composition (Figure 2.2 g), thereby suggesting that at least the GB composition is "liquid-like". Further calculations using an interfacial thermodynamic model taken from prior studies[54–58] suggested nanoscale, Bi-enriched, liquid-like, interfacial phase can be stabilized below the bulk solidus temperature (with the interfacial width scaled by the computed λ_0 values in the Figure 2.2 h). This model will be introduced in the Discission section and further elaborated in the Supplementary Note. Such a liquid-like interfacial structure can presumably promote GB sliding and Coble creep to mitigate cracking during cycling, as we will discuss later.

Electrochemical Performance

Annealed SnSb and SnSb+Bi powder after ball milling was first examined using galvanostatic cycling at a current density of 100 mA/g, as shown in Supplementary Figure 2.6 a.

The SnSb electrode showed severe capacity decay and only retained 26% capacity after 40 cycles. The Coulombic efficiency also quickly decays to 94% after 20 cycles, indicating poor cycling stability and sustained irreversible reactions. After 2.8 at% Bi was added to the SnSb, the capacity retention increased to 84% after 40 cycles with an averaged Coulombic efficiency of 97.8 ± 0.2%. This demonstrates that the addition of small amounts of Bi to SnSb can significantly improve electrode cycling performance.

The cycling performance of the SnSb+Bi anodes can be further improved. Recent research on alloy-type anodes has shown that a carbon composite structure can enhance cycling stability.[59,60] Building on those results, 6.2 wt% of graphite was planetary ball milled with both SnSb and SnSb+Bi to fabricate carbon composite anodes, [SnSb]-C and [SnSb+Bi]-C. The composite anodes were also annealed at 250 °C for 3 hours. Figure 2.3 a and Supplementary Figure 2.18 show the cycling stability of the carbon composite electrodes. The [SnSb]-C composite delivered a capacity of 60 ± 40 mAh/g after 200 cycles, retaining only around 9% of its initial charge capacity. In contrast, the [SnSb+Bi]-C composite demonstrated improved cycling stability. A capacity of 570 ± 4 mAh/g was maintained after 200 cycles, which corresponds to around 86% capacity retention. Figure 2.3 b and c compare the charge and discharge curves of [SnSb]-C and [SnSb+Bi]-C composite anodes. The first cycle discharge capacity for both electrodes are around 835 mAh/g, which includes the initial irreversible capacity from the formation of the SEI layer. Severe capacity decay and voltage hysteresis was observed for the SnSb carbon composite anode. In comparison, the [SnSb+Bi]-C sample showed almost no capacity decay after 150 cycles. The rate capabilities of the [SnSb]-C and [SnSb+Bi]-C carbon composite samples are shown in Figure 2.3 d. At a higher current density of 200 mA/g, 500 mA/g, and 1 A/g, the [SnSb+Bi]-C sample demonstrated charge capacities of 585 mAh/g, 520 mAh/g, and 410 mAh/g, respectively, which

corresponds to 89%, 79%, and 62% retention of the 100 mA/g capacity, respectively. In contrast, the [SnSb]-C sample showed decreased charge capacities of 558 mAh/g, 473 mAh/g, and 270 mAh/g, respectively, which corresponds to 85%, 72%, and 41% retention of the 100 mA/g capacity.

To further study the reaction kinetics of the two electrodes, cyclic voltammetry (CV) profiles were compared for 5 cycles at a sweep rate of 0.1 mV/s (indicated by the blue lines in Figure 2.3 e and f). During the first CV cycle, a strong reduction peak at ~0.5 V was observed for both electrodes. This peak is attributed to the formation of the SEI layer, as well as the lithiation reactions of SnSb to form Li_3Sb, Li_2Sn_5, and LiSn. This first cycle peak shift and convolution due to SEI formation was also reported in previous studies of the Sn and Sb based systems.[61–64] The redox reactions of SnSb can be identified from Cycle 2 to Cycle 5, which are labeled as I – V in the CV plot. Based on the phase diagram and recent studies,[3,65–68] lithiation reactions lead to the formation of (I) Li_3Sb and Sn, (II) Li_2Sn_5, (III) LiSn, (IV) Li_5Sn_2, and (V) $Li_{22}Sn_5$ in a sequence. Upon de-lithiation, a series of reactions lead to the formation of (V') Li_5Sn_2, (IV') LiSn, (III') Li_2Sn_5, (II') Sn, (I'-1) SnSb, and (I'-2) Sb. The detailed reaction formulae are shown in Figure 2.22. In Figure 2.3 f, the [SnSb]-C electrode showed a significant current decay with increasing cycle number, indicating increased irreversible capacity upon cycling. In comparison, the redox peak currents for the [SnSb+Bi]-C electrode in Figure 2.3 e were primarily unchanged from Cycle 1 to 5, showing improved cycling stability. When the scan rate increased from 0.1 mV/s to 0.8 mV/s (shown in Supplementary Figure 2.22), the peak shape of the [SnSb+Bi]-C electrode was preserved. At 0.8 mV/s, the peak separation of the redox couple I – I' for the [SnSb+Bi]-C electrode was 0.66 V, which was noticeable smaller than the [SnSb]-C electrode (0.78 V). This suggests a faster reaction kinetics after Bi addition.[69,70]

Overall, SnSb+Bi anodes showed significantly enhanced cycling stability and rate capability, in comparison to the pure SnSb. The carbon composite version of [SnSb+Bi]-C achieved superior performance with ~86% capacity retention after 200 cycles at 100 mA/g. This is a notable (and somewhat surprising) result, given that Bi doped SnSb is denser (with only 1% porosity inside the particle) than the pure SnSb and its mean primary grain size is 2.7× larger (~81 nm *vs.* ~32 nm). In the conventional theory, a higher porosity and a smaller crystallite size are preferred for alleviating the volume change during cycling for alloy-type anode.

Transmission X-Ray Microscopy (TXM)

To understand the role of Bi in improving cycling stability, 3D *ex situ* transmission X-ray microscopy (TXM) and 2D *in situ/operando* TXM were performed at the Stanford Synchrotron Radiation Light Source (SSRL) beamline 6-2. Alloy particles were imaged after 20 cycles at a current density of 100 mA/g, cycled between 0.05-1.5 V *vs.* Li/Li^+. Figures 4 a and b show the volume renderings of a primary particle from a [SnSb+Bi]-C and a [SnSb]-C composite after cycling, respectively. Figure 2.4 c and d show the corresponding cross-sectional slices. Both surface radial cracks and internal cracks (indicated with arrows) were observed for the [SnSb]-C composite particles after 20 cycles. 2D TXM images (Supplementary Figure 2.14 d-f) and SEM images (Supplementary Figure 2.13) of [SnSb]-C composite particles also showed major cracks, especially for the particles > 5 μm in diameter. This indicates that the Li ion diffusion and phase transformation induced stresses surpass the yield stress of the material. Moreover, images from the cycled [SnSb]-C electrodes showed large bumps protrude from particle surface due to volume expansion (Supplementary Figure 2.13), further increasing reaction sites for the formation of excessive SEI. For [SnSb+Bi]-C composite electrode, SEM images showed only minor bulges from the particle surface after 20 cycles according to Figure 2.12, and no severe cracking was

observed for particles < 2 μm diameter (Supplementary Figures S7 and S9a-c). For particles > 5 μm in diameter, minor cracks still form, as shown in the cross-sectional slice in Figures 4c and Supplementary Figure 2.12 e, f post-cycling SEM images. Nevertheless, most particle shapes were maintained, and no severe fracture was observed.

The morphology difference of these cycled powders can also help to explain the differences in cycling stability. The Coulombic efficiency of the [SnSb+Bi]-C anode reached ~99.5% after five cycles, suggesting that only minor electrolyte decomposition occurs on the anode particles at the initial cycles. For the [SnSb]-C anode, the Coulombic efficiency was 98.5% at the 20^{th} cycle. This indicates that newly exposed anode surfaces continuously lead to electrolyte decomposition reaction and subsequently decrease the Coulombic efficiency. The specific capacity for the [SnSb]-C anode was 631 mAh/g after 20 cycles. From 70^{th} to 150^{th} cycles, the specific capacity rapidly decayed from 622 mAh/g to 355 mAh/g, which indicates that the cracking observed in TXM eventually causes the particle to pulverize and the fractured fragments become electrical isolated. Previous *in-situ* TEM [71] and TXM studies[72] have shown that electrical isolation of fractured particles is one of the major capacity degradation mechanisms for alloy-type anodes.

Figure 2.5 shows the *in operando* 2D TXM of [SnSb+Bi]-C composite during the first lithiation and de-lithiation cycle. Li metal pouch cells were assembled with a [SnSb+Bi]-C composite electrode as the cathode. Low active material and high conductive carbon mass loading electrodes were used to prevent particle overlapping. Figure 2.5 b shows the pristine particle morphology. The areal expansion of individual particle (average over three particles) was calculated and is shown in Figure 2.5 a; the full set of *in operando* 2D TXM images are shown in Supplementary Figures S10-S11. For the SnSb initial lithiation reaction to form Li_3Sb and Sn at 0.8 V, the particle showed ~25% areal expansion. The expansion rate decreased after the first

plateau until full lithiation and finally reached ~40% areal expansion. This corresponds to ~65% volume expansion, assuming the particle expands uniformly in all directions. In contrast, the particle area stayed relatively constant during delithiation with no apparent volume shrinking. Overall, no major cracks were during this first cycle for all the imaged particles (Figure 2.5 c and d). This further verifies the effect of Bi addition on microstructure stabilization upon lithiation and de-lithiation.

Discussion

The Bi-enriched GB configuration (Figures 1e and 2) can be considered as the metallic counterpart to the well-known nanoscale intergranular films (IGFs) in ceramics initially identified by Clarke[73] or the "nanolayer" in the "Dillon-Harmer complexion" series[74]. Such intergranular films can generally be understood to be liquid-like interfacial phase that possess an equilibrium thickness,[73,75] which are thermodynamically 2D phases[74]. Notably, such nanoscale liquid-like interfacial phases can be also stabilized below the bulk solidus temperatures, in both ceramics (*e.g.*, Bi_2O_3-doped ZnO) and metallic alloys (*e.g.*, Ni-doped W), where they are known to promote activated sintering and Coble creep.[57,76,77]

In interfacial thermodynamics, a liquid-like interfacial film of thickness h can be thermodynamically stabilized at a GB at $T < T_S$, if the volumetric free-energy penalty to form the undercooled liquid (ΔG_{amorph}^{vol}) can be over-compensated by the reduction in the interfacial energies upon replacing a "dry" GB (γ_{gb}^0) with two crystal-liquid interfaces ($2\gamma_{cl}$):[54–57]

$$\Delta G_{amorph}^{vol.} \cdot h < \gamma_{gb}^0 - 2\gamma_{cl} \quad (1)$$

Following prior studies,[54–57] we can define a thermodynamic parameter

$$\lambda_0 \equiv \frac{\gamma_{gb}^0 - 2\gamma_{cl}}{\Delta G_{amorph}^{(vol)}} \tag{2}$$

where subscript "0" denotes that we adopt the bulk liquid composition at T_S as the liquid-like film composition in a simplification. This parameter λ_0 represents the thermodynamic ability to stabilize a liquid-like interfacial phase at an average general GB, and it scales the actual (equilibrium) interfacial width ($h_{eq.}$). For metallic systems, we can obtain an approximation $h_{eq.} = \xi \ln(\lambda/\xi)$, if the interfacial repulsion is dominated by a short-range exponentially decaying interaction ($\propto e^{-\xi}$).

Assuming that the Bi solubility is negligible, we can estimate $\gamma_{GB}^{(0)}$ as:

$$\gamma_{GB}^{(0)} \approx \sum_i X_i^C \gamma_{GB,\,i}^{(0)} + \frac{1}{6C_0 V_A^{\frac{2}{3}}} \sum_{i \neq j} X_i^C X_j^C \Omega_{i-j}^C \tag{3}$$

where C_0 is a constant ($\approx 4.5 \times 10^8$) in the Miedema "macroscopic atom" model, V_A is the average atomic volume, Ω_{i-j}^C is the molar crystal phase regular-solution parameter (for which we adopt the value of the SnSb phase from the NIST CALPHAD database for solder systems[9]). Here, the GB energy for a pure element i is estimated as: $\gamma_{GB,\,i}^{(0)} \approx \frac{1}{3}\gamma_{\text{Surface},\,i}^{(0)} = \frac{1}{3}\frac{\Delta H_i^{atomisation}}{C_0 V_A^{2/3}}$. Thus, we can obtain the following estimate for a SnSb GB (with $X_{Sn}^C = X_{Sb}^C = 1/2$):

$$\gamma_{GB}^{(0)} \approx \frac{1}{3C_0 V^{2/3}} \left[\frac{1}{2}\left(\Delta H_{\text{Sn}}^{\text{atomisation}} + \Delta H_{\text{Sb}}^{\text{atomisation}} \right) + \frac{1}{2}\left(\frac{1}{2}\right)^2 \Omega_{\text{Sn-Sb}}^C \right] \tag{4}$$

where the enthalpies of atomization ($\Delta H_i^{atomisation}$, i = Sn or Sb) can be found from the CRC handbook.

The crystal-liquid interfacial energy can be estimated by considering the enthalpic, chemical, and entropic contributions based on the Miedema "macroscopic atom" model

$$\gamma_{cl} \approx \frac{1}{C_0 V_A^{\frac{2}{3}}}\left[\sum_i X_i^C\left(\Delta H_i^{fuse} + \sum_{i\neq j} X_j^L \Omega_{i-j}^L\right) - \frac{1}{2}\left(\sum_{i\neq j} X_i^L X_j^L \Omega_{i-j}^L + \sum_{i\neq j} X_i^C X_j^C \Omega_{i-j}^C\right) + 1.9RT\right] \quad (5)$$

where the subscripts "C" and "L" represents crystal and liquid phases, respectively. The enthalpies of fusion are obtained from the CRC handbook.[10] The liquid phase regular-solution parameters (Ω_{i-j}^L) can be estimated based on the Miedema model.

The volumetric free energy to form the undercooled liquid can be calculated with the molar free energy of the bulk liquid phase and the reference free-energy state set by the chemical potentials of the bulk phases:

$$\Delta G_{\text{amorph}}^{(\text{vol})} = \frac{\left[G^L(\boldsymbol{X}_{film}^L) - \sum_i \mu_i X_i^L\right]}{(\sum_i V_i X_i^L)} \quad (6)$$

where $G^L(\boldsymbol{X}_{film}^L)$ is the molar free energy of the bulk liquid phase, μ_i is the chemical potentials (set by the bulk phase equilibrium), $\boldsymbol{X}_{film}^L = \{X_i^L\}$ represents the composition of the liquid-like interfacial film, and $\sum_i V_i X_i^L$ is the molar volume of the liquid phase. These functions and variables can be obtained from the CALPHAD simulation of SnSb+Bi based on the NIST database for solder systems.

Note that the specific value of λ depends on the selection of the composition of $\boldsymbol{X}_{film}^L = \{X_i^L\}$. We can adopt the maximum λ value via searching all possible film compositions:

$$\lambda \equiv \max_{\text{all } \boldsymbol{X}_{film}^L} \left\{\lambda\left(\boldsymbol{X}_{film}^L\right)\right\} \quad (7)$$

which is computationally expensive for a ternary system. Here, it is sufficient to adopt a reference film composition of $\boldsymbol{X}_0^L$ (43.8Bi-1.4Sb-54.8Sn at%, *i.e.*, the composition of the bulk liquid that will first appear upon heating), which is the composition of the liquid in the invariant reaction "(Bi, Sb)$_{\text{Rhombo}}$ + (Sn)$_{\text{BCT}}$ → SnSb + Liquid" at T_S = ~172 °C obtained from the CALPHAD simulation. We denote it as:

$$\lambda_0 \equiv \lambda(\boldsymbol{X}_0^L) \tag{8}$$

By the definition, we know: $\lambda_0 \leq \lambda$ and $\lim_{T \to T_0} (\lambda_0/\lambda) = 1$.

For Bi-statured SnSb specimens in the three-phase region (SnSb plus minor (Bi, Sb)$_{\text{Rhombo}}$ and (Sn)$_{\text{BCT}}$ phases) below the lowest bulk solidus temperature (T_S = ~172 °C), $\lambda_0 = \lambda_0(T)$ is a function of temperature. Figure 2.18 shows computed λ_0 *vs.* temperature curve for a SnSb + 2.8 at.% Bi alloy (*i.e.*, in the three-phase region) for predicting the stabilization of Bi-enriched liquid-like interfacial phase below the bulk solidus (ternary invariant) temperature T_S. Here, the thermodynamic variable λ_0 represents an (upper bound) estimate of the thickness of a premelting-like interfacial film that can be thermodynamically stabilized at an average general GB. The computed λ_0 scales with the actual interfacial width, and it is divergent ($\lambda_0 \to \infty$) at T_S = ~172 °C when a bulk liquid phase appears. A corresponding computed GB diagram is shown in Figure 2.2 h in the main article.

We calculated λ_0 *vs.* temperature curve for a SnSb + 2.8 at% Bi alloy (noting that $\lambda_0(T)$ is a constant at a fixed temperature in the three-phase region), which is shown in Supplementary Figure 2.19. Furthermore, a computed GB diagram is shown in Figure 2.2 h, where red dashed lines (computed λ_0 values) are plotted in the bulk isopleth of SnSb + *x* at% Bi to represent the (upper bound of) estimated thickness of a liquid-like interfacial film that can be

thermodynamically stabilized at an average general GB. The calculated λ_0 value of ~1.1 nm at room temperature suggests a liquid-like character of the Bi-enriched GB structure, which also has a Bi-enriched and Sb-depleted composition akin to the bulk liquid phase (Figure 2.2 g). Such a Bi-enriched, nanoscale, liquid-like interfacial phase can promote GB sliding and Coble creep to mitigate cracking during electrochemical cycling.

In a broader context, this nanoscale liquid-like interfacial phase represents one of segregation-based 2D interfacial phases that can form spontaneously as a thermodynamically equilibrium state (also named as "complexions"[74]) with composition and properties distinct from the corresponding bulk phase. Moreover, there are compositional and structural gradients in the through-thickness direction (Figure 2.2 g), factors that are character of GB complexions[74] that differentiates these 2D interfacial phases from thin precipitation layers of a 3D bulk phase.

In the current case, this Bi-enriched interfacial phase can help to improve cycling stability via two possible mechanisms. First, Bi segregation at GBs may stabilize the grain structure within the secondary particles during cycling. Second, its liquid-like character (analogous to segregation-induced interfacial premelting[78,79]) can promote GB sliding and Coble creep to release stress during cycling. Indeed, Sn-Bi alloys are known to exhibit superplasticity at room temperature due to GB sliding and enhanced Coble creep[51,52]. We hypothesize that a similar mechanism can prevail in SnSb-Bi alloys, which is supported by the interfacial thermodynamic modeling and cryo-STEM-EDS analysis (Figure 2.2).

During alloy type anode lithiation, mechanical stresses can induce cracks formation.[80] Lithiation of alloy-type anodes usually involves multiple phase transformations, each of which has an associated volume expansion. For SnSb, lithiation results in the formation of Li_3Sb and various Li-Sn intermetallic compounds.[24] Abrupt Li concentration change generally exists at the phase

boundary. With the volume expansion from the particle shell, the particle core region can experience compressive hoop stress, and the lithiated surface forms tensile hoop stress. Surface fractures occur when the accumulated stress exceeds the yield strength of the material.[81,82] Various factors can affect stress evolution, including Li-ion diffusion coefficients, current densities, and the electrode particle geometry, as indicated by both experimental studies and computational models.[7,80,81]

On the other hand, it is known that low GB sliding resistance and high GB diffusion coefficients can enable Coble creep.[51,83,84] For the Sn-Bi alloys, for example, Bi GB sliding is facile even at room temperature due to the high GB diffusion coefficient (estimated to be 6.23×10^{-21} m^3s^{-1} for Bi GBs, and 3.15×10^{-21} m^3s^{-1} for Sn GBs).[51] Similar effects can exist in the SnSb-Bi GBs due to the formation of liquid-like interfacial phase (Figure 2.2). For lithiation of high volumetric expansion anode, GBs are also subjected to stress; GB sliding and Coble creep have been reported as one of the mechanisms for stress relaxation.[81,85] In the current work, the dense SnSb+Bi anode can achieve better cycling stability with less porosity and a larger mean grain size in comparison with the more porous SnSb anode with smaller grains. The cycled SnSb+Bi anode also showed less severe surface bulges and cracks after cycling based on post-cycling SEM and TXM characterization. This observation suggests the Bi segregation at GBs can stabilize microstructure upon cycling. Here, we further hypothesize that the Bi-enriched, nanoscale interfacial phase at the SnSb GBs can also assist GB sliding and Coble creep, akin to Sn-Bi.[51] The strain energy could be released via GB sliding and Coble creep to alleviate GB stress concentration. A similar hypothesis of stress relief mechanism via GB sliding was also previously proposed for 3Ag-0.5Cu-96.5Sn alloy type anodes[85] and cobalt boride modified $LiNi_{0.8}Co_{0.1}Mn_{0.1}O_2$ cathodes[86] (but without direct evidence). For SnSb-Bi, this hypothesized mechanism is supported by

interfacial thermodynamic modeling and a careful cryo-STEM-EDS analysis, along with the *in operando* TXM characterization.

While bulk Bi is known to lithiate at 0.8 V, there is also a possibility that the Bi-enriched interfacial phase can be lithiated. Yet, the formation of any crystalline Bi-Li intermetallic compound would likely increase the interfacial energy so that it may be suppressed (in comparison with the lower energy liquid-like interfacial phase). Further detailed GB characterization after cycling is needed to clarify this issue.

In a broader context, this study supports an emerging approach of thermodynamics driven interfacial engineering via spontaneous formation of 2D interfacial phases (complexions).[87–90] These 2D interfacial phases are different from thin layers of 3D bulk phases in that they have a thermodynamically determined self-limiting thickness (~ 1 nm in this case), and they can form spontaneously. Both liquid-like[91–93] and ordered[87,94,95] GB complexions have been reported in various ceramic and metallic materials, including solid electrolytes and battery systems.[28,89] Analogous nanoscale surface phases with self-selecting thickness have also been used previously to improve battery performance,[28,96,97] and this study further suggests a new route to engineer GBs in alloy-type anodes (potentially extendable to other volume expansion materials).

Conclusion

We investigate a thermodynamically controlled method to tailor the stability of alloy-type anode. The spontaneous formation of a 2D liquid-like interfacial phase induced by Bi segregation was used to modify the GBs in an SnSb anode as an exemplar. This was achieved via a facile ball milling and annealing method. Both cryogenic STEM HAADF imaging and EDX elemental mapping revealed Bi enrichment at SnSb GBs. Our modeling showed that a nanoscale, Bi-enriched, liquid-like, interfacial phase can be thermodynamically stabilized at general GBs. The

Bi containing electrode showed improved cycling stability and rate capability compared to a pure SnSb electrode, despite the fact that the Bi containing material is both denser (~ 99% dense particles) and shows larger primary grain sizes within comparable secondary particles. A specific capacity of 565.5 mAh/g was maintained for SnSb+Bi carbon composite electrode after 200 cycles, which corresponds to an 85.9% capacity retention. Post-cycling SEM, 3D TXM, and *in operando* 2D TXM all demonstrate that the Bi GB modification significantly suppressed intergranular cracking upon lithiation and delithiation. In addition to stabilizing GBs, the nanometer-thick, Bi-enriched, interfacial phase may facilitate GB sliding and Coble creep to alleviate stress and avoid fracture upon cycling. This work thus suggests thermodynamically driven interfacial engineering of GBs as a new approach to improve the performance of battery electrode materials, particularly volume expansion anodes.

Experimental Procedures

Sample Preparation

The alloy anodes were prepared using planetary ball milling. To fabricate alloyed particles of SnSb (without carbon), Sn (Alfa Aesar, 99.80%, 325 mesh) and Sb (Alfa Aesar, 99.5%, 200 mesh) in 1:1 mol ratio (total 4.809 g) were placed into a 100 ml yttrium stabilized zirconium oxide (YSZ) grinding jar with seven 10-mm and 50 3-mm YSZ grinding balls inside an Ar filled glovebox. The milling process was conducted for 8 hours (48 cycles of 10 min each, with resting of 5 min in between) with a Across International PQ-N04 planetary ball mill at room temperature. To fabricate SnSb+Bi, 5 wt% Bi (Alfa Aesar, 99.999%, 200 mesh) was added, and the rest the recipe is identical. To make [SnSb]-C and [SnSb+Bi]-C carbon composites (in a second step), 6.2 wt% graphite was added into the alloyed particles made via the above steps and subsequently milled for another 16 hours (96 cycles of 10 min each, with resting of 5 min in between). To

achieve a thermodynamic equilibrium, the milled powder was placed in a covered alumina crucible and isothermally annealed at 250 °C (ramped with 5 °C/min heating rate) for 3 hours in a tube furnace in an Ar atmosphere. For the dense SnSb pellet with 2.8 at% of Bi, the ball milled powders (Sn and Bi in 1:1 mol ration with 5 wt% Bi) were uniaxially pressed in a stainless-steel die and placed in a covered alumina crucible and isothermally annealed at 250 °C (ramped with 5 °C/min heating rate) for 12 hours in a tube furnace in an Ar atmosphere. The sintered pellet was polished before characterization.

Materials Characterization

The alloy anodes were characterized by X-ray diffraction (XRD) with a Bruker D2 Phaser (Cu Kα radiation, λ = 1.5406 Å). To fabricate transmission electron microscopy (TEM) sample, a dual-beam focused ion beam FIB/SEM system (FEI Scios) was used to lift-out lamella. The powder grain structure was characterized with cryogenic TEM using a JEOL JEM-2800 microscope operated at 200 kV. SnSb+Bi alloy particles can be melted under room temperature with electron beam exposure. Thus, a liquid N_2 cooling holder (Gatan 626) was used to cool the TEM samples to around -170 °C to minimize beam damage. Transmission X-ray Microscopy (TXM) was conducted at the Stanford Synchrotron Radiation Lightsource (SSRL) on beamline 6-2C. 8.95 KeV X-rays were utilized to characterize the particle morphology. The alloy particles were placed in a quartz tube and sealed with epoxy in an Ar filled glovebox. The tomography data were taken over an angular range of 180°. X-ray images were processed using TXM-Wizard.[98]

Electrochemical Characterization

70 wt.% ball milled alloy powders were mixed with 15 wt% carbon fibers (Sigma-Aldrich) and 15 wt% carboxymethyl cellulose (CMC, MTI Corp) in DI water. Such a relatively high conductive carbon content was typically used for high-volume-change alloy type anode materials

to accommodate the volume expansion. Future optimization of active material-binder-conductive carbon ratio is required to increase electrode active material content. For *in situ* TXM experiment, an electrode with low active material loading (25 wt% active, 56 wt% carbon fiber, and 19 wt% CMC) were used to prevent particles overlapping. The slurry was mixed using a Thinky mixer (ARE-310) for 2 hours at 2000 rpm. The slurry was coated on a copper foil (9 μm thick, MTI Corp) with a doctor blade, dried first in air for 12 hours, and subsequently dried further at 80 °C for 12 hours in vacuum. The active material mass loading of the electrode was ~ 1.5 mg/cm^2. The electrode was not calendared after casting. Cycling tests were carried out with Li metal anode (excess amount, ~0.6 mm thick, ~16 mm diameter) and Celgard 2320 separator using 2032 coin cell. Two 0.5 mm thick spacer and one spring was used during coin cell assembly, and the total mass for the assembled coin cell is around 13 g. For *in situ* TXM characterization, Li metal pouch cells were assembled in an argon filled glovebox. 1 M $LiPF_6$ in a 1:1 ethylene carbonate/diethyl carbonate solvent (LP40, Sigma-Aldrich) with 5 vol% fluorinated ethylene carbonates (FEC, Sigma-Aldrich) was used as the electrolyte (excess amount was used). Constant current cycling was conducted in a potential range of 0.05 – 1.5 V vs. Li/Li$^+$ under ~20 °C room temperature. The specific capacities were calculated based on the 70 wt.% active material to be around 660 mAh/g at 100 mA/g current density. Assuming ~250% volume expansion, the volumetric capacity of SnSb+Bi carbon composite anode can be calculated to be around 1790 Ah/L. The gravimetric stack energy was estimated using the model reported by Obrovac *et al*..[3] By using the $LiCoO_2$ (LCO) as baseline cathode with 530 Ah/L volumetric capacity, 1.1 N/P ratio, SnSb+Bi carbon composite anode average voltage of 0.75V, the stack energy can be calculated to be around 850 Wh/L. This corresponds to at least 17% increase compared to LCO/graphite cell (calculated to be 726 Wh/L using the same model)

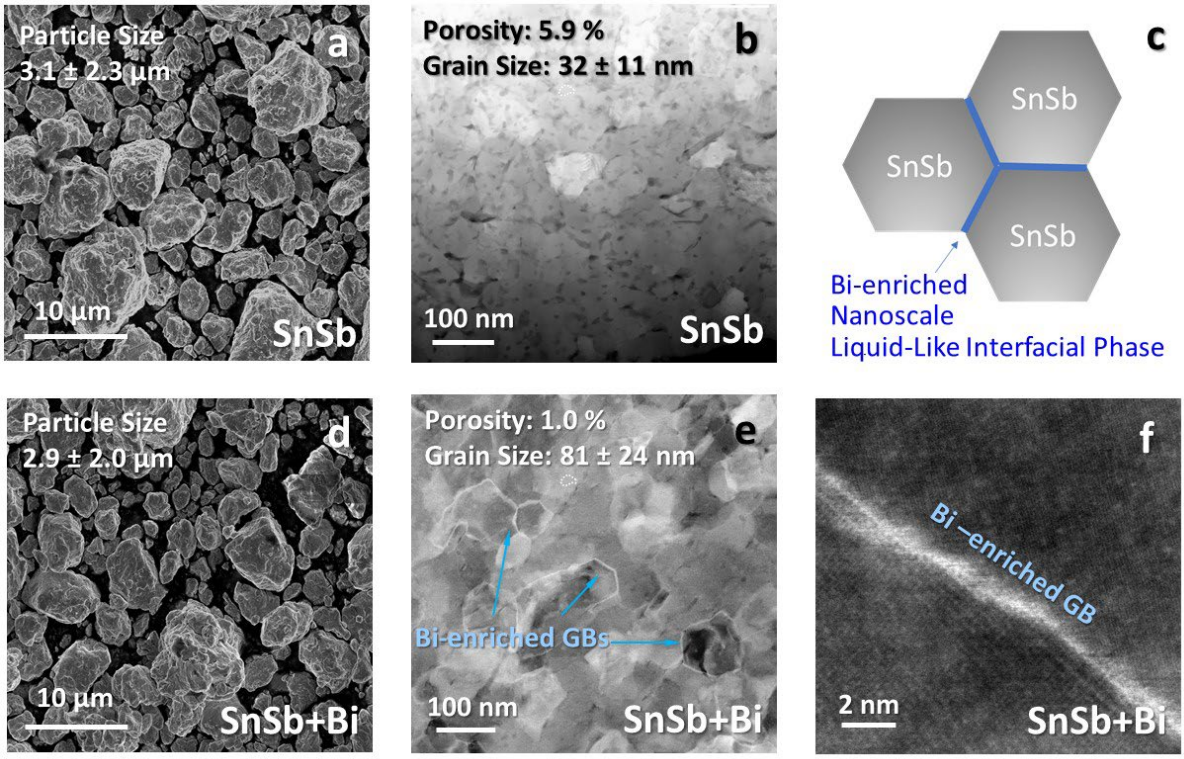

Figure 2.1 Scanning electron microscopy (SEM) and cryogenic scanning transmission electron microscopy (cryo-STEM) micrographs of the SnSb and SnSb+Bi anode materials. SEM images of (a) SnSb and (d) SnSb+Bi particles shows similar secondary particle diameters. High-angle annular dark-field (HAADF) cryo-STEM images of (b) SnSb and (e) SnSb+Bi, where the bright contrast at grain boundaries (GBs) in the latter indicates the formation of a Bi-rich interfacial phase. (f) High-magnification HAADF cryo-STEM image showing bright contrast at GBs indicating Bi segregation in the SnSb+Bi specimen. STEM specimens were imaged at cryogenic temperatures, which is essential to prevent beam damage (melting) of the specimens. (c) A schematic diagram of the SnSb+Bi grain structure.

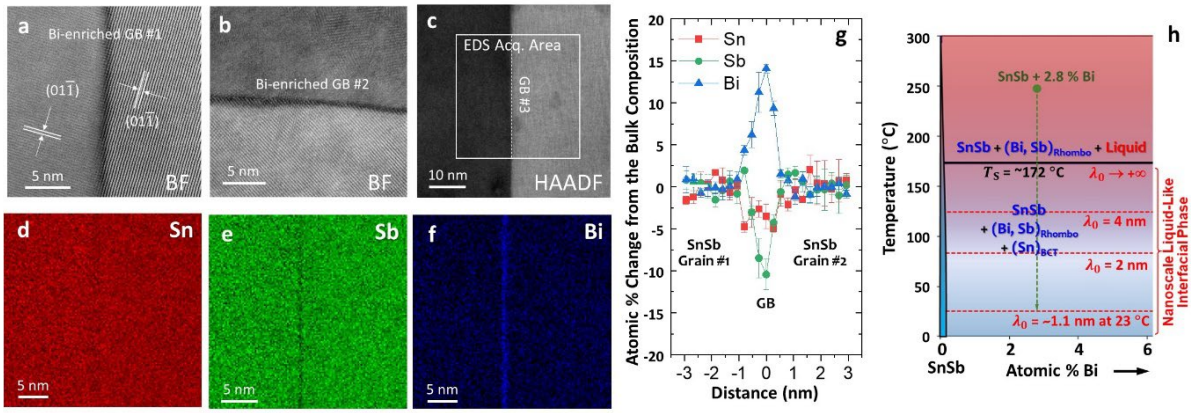

Figure 2.2 Cryo-STEM images and energy dispersive X-ray spectroscopy (EDS) elemental maps of a SnSb+Bi grain boundary (GB) and thermodynamic modeling. (a) and (b) High-magnification cryo-STEM BF images of SnSb+Bi GBs. (c) Cryo-STEM HAADF image of a SnSb+Bi GB and the EDS acquisition area. EDS elemental maps for (d) tin, (e) antimony, and (f) bismuth (in atomic percentages). (g) Line profile across the GB showing the changes in the atomic percentages of Sn, Sb, and Bi with respect to the bulk composition. This GB structure can be considered as a nanoscale, Bi-enriched, liquid-like, interfacial phase. (h) A computed GB λ diagram,[54–57] where red dashed lines (computed λ_0 values) are plotted in the bulk isopleth of SnSb + x at% Bi to represent the (upper bound of) estimated thickness of a liquid-like interfacial phase that can be thermodynamically stabilized at an average general GB. Note that $\lambda_0 \rightarrow \infty$ at T_S= ~172 °C, where a bulk liquid phase appears. See Supplementary Note and Figure 2.19 for the underlying interfacial thermodynamic model and calculation procedure.

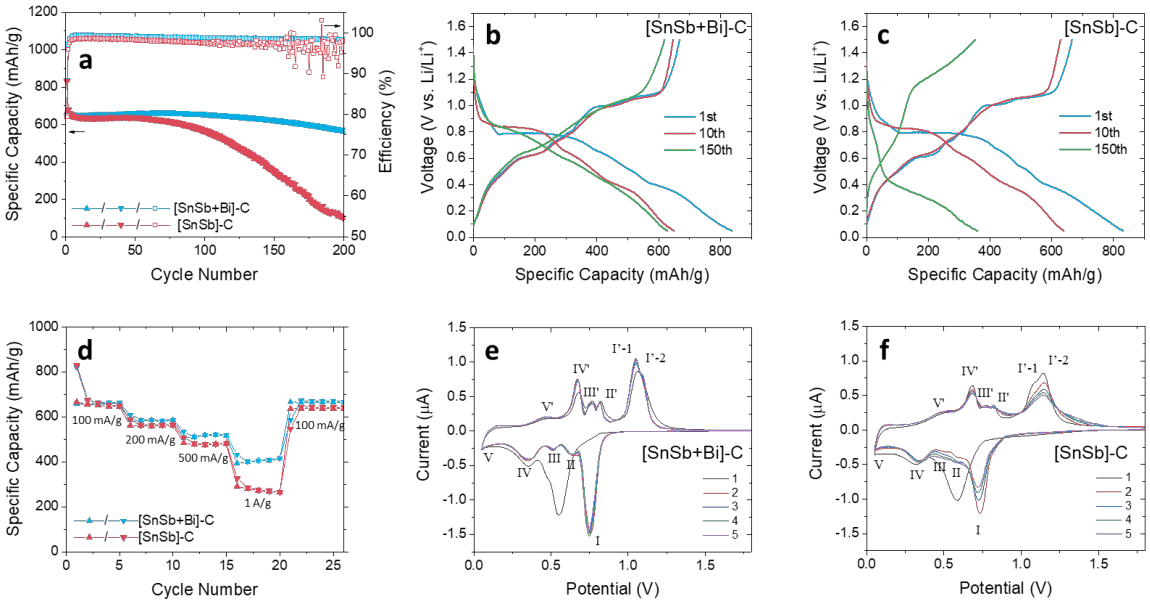

Figure 2.3 Electrochemical characterization of the [SnSb]-C and [SnSb+Bi]-C composite anodes. (a) Cycling stability comparison for the [SnSb]-C and [SnSb+Bi]-C composite anodes cycled at 100 mA/g between 0.05-1.5 V vs. Li/Li^+. Here, "▲" represents charge specific capacity, "▼" represents discharge specific capacity, and "□" represents the Coulombic efficiency. (b) [SnSb+Bi]-C and (c) [SnSb]-C composite anode for the 1st, 10th, and 150th cycle at 100 mA/g. (d) Rate capability comparison of [SnSb]-C and [SnSb+Bi]-C composites samples. Cyclic voltammograms of (e) [SnSb+Bi]-C and (f) [SnSb]-C composite anodes for 5 cycles at 0.1 mV/s between 0.05 and 1.5 V vs. Li/Li^+.

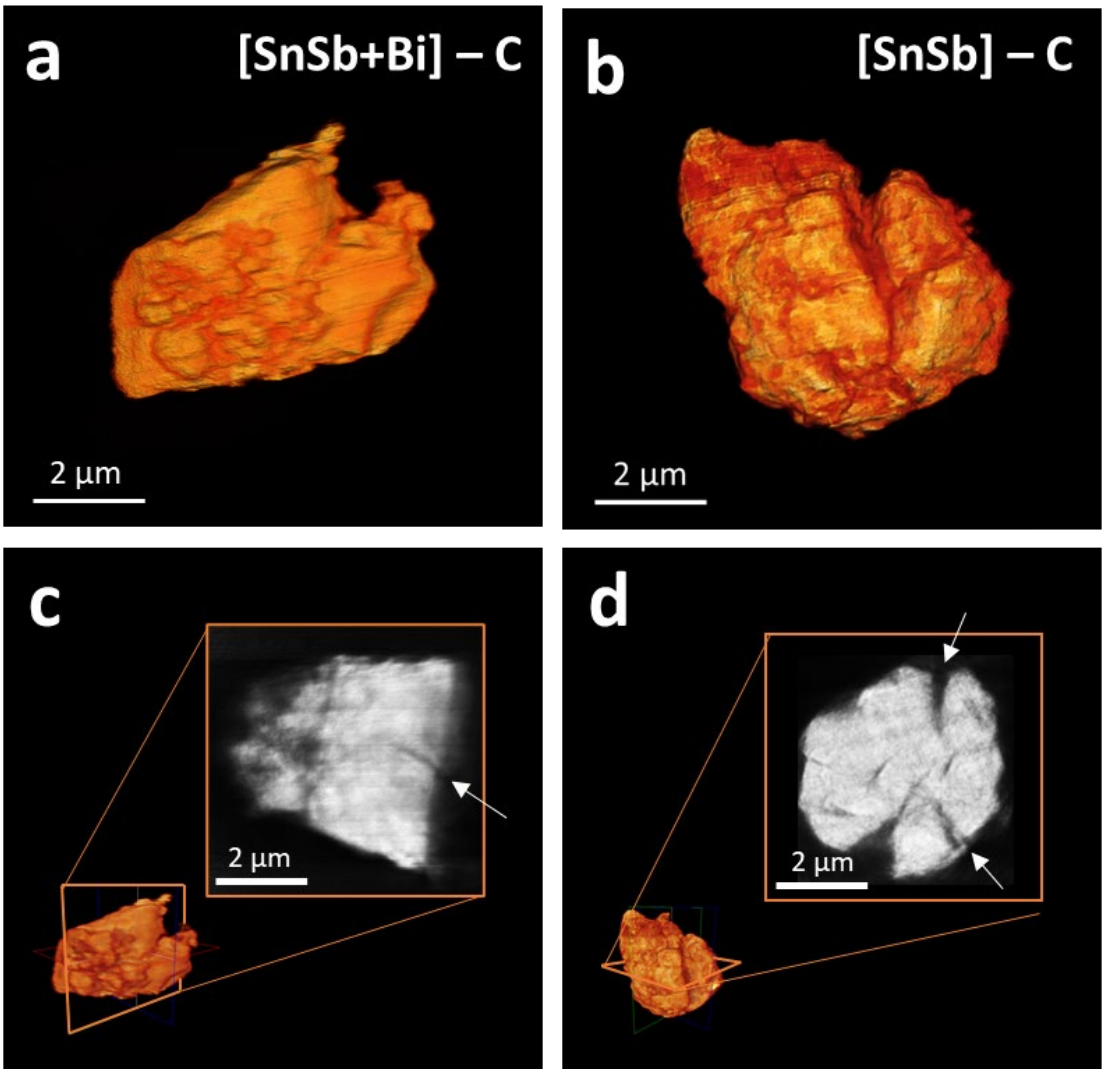

Figure 2.4 Comparison of the changes in morphologies upon cycling for [SnSb]-C and [SnSb+Bi]-C composite anodes. 3D X-ray tomographic reconstructions of a single secondary particle from (a) [SnSb+Bi]-C and (b) [SnSb]-C composite anodes after 20 cycles down to 0.05 V vs. Li/Li^+. Cross-section slices of a secondary particle from (c) [SnSb+Bi]-C and (d) [SnSb]-C composite anodes after 20 cycles down to 0.05 V vs. Li/Li^+. Cracks are indicated with white arrows.

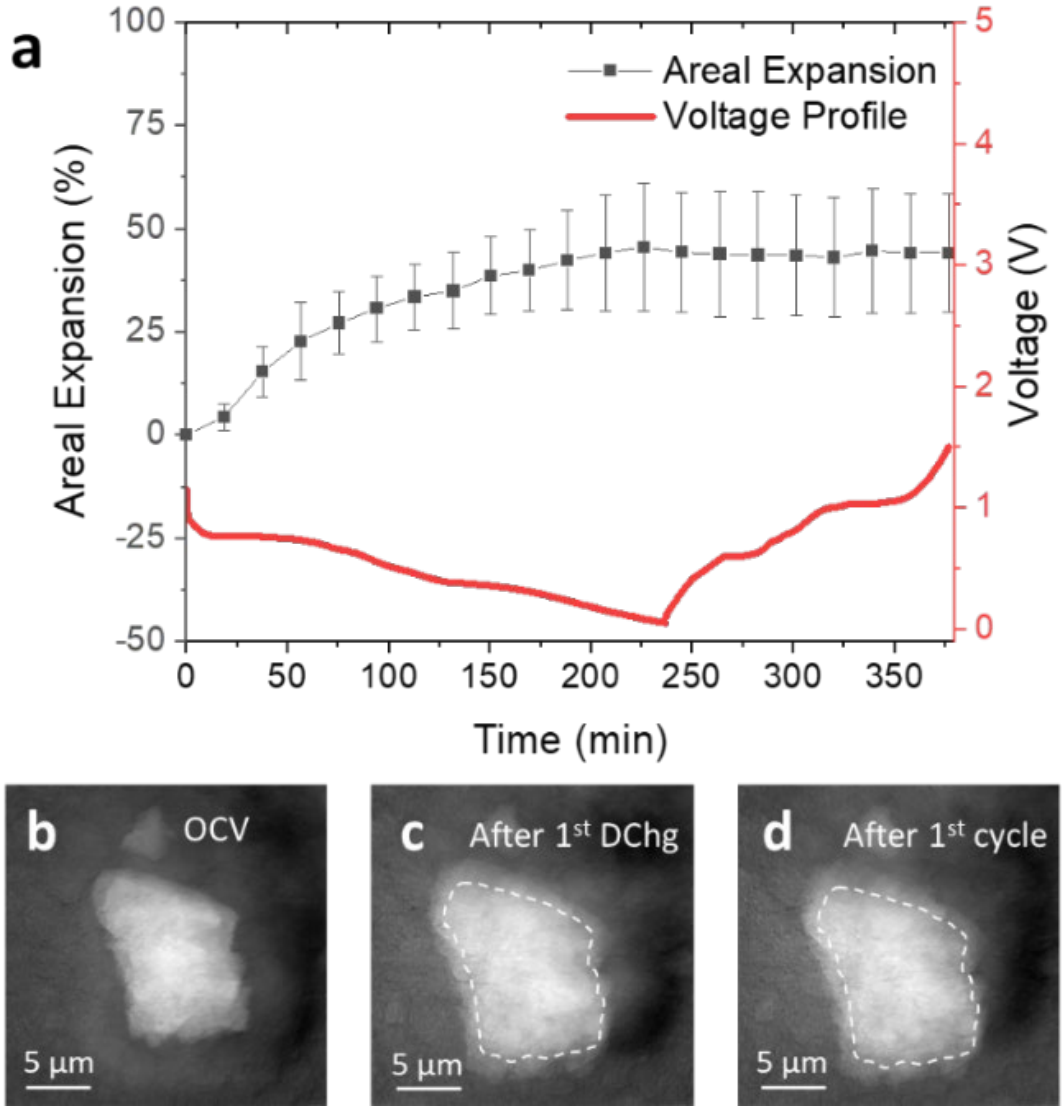

Figure 2.5 In situ/operando 2D TXM characterization of a [SnSb+Bi]-C composite anode. (a) The change in areal expansion during the first cycle. TXM images of at the (a) OCV, (b) full lithiation, and (d) delithiation states.

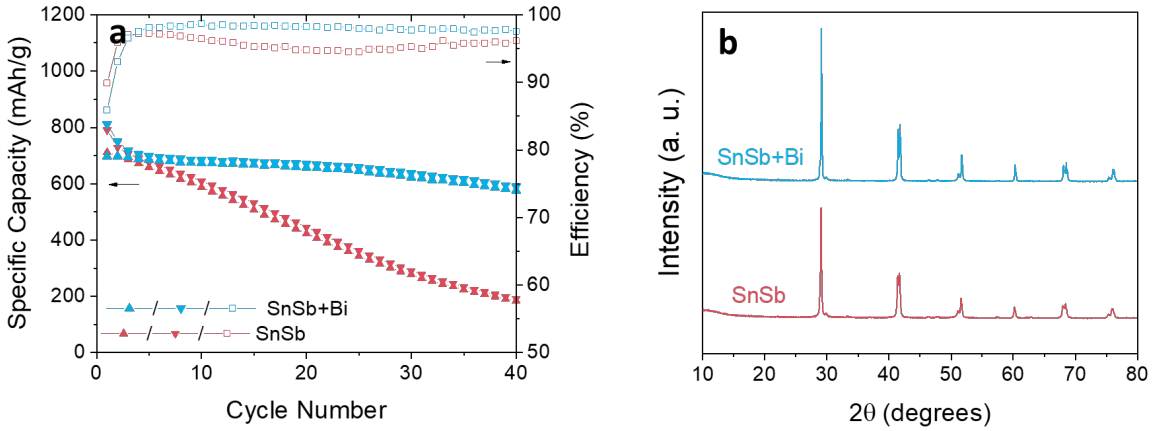

Figure 2.6 (**a**) Cycling performance and (**b**) XRD comparison of SnSb+Bi and SnSb. The cells were cycled at 100 mA/g with the voltage range of 0.05 V – 1.5 V. Here, "▲" represents electrode charge specific capacity, "▼" represents discharge specific capacity, and "□" represents the Coulombic efficiency.

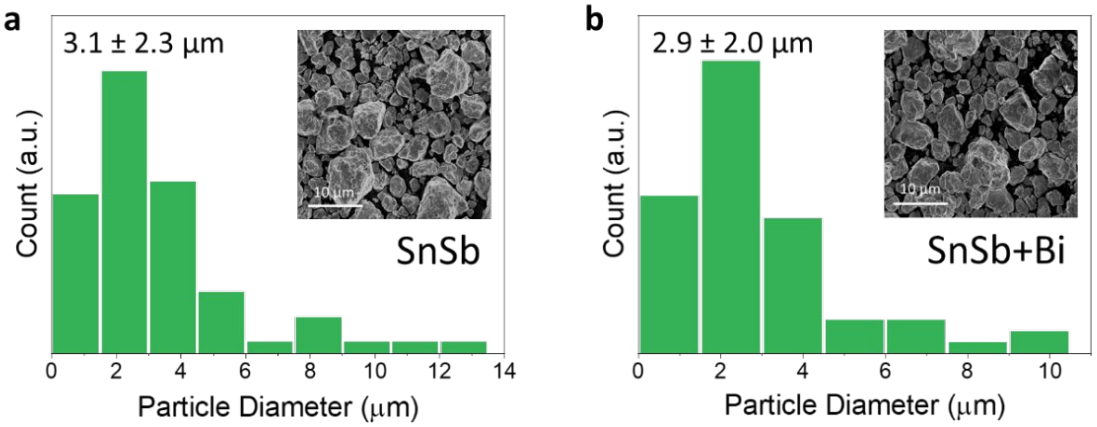

Figure 2.7 SEM and particle diameter distribution of planetary ball milled (**a**) SnSb and (**b**) SnSb+Bi.

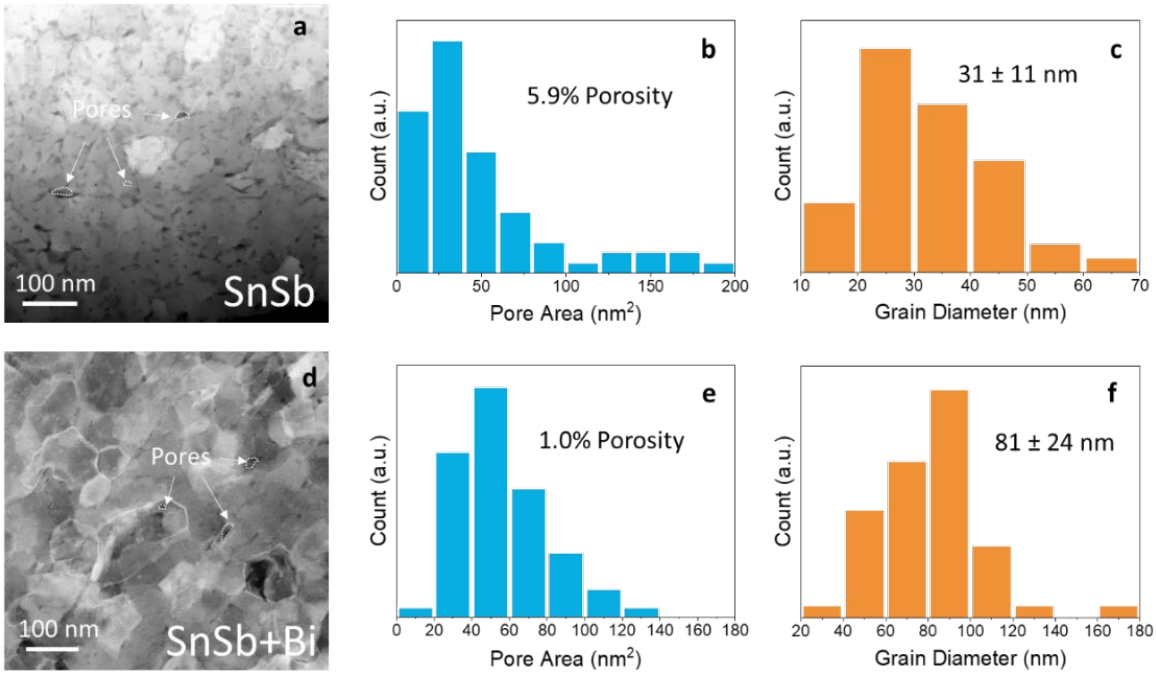

Figure 2.8 Cryo-STEM HAADF micrographs of (**a**) SnSb and (**d**) SnSb+Bi. Cross-sectional pore area distributions and total calculated porosities of (**b**) SnSb and (**e**) SnSb+Bi. Grain diameter distributions of (**c**) SnSb and (**f**) SnSb+Bi.

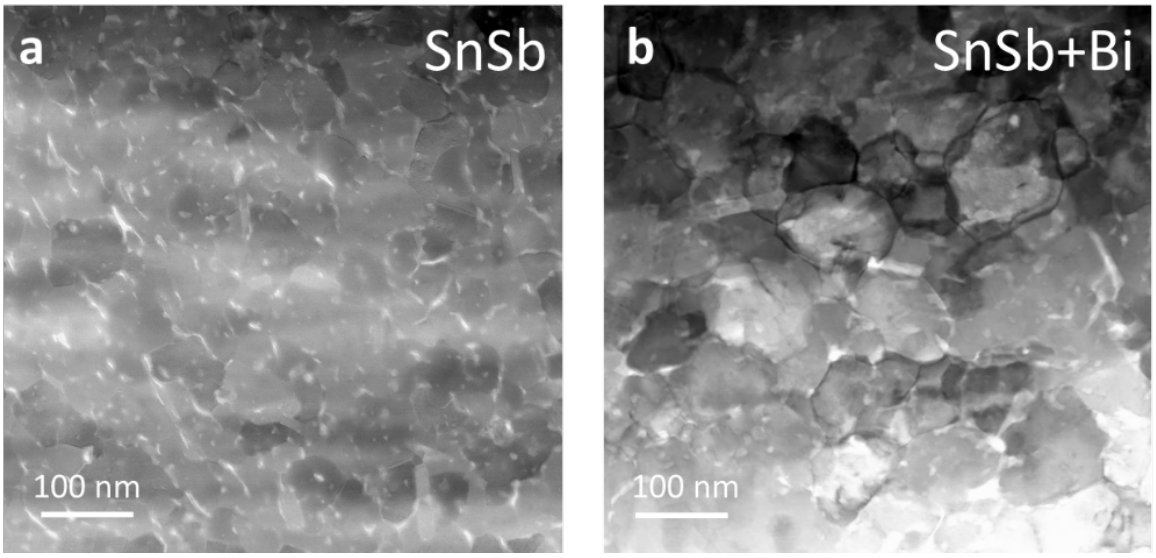

Figure 2.9 Cryogenic scanning transmission electron microscopy (cryo-STEM) bright field images of (**a**) SnSb and (**b**) SnSb+Bi. Bi-enriched grain boundaries (GBs) with dark contrast in the bright field image were observed for SnSb+Bi.

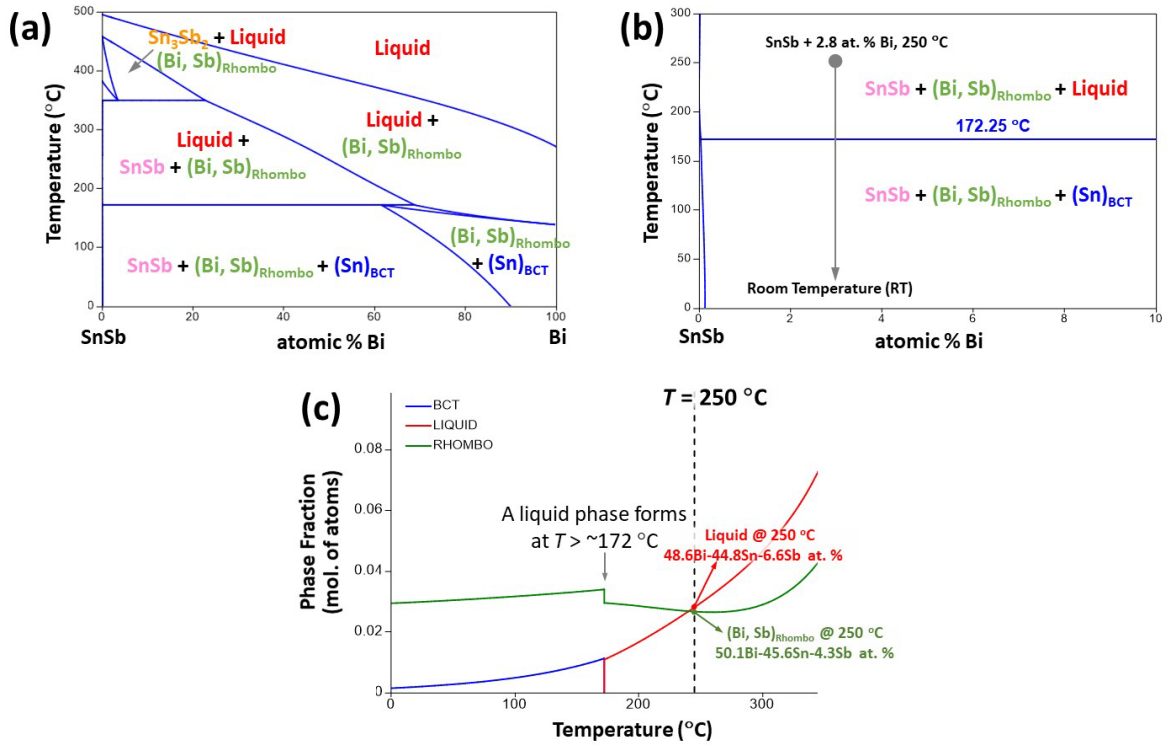

Figure 2.10 CALPHAD calculations of Bi-Sn-Sb ternary system based on the NIST solder systems database (https://www.metallurgy.nist.gov/phase/solder/solder.html). (**a**) Computed isopleth of SnSb-Bi and (**b**) an enlarged portion, where our composition and annealed and battery operation conditions are highlighted. A ternary invariant reaction, SnSb + Liquid → $(Bi, Sb)_{Rhombo}$ + $(Sn)_{BCT}$, takes place at T_S = ~172°C, above which a (bulk) liquid phase forms. (**c**) Computed phase fractions *vs.* temperature curves for the composition SnSb + 2.8 at% Bi (*i.e.*, 48.6 Sn – 48.6 Sb – 2.8 Bi atomic %).

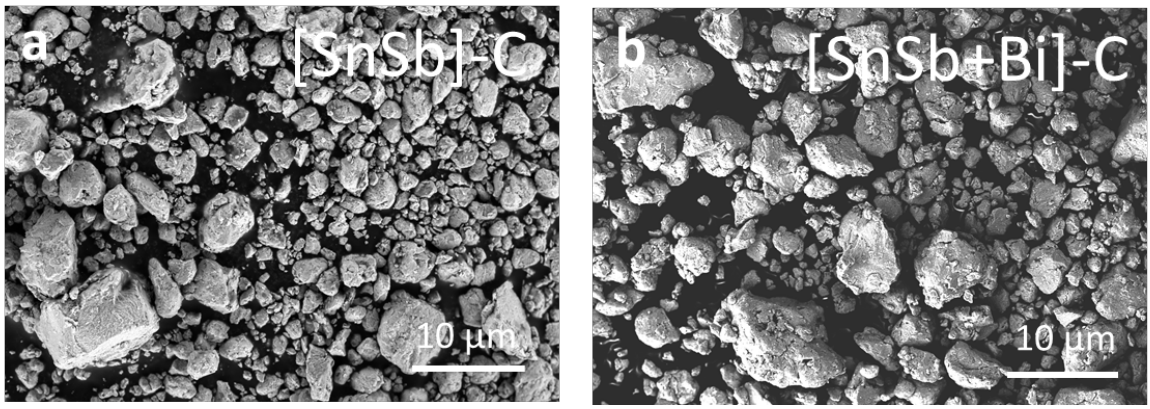

Figure 2.11 SEM images of planetary ball milled (**a**) [SnSb]-C and (**b**) [SnSb+Bi]-C composite anodes.

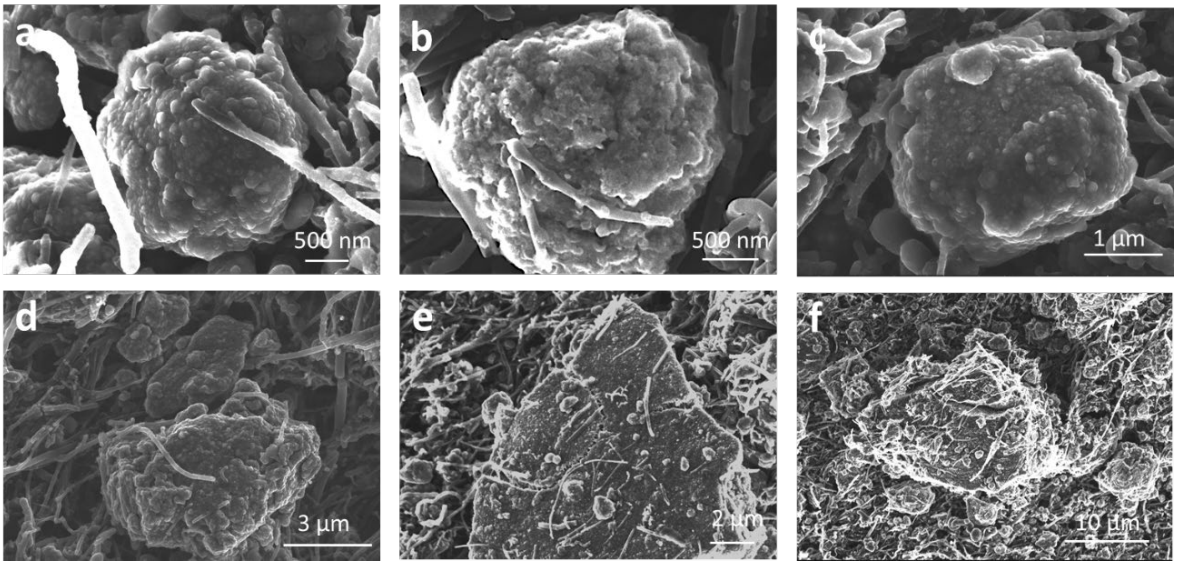

Figure 2.12 SEM images of a [SnSb+Bi]-C composite anode after 20 cycles showing representative particles of various sizes.

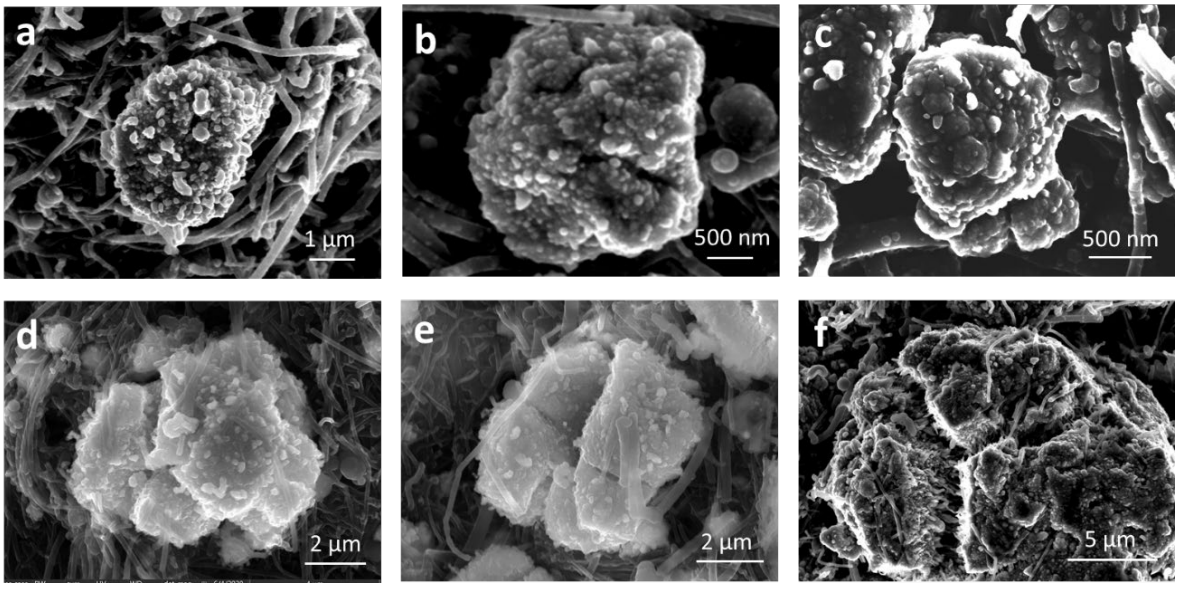

Figure 2.13 SEM images of a [SnSb]-C composite anode after 20 cycles showing representative particles of various sizes.

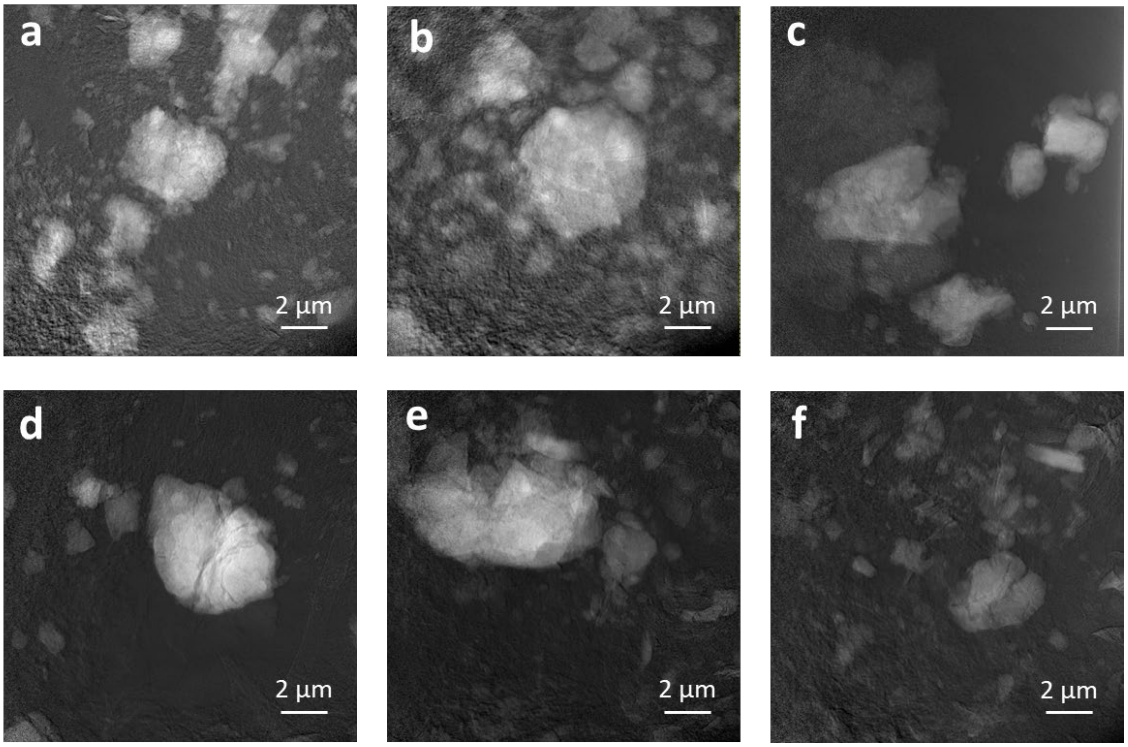

Figure 2.14 Transmission X-ray microscopy (TXM) images of (**a-c**) [SnSb+Bi]-C and (**d-f**) [SnSb]-C composite anodes after 20 cycles.

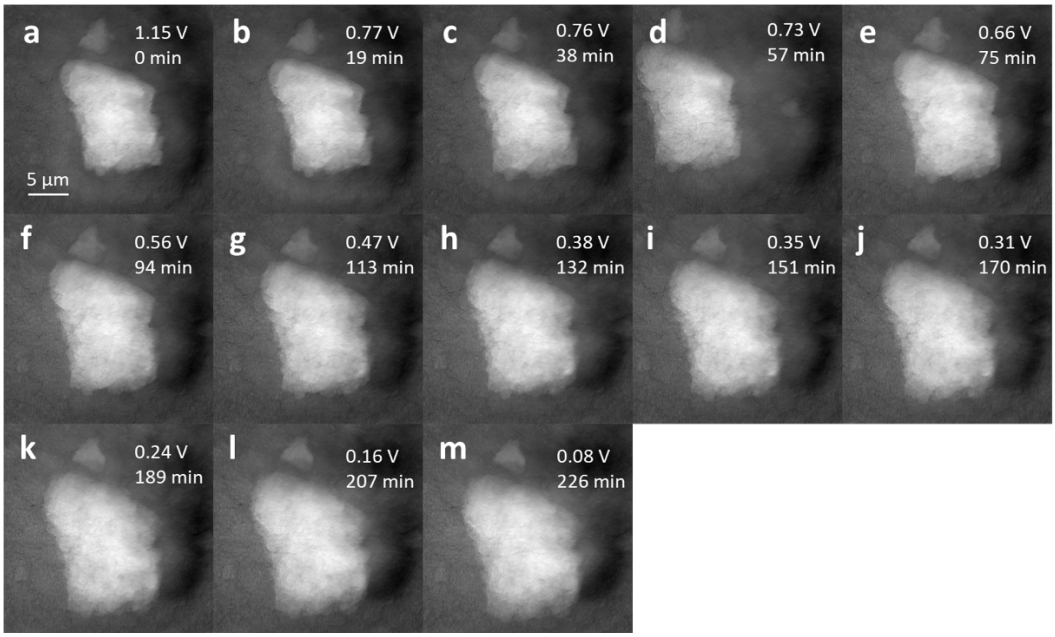

Figure 2.15 *In-situ* 2D TXM images of a [SnSb+Bi]-C composite anode during lithiation in the first cycle.

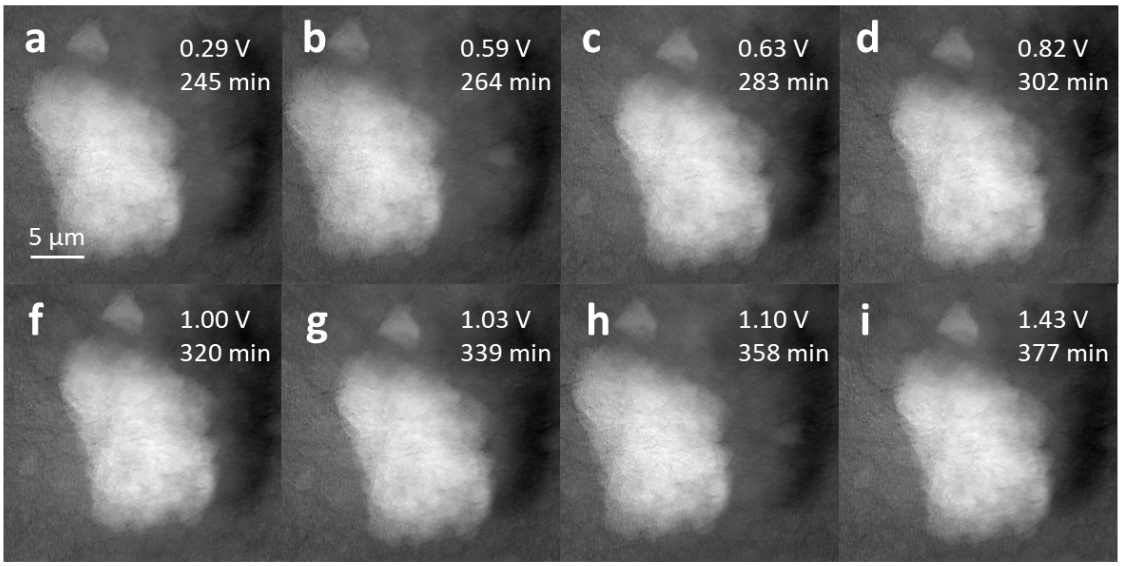

Figure 2.16 *In-situ* 2D TXM images of [SnSb+Bi]-C composite anode during delithiation in the first cycle.

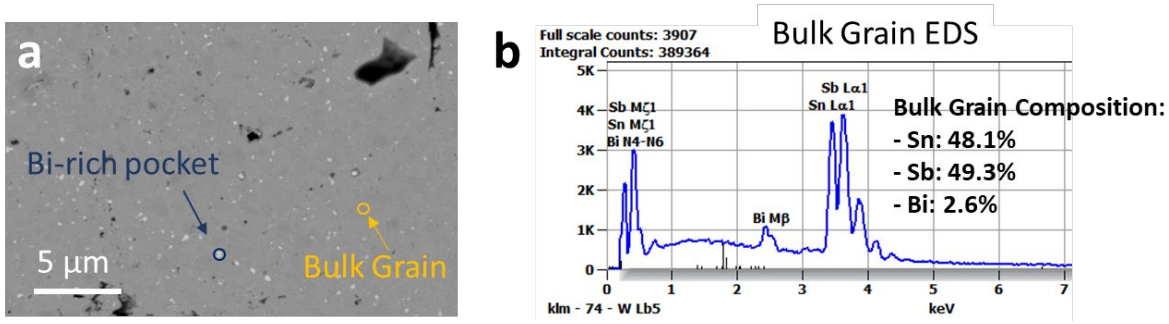

Figure 2.17 (**a**) SEM of a dense SnSb + 2.8 at% Bi pellet. (**b**) EDS spectra and elemental quantification of a region inside a SnSb grain.

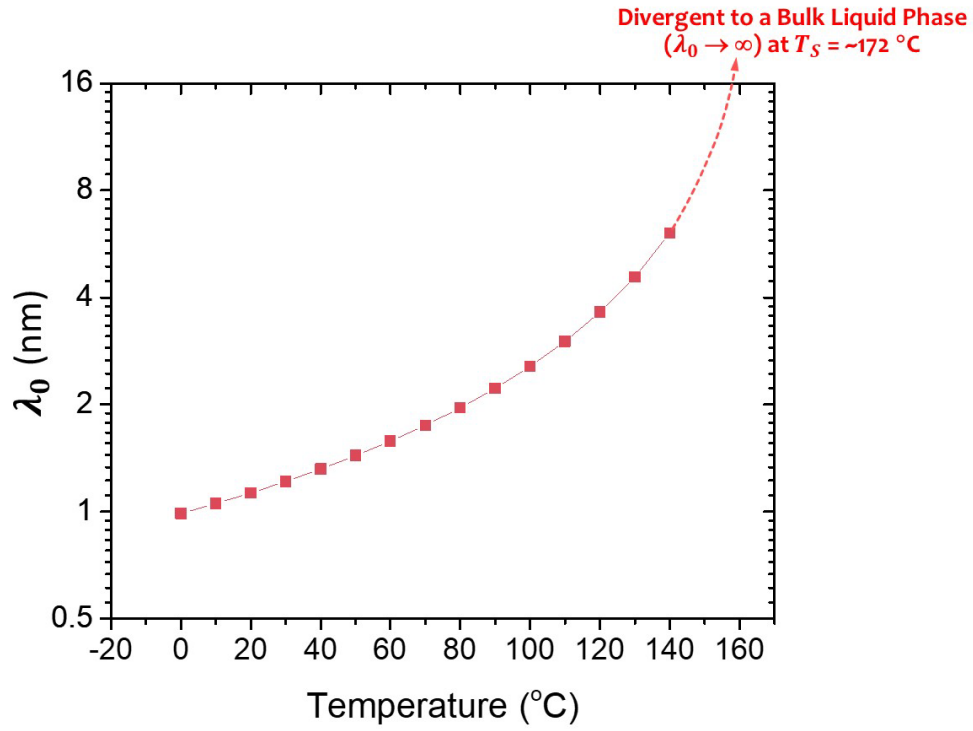

Figure 2.18 Computed λ_0 *vs.* temperature curve for a SnSb + 2.8 at% Bi alloy (*i.e.*, in the three-phase region of the ternary alloy, where $\lambda_0 = \lambda_0(T)$ is only a function of temperature) for predicting the stabilization of the Bi-enriched liquid-like interfacial phase below the bulk solidus temperature T_S. Here, the thermodynamic variable λ_0 represents an estimate of (of the upper limit of) the thickness of a premelting-like interfacial film that can be thermodynamically stabilized at an average general grain boundary (GB). The computed λ_0 scales with the actual interfacial width, and it is divergent ($\lambda_0 \rightarrow \infty$) at T_S = ~172 °C when a bulk liquid phase appears. A corresponding computed GB diagram is shown in Figure 2h in the main article. See Supplementary Note for details on the definition and calculation of λ_0 and the relevant interfacial thermodynamic model and parameters used.

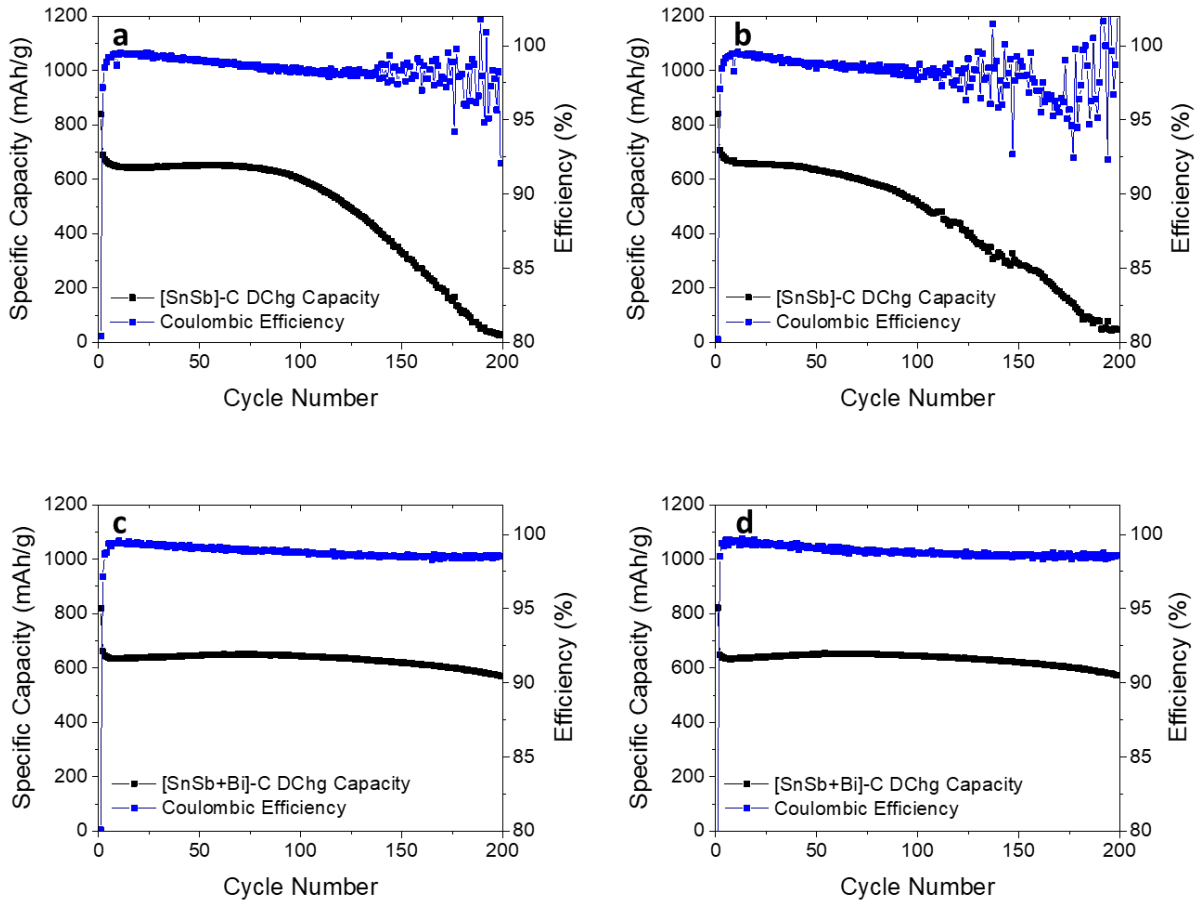

Figure 2.19 Cycling stability test from two individual cells of the (**a**, **b**) SnSb and (**c**, **d**) SnSb+Bi carbon composite anodes. The cells were all cycled at 100 mA/g between 0.05-1.5 V *vs.* Li/Li^+.

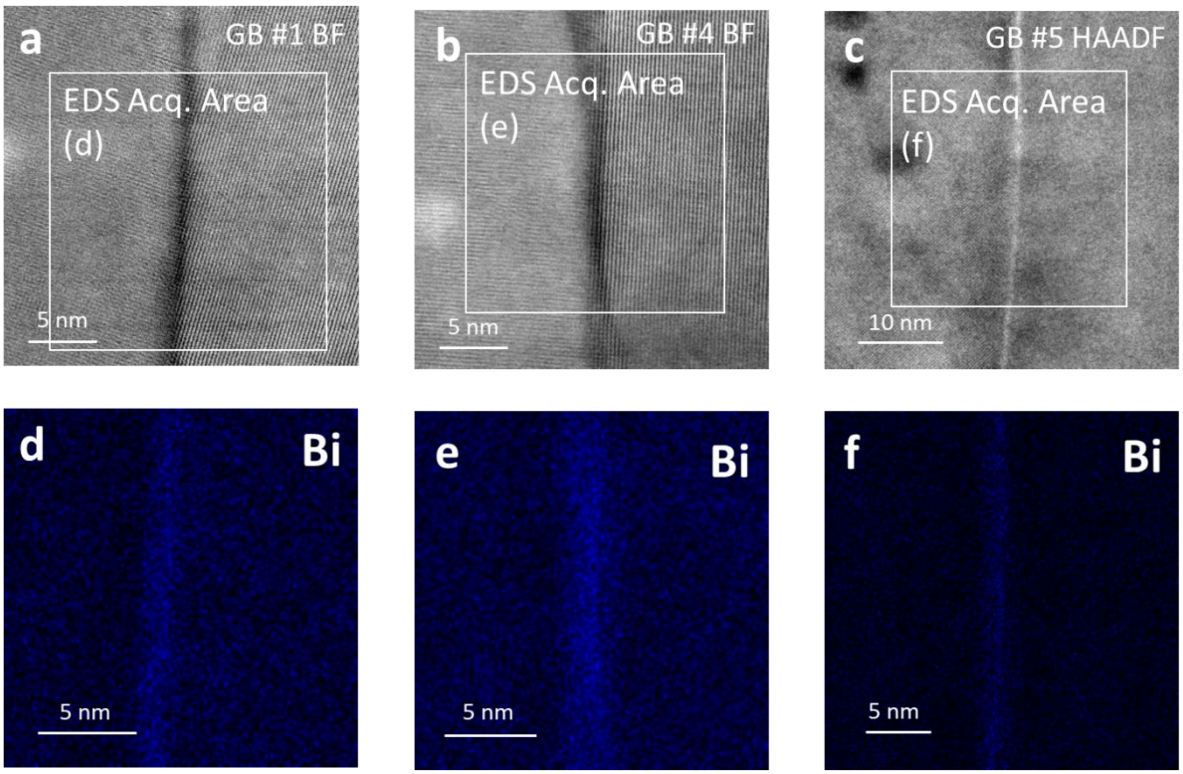

Figure 2.20 Cryo-STEM images and energy dispersive X-ray spectroscopy (EDS) elemental maps of three grain boundaries (GBs) randomly selected from the SnSb+Bi specimen.

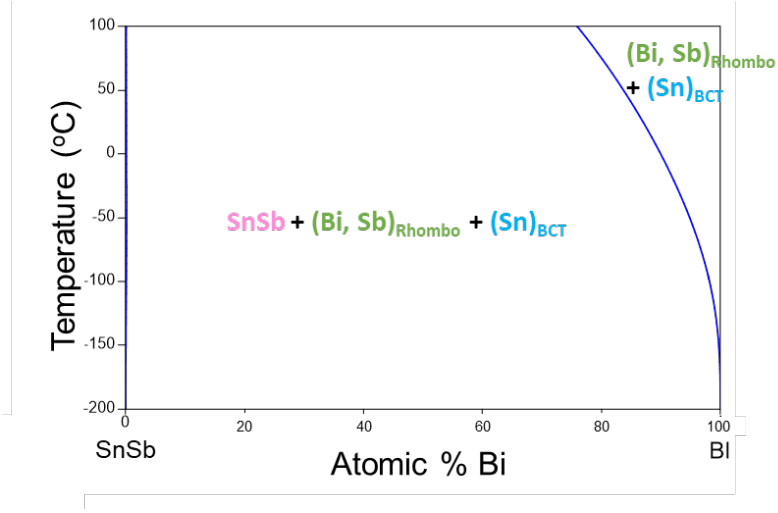

Figure 2.21 Computed isopleth of SnSb-Bi from 100 °C to -200 °C. There is no phase transformation for SnSb + 2.8 at% Bi below room temperature.

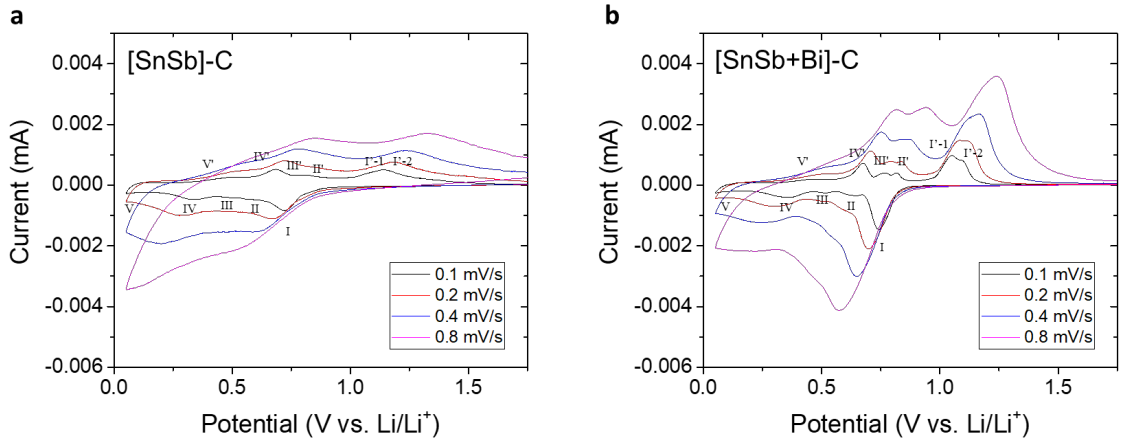

Figure 2.22 Cyclic voltammograms of (**a**) [SnSb]-C and (**b**) [SnSb+Bi]-C composite anodes at 0.1 mV/s (the 5th cycle), 0.2 mV/s, 0.4 mV/s and 0.8 mV/s between 0.05 and 1.5 V vs. Li/Li+. The lithiation reactions of SnSb includes (I) $SnSb + 3\ Li \rightarrow Li_3Sb + Sn$, (II) $Sn + 0.4\ Li \rightarrow 0.2\ Li_2Sn_5$, (III) $0.2\ Li_2Sn_5 + 0.6\ Li \rightarrow LiSn$, (IV) $LiSn + 1.5\ Li \rightarrow 0.5\ Li_5Sn_2$, (V) $0.5\ Li_5Sn_2 + 1.9\ Li \rightarrow 0.2\ Li_{22}Sn_5$. Upon de-lithiation, the reaction process can be summarized as (V') $0.2\ Li_{22}Sn_5 \rightarrow 0.5\ Li_5Sn_2 + 1.9\ Li$, (IV') $0.5\ Li_5Sn_2 \rightarrow LiSn + 1.5\ Li$, (III') $LiSn \rightarrow 0.2\ Li_2Sn_5 + 0.6\ Li$, (II') $0.2\ Li_2Sn_5 \rightarrow Sn + 0.4\ Li$, (I'-1) $Sn + Li_3Sb \rightarrow SnSb + 3\ Li$, and (I'-2) $Li_3Sb \rightarrow Sb + 3\ Li$. See Figure 3 in the main text where these reactions are labeled.

Acknowledgments

This work is supported as part of the Center for Synthetic Control Across Length-scales for Advancing Rechargeables (SCALAR), an Energy Frontier Research Center funded by the United States Department of Energy, Office of Science, Basic Energy Sciences under Award No. DESC0019381. Use of the Stanford Synchrotron Radiation Light source, SLAC National Accelerator Laboratory, is supported by the U.S. Department of Energy, Office of Science, Office of Basic Energy Sciences, under Contract No. DE-AC02-76SF00515. The authors acknowledge the use of shared TEM facility at the UC Irvine Materials Research Institute (IMRI), which is supported in part by the National Science Foundation through the UC Irvine Materials Research Science and Engineering Center (UCI MRSEC DMR-2011967), as well as the Nano3/SDNI and IMCF facilities and instrumentation supported by the National Science Foundation (ECCS-1542148 and UCSD MRSEC DMR-2011924) at UC San Diego for specimen preparation.

Chapter 2, in part, is a reprint of the material "Thermodynamics-driven interfacial engineering of alloy-type anode materials", Q. Yan, S. Ko, A. Dawson, D. Agyeman-Budu, G. Whang, Y. Zhao, M. Qin, B. Dunn, J. Weker, S. Tolbert, and J. Luo, as it appears in Cell Reports Physical Science, 2022, 3, 1. The dissertation author was the primary investigator and author of this paper.

Chapter 3. Cryogenic Milling Method to Fabricate Nanostructured Anodes

Introduction

The development of rechargeable energy storage systems has played a crucial role in advancing portable electronic devices and electric vehicles. For the past three decades, carbon-based anodes were mainly used due to their good electronic conductivity and cycling stability.[99] However, the theoretical gravimetric and volumetric capacities of graphite, 372m Ah/g and 756 Ah/L, are major limitations to attain higher energy density batteries. To further increase the cell energy density, researchers have studied Li-alloying reactions with metal or semi-metal elements and various intermetallic compounds. Various strategies, such as nanoporous structures,[5,16,17] inactive matrix composites,[100,101] and carbon composites,[12–14] have been proposed to alleviate the extreme volume change (> 200%) during cycling.

To fabricate carbon composite structures, mechanical alloying via ball milling is widely used due to its simplicity. Several groups have demonstrated the successful synthesis of Sn-M-C composites (M = metal)[12–14] and Si-C composites[102–104] that showed higher specific capacity compared to the graphite anode. However, the volumetric capacities of these composites are often limited by the amount of carbon added. In 2005, Sony announced the "Nexelion" cell that utilized an amorphous Sn-Co carbon composite as the anode for a portable camcorder[105]. It improved the volumetric energy density by 10% compared to $LiCoO_2$/graphite cells[3]. While the composition of the anode material was not disclosed, researchers suggested a composition of Sn:Co:C = 3:3:4(mol) fabricated through high-energy ball milling (HEBM)[101,106,107]. This corresponds to 10 wt%, or 27 vol%, of graphite added during the ball milling process. While the added carbon can help to alleviate the volume expansion from the cycling process, it decreases the full cell volumetric energy density. Unfortunately, due to the heat generated from the ball milling process,

decreasing the carbon content in traditional HEBM can increase cold-welding of the metal grains, especially for the low melting temperature metals such as Sn. This can increase both the grain size and the secondary particle size[108], which are undesirable for battery applications[3,4]. Therefore, a new processing route is needed to fabricate anode particles with desired micro- and nano-nanostructures.

In this study, we demonstrate a new route using cryogenic milling (cryomilling) to fabricate nanostructured alloy anodes. Cryomilling is a cost-effective manufacturing method that is already widely used in the food industry,[109,110] in polymer powder synthesis,[111] and in the fabrication of nanostructured alloys.[112] Due to the presence of a ductile-to-brittle transition for many materials at low temperatures, cryomilling can efficiently alleviate cold-welding and reduce the grain and particle size[113]. Previous studies have also suggested that cryomilling can promote the uniform distribution of various types of carbon between metal grains for mechanical properties enhancements[84,114,115]. To demonstrate the feasibility and the benefits of cryomilling on the fabrication of battery anode materials, the SnSb intermetallic was selected as a model system. SnSb has attracted considerable attention due to its high theoretical capacity of 825 mAh/g. Additionally, researchers have found the two-step lithiation reaction of SnSb can create a Li_3Sb matrix structure to buffer the volume expansion and improve the cycling stability[24,25,116]. However, cracks can often form in micrometer-size SnSb particles during cycling, resulting in capacity decay upon cycling[25].

Here, we compare the synthesis of SnSb-C composite using three ball milling methods: high-energy ball milling or HEBM, (lower energy) planetary ball milling, and cryomilling. SnSb-C composite fabricated with HEBM showed severe cold-welding and an average particle size > 100 μm. The composite made with the planetary ball milling demonstrated poor cycling stability. In contrast, cryomilling led to the synthesis of high-energy density SnSb-C anode in one step.

Aberration-corrected scanning transmission electron microscopy (AC STEM) and post-cycling SEM revealed that the refined grain size and well-dispersed carbon nanoplatelets effectively alleviate the volume expansion and prevent particle cracking after cycling. This work thus demonstrates a new and potentially general method to fabricate practical nanostructured battery electrodes that can be applied to various materials.

Experimental Section

Material Synthesis

The SnSb-C composites were prepared by various ball milling routes. 48.78 wt% Sn (Alfa Aesar, 99.80%, 325 mesh), 50.02 wt.% Sb (Alfa Aesar, 99.5%, 200 mesh), and 1.2 wt% graphite (MTI) were used as starting materials. For cryomilling, 1.3 g starting material was placed in a stainless-steel jar (50 ml) with 5 stainless-steel balls (5 mm diameter) inside an Ar-filled glovebox. After sample is pre-cooled for 15 min, the milling process was performed for 4 h @25 Hz (1500 min^{-1}) (8 cycles of 25 min each with an intermediate cooling of 5 min) using a Retsch Cryomill. The jar is cooled with liquid nitrogen circulation during the pre-cooling and milling process. The milling temperature was constantly monitored with an "Autofill system" from the cryomill machine. For high-energy ball milling, 1.3 g starting material was placed in a stainless-steel jar (65 ml) with 6 stainless-steel balls (5 mm diameter) inside an Ar-filled glovebox. The milling process was performed for 4 h @1200 min^{-1}(8 cycles of 25 min each with resting of 5 min) using a SPEX-8000D Mixer/Mill at room temperature. For planetary ball milling, 5 g starting material was placed in an yttrium stabilized zirconium oxide (YSZ) grinding jar (100 ml) with 12 YSZ grinding balls (10 mm diameter) inside an Ar-filled glovebox. The milling process was performed for 8 h @400 rpm (16 cycles of 25 min each with resting of 5 min) using a Across International PQ-N04 planetary ball mill at room temperature.

For sample comparison, the processing parameters (ball-to-powder ratio, jar volume/geometry, ball/jar material, milling time, and speed) of cryomilling and HEBM are similar. Therefore, the resulting powder comparison between HEBM and cryomill can demonstrate the benefits under cryogenic temperature.

Material Characterization.

Scanning electron microscopy (SEM) images were taken with a FEI Apreo SEM operated at 5 kV. To characterize the crystal structure of the synthesized SnSb-C composite, X-ray powder diffraction (XRD) was conducted using a Bruker D2 Phaser (Cu Kα radiation, λ = 1.5406 Å) with scanning rate of 0.5 °/min. The grain size was calculated using the Scherrer Equation, and instrument peak broadening equals 0.1°. Single peak calculation at 29.1° was performed. The pattern at 41.5° and 51.4° were combination of two diffraction peaks; therefore, a large estimated error was expected, and the calculation was not performed. N_2 porosimetry was conducted with a Micrometritics TriStar II 3020. The sample pore volume was calculated from the adsorption branch of the isotherm using the Braet-Joyner-Halenda (BJH) model. Raman spectroscopy was taken using a Renishaw Raman with 633 nm laser. The transmission electron microscopy sample was fabricated with a dual-beam focused ion beam (FIB)/SEM system using a FEI Scios. The microstructures and elemental distribution of the cryomilled composite were further studied with aberration-corrected scanning transmission electron microscopy (AC-STEM) using a JEOL JEM-300CF STEM microscope operated at 300 kV with double correctors and dual large angle energy dispersive X-ray spectroscopy (EDS) detector. The STEM and EDS data processing was performed with DigitalMicrograph (DM). For post-cycling particle morphology SEM characterization, the electrode after electrochemical cycling was disassembled using an MTI hydraulic crimper equipped with disassembling die inside an Ar-filled glovebox. The obtained

electrode was rinsed with diethyl carbonate (DEC) solvent to remove residual electrolyte, and then dried inside glovebox antechamber under vacuum for 30 min. To ensure air-free transfer into the SEM chamber, the sample is sealed inside a QuickLoader (FEI) in the glovebox and directly load into the SEM chamber.

Electrochemical Characterization

Each type of ball milled SnSb-C was mixed with carbon fiber (pyrolytically stripped, >98% carbon basis, $D \times L$ = 100 nm × 20-200 μm) and carboxymethyl cellulose (CMC, MTI Corp) in water at a mass ratio of 8:1:1 using a Thinky mixer (ARE-310) for 2 h at 2000 rpm. The resulting homogeneous slurry was casted on a copper foil (9 μm thick, MTI Corp) using a doctor blade and an automatic tape casting coater at a constant traverse speed of 10 mm/s. The casted tape was first dried in air for 12 h then dried in a vacuum oven at 80 ºC for 12 h. After drying, the electrode was then punched into 11 mm discs and weighed individually. The average active material (SnSb-C composite) loading was 1.50 mg/cm^2. 2032-type coin cells were assembled with Li metal disc as counter/reference electrode and Celgard 2320 polypropylene membrane as separator. The electrolyte consists of 1 M LiPF6 in a 1:1 ethylene carbonate/diethyl carbonate solvent (LP40, Sigma-Aldrich) with 5 vol% fluorinated ethylene carbonate (FEC, Sigma-Aldrich). Galvanostatic cycling was conducted using a Lanhe battery cycler in the potential range of 0.05-1.5 V vs. Li^+/Li at various current rates (listed in figures). The gravimetric capacity was calculated based on the loading of the active material (SnSb-C composite).

Results and Discussion

The cryomilling process used in this study based on having liquid nitrogen (LN_2) circulate outside the ball milling jar to continually cool the milling process (Figure 3.1 b). This process can be viewed as a high-energy shaker mill with automatic LN_2 cooling. The ball mill jar was cooled

to -196ºC before the milling process. Additionally, 5 minutes of cooling was carried out after 25 minutes of ball milling to ensure the cryogenic processing temperature. The cryomilling process was first optimized with various milling times. Sn and Sb particles were added in 1:1 mol ratio with 1.2 wt% graphite. The starting composition was kept the same for all ball milling process. After 1 h of cryomilling (2×25 min milling with 5 min intermediate cooling), unmixed graphite could still be observed in the SEM images, indicating insufficient mixing. Sn (ICSD-106072) and Sb (ICSD-64695) phases were also seen in the product based on X-ray diffraction (XRD), further signifying that longer processing time was required. When the milling time increased to 4 h, SnSb particles with maximum diameters of 7 μm could be observed in the SEM image (Figure 3.2 a, Figure 3.11 a). The average particle size was estimated to be 1.84 ± 1.29 μm as shown in Figure 3.12 a. In addition, no graphite flakes could be found, indicating most of the graphite was exfoliated and mixed between the grains. The diffraction patterns of the 4 h cryomilled sample could be indexed with SnSb (ICSD-154085) in the $R\bar{3}m$ space group. The diffraction peaks corresponding to Sn and Sb mostly disappeared after 4 h of cryomilling, with only trace Sb diffraction remaining. The dominant SnSb diffraction peaks also became broader. This indicates cryomilling can be used to synthesize fine-grained SnSb particles.

For comparison, HEBM and planetary ball milling were carried out with similar processing parameters (see Experimental Section). The resulting morphology and XRD comparison of SnSb-C composites are shown in Figure 3.1 a, c, and d. All the ball milling process resulted in the formation of SnSb. After 4 h of HEBM (8 × 25 min milling with 5 min intermediate rest), large particles of more than 100 μm diameters could be commonly observed (Figure 3.1 a, Figure 3.11 e), indicating severe cold-welding during the milling process. The average particle size was estimated to be 22.12 ± 28.91 μm as shown in Figure 3.12 c. Since planetary ball milling has lower

energy, 8 h (16 × 25 min with 5 min intermediate rest) was required to mechanically alloy SnSb phase. The lower mixing energy also alleviated the cold-welding effect and resulted in smaller particle diameters (Figure 3.1 c, Figure 3.11 c). The average particle size was estimated to be 2.54 ± 1.96 μm as shown in Figure 3.12 b. However, the lower milling energy also results in uneven mixing of graphite with the metal powder. In Figure 3.6, graphite flakes could still be observed after an 8 h planetary ball milling process. An additional benefit of the LN_2 cooled shaker mill is that 4 h of cryomilling produced < 7 μm diameter particles with no obvious graphite observed. Moreover, the cryomilled powder showed broader diffraction peaks, which indicates a finer grain size (Table S1). Using the Williamson-Hall method, the averaged grain size of the cryomilled powder was estimated to be 23.5 nm, which was smaller than the averaged grain sizes of the samples from HEBM (41.7 nm) and planetary ball milling (59.2 nm). The estimated strain of the cryomilled powder was 0.0020, which was also smaller than the strain of the HEBM sample (0.0028), and planetary ball milling (0.0030).

The cryomilled and planetary ball milled sample porosity was characterized with nitrogen porosimetry. The N_2 adsorption-desorption curves in Figure 3.7 a and 3.7 b shows type II isotherm, which indicates both samples are mostly non-porous. Using the Barrett-Joyner-Halenda (BJH) method, the cumulative pore volume of the cryomilled and planetary ball milled sample were calculated to be 0.0044 cm^3/g and 0.0058 cm^3/g, respectively, which also match the observed mostly dense particles from the SEM images for both samples. This shows that the cycling stability is not likely affected by the sample porosity.

To characterize the underlying nanostructures of the milled powder, a focused ion beam (FIB) was used to lift-out a lamella sample from the powder to use for cross-sectional STEM characterization. AC STEM high-angle annular dark field (HAADF) images (Figure 3.2 c) showed

mostly fiber-like fine-grained SnSb (bright region) reinforced with a carbon structure (dark region). After zooming in, the bright-field images (Figure 3.2 d, e) showed majority of the SnSb grains are elongated and has width around 20 nm. In addition, ~3 nm thick multilayer graphene layers were observed between the grains. This indicated that cryomilling could exfoliate bulk graphite powder into nanometer-thick nanoplatelets and disperse this nano-graphite homogeneously within the SnSb grains. Based on Figure 3.2 c, the averaged carbon thickness with the cryomilled sample was 3.62 ± 2.01 nm, with the maximum measured carbon thickness being 11.04 nm (Figure 3.10). The atomic resolution HAADF image (Figure 3.2 f) further shows an interplanar spacing of 0.217 nm, which corresponds to the (012) orientation of SnSb. The distribution of SnSb and carbon was further confirmed with STEM EDS mapping, as shown in Figure 3.3. Sn and Sb are relatively evenly distributed, as shown in the HAADF image in Figure 3.3 a. The carbon EDS mapping (Figure 3.3 b) confirms that the dark region in the HAADF image corresponds to the carbon matrix structure.

Sn and Sb EDS mapping (Figure 3.3 c,d) confirms the colocalization of Sn and Sb, but also shows some Sb-rich regions, in agreement with the small amount of residual Sb diffraction in figure 3.1 d. The EDS spectrum fitting showed that there are 4.0 at% C, 51.2 at% Sn, and 44.8 at% Sb, which can be well correlated to the designed composition. The small domain size of this material shows the feasibility of using cryomilling to fabricate high nanostructured carbon composite alloy anodes. It should be noted that for these cryomilled SnSb-C composites, there still exists regions with higher Sb content (Figure 3.3 d) and inhomogeneous grain sizes (Figure 3.2 b), both of which are indications of insufficient mixing. Further fine-tuning of processing parameters is ongoing to optimize microstructure homogeneity.

To evaluate the potential of these materials as high energy density anodes, the electrochemical performance of the SnSb-C composites synthesized with planetary ball milling and cryomilling was compared using galvanostatic cycling. The particle size of HEBM SnSb-C composite was greater than 100 μm; therefore, poor electrochemical performance was expected, in part due to inhomogeneous slurry mixing and tape casting. Additionally, large particles are known to easily fracture during cycling,[3] and they can even penetrate the separator and cause battery shorting. Because of this, these samples were not studied further. The 4 h cryomilled composites showed higher coulombic efficiency (99.6% vs. 97.5%) and cycling stability, which likely benefit from the smaller grain size, formation of SnSb phase, and evenly distributed carbon matrix. The cryomilling and planetary ball milled samples have initial lithium capacity of 708 mAh/g and 697 mAh/g, respectively (Figure 3.4 b), which is lower than the SnSb theoretical capacity of 825 mAh/g. The lower values are due to the higher voltage cutoff (0.05-1.5V) used to prevent lithium plating. The cryomilled SnSb-C showed a distinct voltage plateau during cycling (Figure 3.4 b), indicating that most of the charge storage happens through well-defined alloying reactions. Figure 3.4 a showed that the planetary milled SnSb-C composites lost 73% of capacity after 150 cycles with a coulombic efficiency that varied between 97.5 and 98.8%. In comparison, the cryomilled SnSb-C composite showed 84% capacity retention after 150 cycles with averaged coulombic efficiency of 99.6 ± 0.3% (Figure 3.4 a).

The rate capabilities of the cryomilled and planetary ball milled samples are shown in Figure 3.4 c. When the cycling current is increased to 200 mA/g, 500 mA/g, and 1 A/g, the cryomilled sample demonstrated charge capacity of 598 mAh/g, 537 mAh/g, and 415 mAh/g, respectively, which corresponds to 86%, 78%, and 60% of the charge capacity at 100mA/g, respectively. In contrast, the planetary ball milled composite only showed charge capacity of 541

mAh/g, 428 mAh/g, 266 mAh/g, respectively, which corresponds to 77%, 61%, 38% of the charge capacity at 100 mA/g. When the current density was returned to 100 mA/g after being subjected to currents as high as 1 A/g, the lower specific capacity values suggest possible electrode microstructure damage after high rate cycling. To further evaluate the cryomilled SnSb-C electrode kinetics, cyclic voltammetry (CV) was also conducted (Figure 3.4 d). The response correlates well to the galvanostatic cycling results. The first CV cycle showed a reduction peak at 0.5V, which can be assigned to the formation of Li_3Sb phase and solid electrolyte interface (SEI) layer[24,117]. The remaining reduction peaks from 0.4 V to 0.05 V could be labeled with the formation of Li-Sn intermetallic including Li_2Sn_5, LiSn and $Li_{4.4}Sn$[3]. At Cycle 2 and 3, the change in the first reduction peak potential corresponds to the phase separation of the Sb and Sn. The redox peak current densities are mostly unchanged for the 2nd and 3rd CV cycle, thereby indicating good cycling stability of the cryomilled SnSb-C composite electrode.

To evaluate the effectiveness of the nanostructure on alleviating crack formation, the morphology of the composites was evaluated using SEM for the first lithiation and after 20 cycles (Figure 3.5). After the initial lithiation, minor cracks could be found for the large particles (>5 μm) in the planetary ball milled sample shown in Figure 3.5 e, but not in the cryo-milled sample. After 20 cycles, severe cracking and complete particle fracture were commonly found in single-particle SEM images throughout the electrode for the planetary ball milled sample, as shown in Figure 3.5 f. Severe particle fracture exposes fresh surface which can cause excessive SEI formation with electrolyte, which explains the observed low Coulombic efficiency and fast capacity fade for the planetary ball milled composite.

For the cryomilled sample, surface bulges were observed on particle after initial lithiation, indicating volume expansion from the alloying reaction. However, no obvious cracking could be

easily spotted in the SEM images (Figure 3.5 b), which demonstrates the effectiveness of the carbon matrix structure and the refined grain size. When the cryomilled composite was cycled for 20 cycles, the particle surface became noticeably rough (Figure 3.5 c) and some minor surface cracks could be spotted for the larger particles. Nevertheless, most particles still maintain their shapes and no complete fracture could be observed. This improved post-cycling morphology was consistent with the improved electrochemical stability of the cryomilled SnSb-C composite.

As previous reviews have pointed out, the volumetric energy density of many alloy type carbon composite anodes can be limited due to the large volume of low-density carbon and internal porosity.[3,4] The present research demonstrates that cryomilling can be utilized for facile fabrication of high energy density anodes. The cryomilled SnSb-C composite is mostly non-porous (0.0044 cm^3/g porosity), and it has a gravimetric capacity of 669 mAh/g after 50 cycles at 100 mA/g. Using the density of graphite (2.2 g/cm^3) and fully lithiated SnSb (2.78 g/cm^3), the composite demonstrates a volumetric capacity q_R^- of 1842 Ah/L, which shows significant improvement compared to a graphite anode (756 Ah/L). For energy storage applications in portable electronics and electric vehicles, it is more important to compare the improvements on full cell energy density.[3,118] Active material porosity, average voltage, irreversible capacity, and coulombic efficiency all have significant impacts on cell energy density and performance.

By adopting the cell-based model proposed by Obrovac et al.,[3] the stack energy can be calculated by the assumption that the anode electrode contains 70 vol% SnSb-C, and the anode irreversible capacity matches that of the cathode. $LiCoO_2$ was selected as the baseline cathode that has a reversible volumetric capacity q_R^+ of 530 Ah/L, and an average voltage V_{avg}^+ of 3.9V. The N/P ratio (capacity ratio of the negative and positive electrode) was set to be 1.1. The cryomilled

SnSb-C composite has an average voltage V_{avg}^{-} of 0.75V. Using these data and assumptions, the stack energy U_R can be calculated to be 855 Wh/L based on the following equation:[3]

$$U_R = \frac{2q_R^+ t^+}{t_{cc}^+ + t_{cc}^- + 2t_s + 2t^+\left[1+\frac{q_R^+}{q_R^-}\left(\frac{N}{P}\right)\right]}(V_{avg}^+ - V_{avg}^-),$$

where the cathode current collector thickness t_{cc}^+ and anode current collector thickness t_{cc}^- were set to 15 μm, the separator thickness t_s was set to 20 μm, and the cathode electrode thickness t^+ was set to 55 μm. Based on this full cell model, an 18% increase in the stack level volumetric energy density can be obtained with the cryomilled SnSb-C composite compared to the baseline LCO/graphite cell (726 Wh/L).[3] Note that the volumetric energy density of the modeled cell with cryomilled SnSb-C anode is likely to be higher since ~250% volume expansion was assumed based on the theoretical density differences between SnSb and fully-lithiated SnSb to prevent overestimation. A more reliable estimation of the anode volume expansion and energy density will be conducted in the future using *in-situ* transmission X-ray tomography (TXM) studies during electrochemical cycling.[25,72]

Based on the structural and electrochemical characterization, the major improvement in cycling stability of the SnSb-C composite can be attributed to the nanostructures from the cryomilling process, namely the refined grain size and the well-dispersed graphite within the SnSb. Fecht et al. proposed an empirical description of the microstructure development during ball milling in three stages:[119] 1) localized deformation occurs in shear bands (the region with a high dislocation density), 2) after a certain strain level is reached, nanometer-sized sub-grains form via dislocation recombination, and 3) randomly oriented single-crystalline grains recrystallize from the sub-grain structure. The competing process of dislocation generation during plastic deformation and grain recovery by thermal effects determines the minimum grain size achievable of the milling process.[120] At cryogenic temperature, the recovery, recrystallization, and grain

growth can be limited. Therefore, a fine-grained structure can be achieved with shorter milling time.[112,121] A theoretical dislocation model for milling minimum grain sizes also suggests a decrease in grain size with lower milling temperature.[122] SnSb sample without carbon addition was fabricated via HEBM and cryomill, as shown Figure 3.8. Using W-H analysis, the grain size of the cryomilled SnSb was estimated to be 43 nm with a strain of 0.0023. In comparison, the grain size of the HEBM SnSb was estimated to be 99 nm with a strain of 0.0034. These results further showed a decrease in grain size can be achieved with lower milling temperature under the same milling time.

In addition to allowing for the formation of nanoscale grains, cryomilling has another advantage when it comes to dispersing nanoscale carbon. Due to its high specific surface area and strong van der Waals interactions, both multilayered graphene and carbon nanotubes tend to stick together and form agglomerates, making them hard to disperse in the matrix structure.[123,124] Cryomilling has been shown to be an effective method to exfoliate graphite flakes into nanoplatelets[84] and prevent agglomeration[115,125] in nanocomposites. Various research groups have fabricated CNT reinforced aluminum matrix composites with good CNT dispersity and minimal sidewall defects using cryo-milling.[114,126,127] Similarly, in this work, the initial micron-sized graphite powder was exfoliated into nanoplatelets and evenly dispersed between the SnSb grains. Raman spectroscopy was also utilized to study the carbon structure of the samples fabricated from HEBM and cryomill, as shown in Figure 3.9. The 2D band of the HEBM sample has weak intensity due to the disordered structure.[128,129] The ratio of D and G band can be used to determine the structural defects in carbon materials.[130] I_D/I_G of the cryomilled sample was 0.82, which was much lower than the ratio of the HEBM sample (1.35). This showcased cryomill can reduce defects formation during milling process, which also correlates well with previous studies.[114,125,131]

Various forms of carbons, including graphite, graphene, CNT, and amorphous carbons are being widely used with high volume change anodes due to their ability to buffer volume changes using their internal void space or by creating wrinkled structure.[3,4] In this work, the well-dispersed nanoplatelets may also suppress grain growth and matrix phase coarsening (Li_3Sb) via grain boundary pinning.[112,115]

Conclusions

We have developed a facile synthesis method using cryogenic milling to produce stable, high energy density anode materials. SnSb-C composites were chosen as a model system to demonstrate the improvements on nanostructure and cycling stability. The cryomilled SnSb-C showed a specific capacity of 708 mAh/g and an initial Coulombic efficiency of 83%. After the first cycle, the anode showed an average Coulombic efficiency of 99.6 ± 0.3% and capacity retention of 90% over 100 cycles. Moreover, the composite anode has a reversible volumetric capacity of 1842 Ah/L, and an expected full cell stacking volumetric energy density is 855 Wh/L if $LiCoO_2$ was used as the cathode. This corresponds to an 18% increase compared to a baseline $LiCoO_2$/graphite cell. Based on STEM and post-cycling SEM analysis, the nanometer scale grain size and well-dispersed carbon matrix structure appears to reduce volume expansion and particle cracking during cycling. This work demonstrates the application of cryomilling on battery electrode materials and shows improved cycle life compared with materials obtained using conventional ball mill routes. Cryomilling can potentially become a general method for improving other battery electrode materials, thereby providing a pathway for developing high-performance energy storage systems.

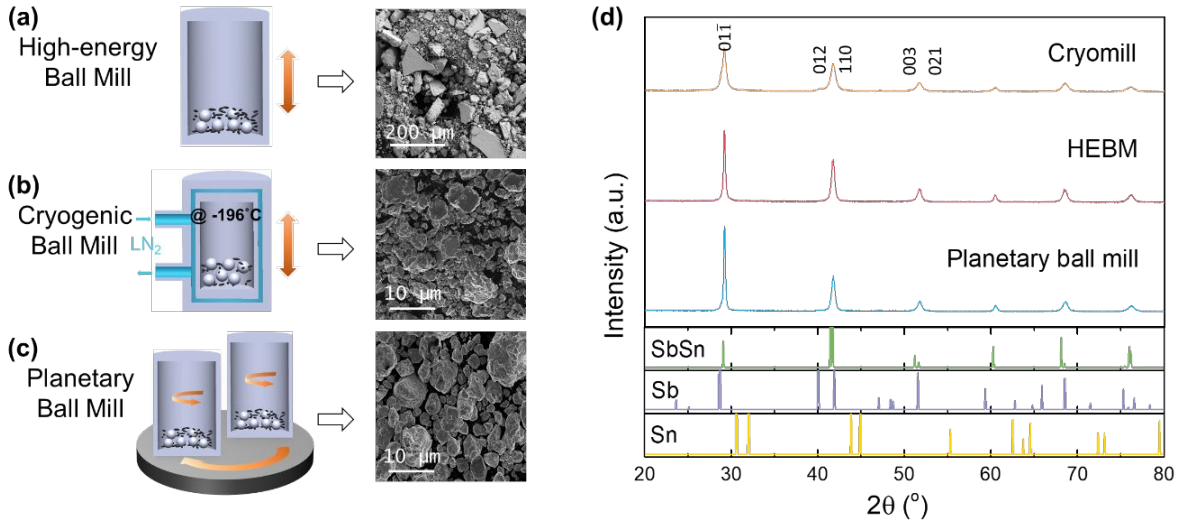

Figure 3.1 Synthesis method and SEM images of mechanical alloyed SnSb-C composite anodes fabricated through (a) high-energy ball mill, (b) cryogenic ball mill, and (c) planetary ball mill. (b) X-ray diffraction patterns comparing SnSb-C composite anodes synthesized through these three different mechanical methods. All methods produce SbSn, but the degree of crystallinity, as evidenced by the diffraction peak widths, varies dramatically between methods.

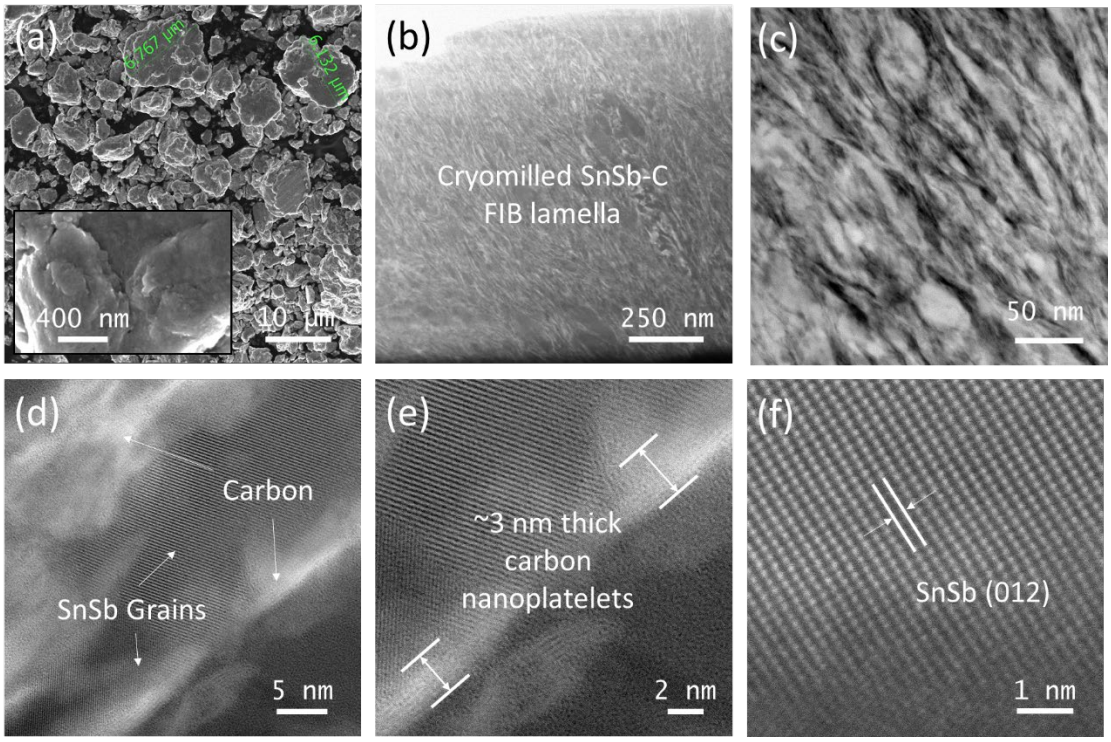

Figure 3.2 SEM and TEM micrographs of the cryomilled SnSb-C composite anode. (a) SEM image of the cryomilled SnSb-C. (b) low-mag bright field and (c) high-magnification STEM HAADF images revealing nanostructures in the cryomilled composite. (d) (e) high-magnification STEM bright-field images showing carbon nanoplatelets between the grains. (f) Atomic resolution STEM HAADF image of the SnSb grains.

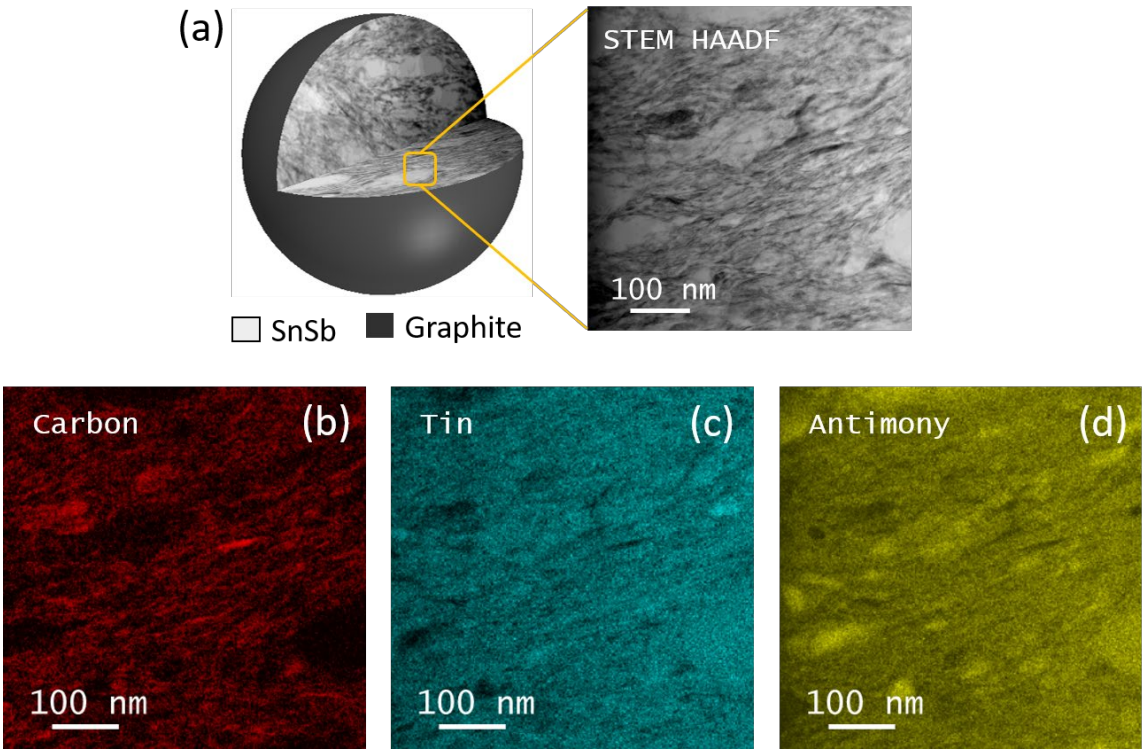

Figure 3.3 STEM image and EDS elemental maps of a cryomilled SnSb-C composite anode. (a) Schematic diagram and a STEM HAADF image of a cryomilled SnSb-C composite particle and the region where the EDS scan was performed. EDS elemental maps for (b) carbon, (c) tin, and (d) antimony.

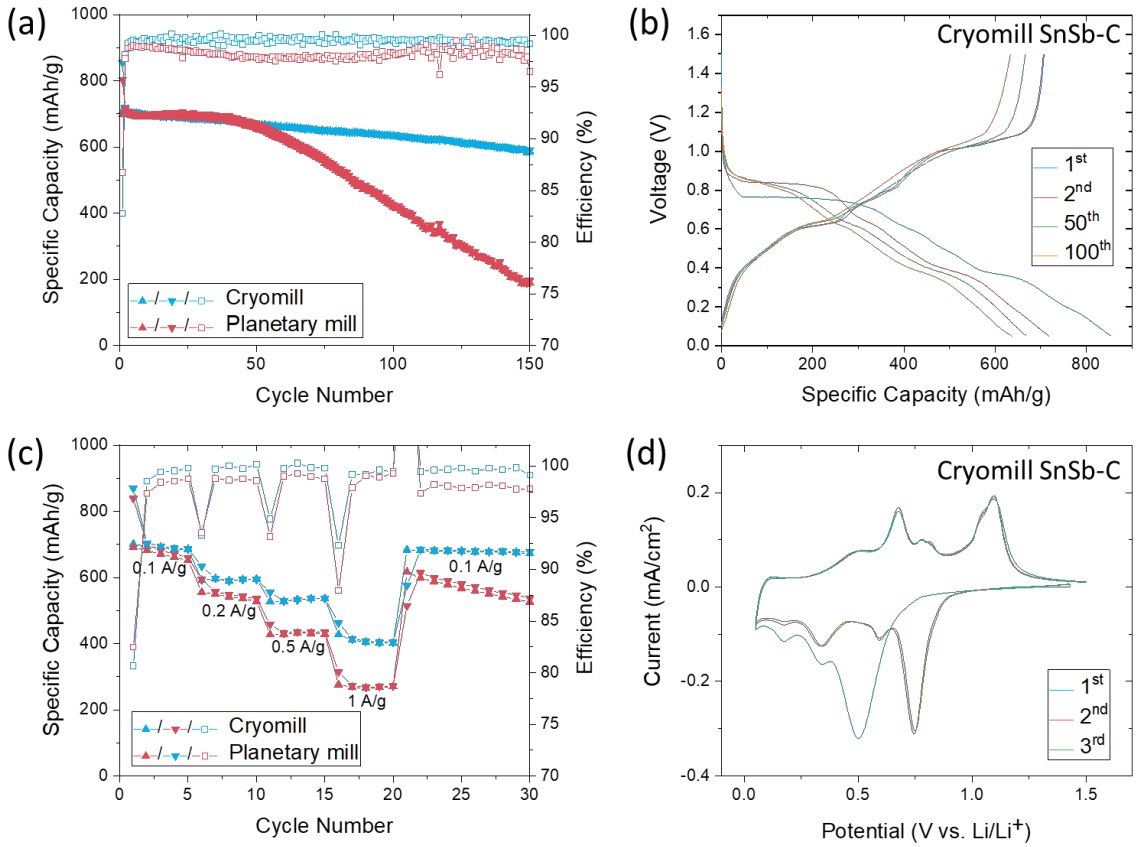

Figure 3.4 Electrochemical characterization of the cryomilled and planetary ball milled SnSb-C composite anodes. (a) Cycling stability for the cryomilled and planetary ball milled SnSb-C composite anodes cycled at 100 mA/g between 0.05-1.5V. (b) Voltage profiles of the cryomilled SnSb-C composite anode for the 1st, 2nd, 50th, and 100th cycle at 100 mA/g. (c) Rate performance comparison of cryomilled and planetary ball milled samples. (d) Cyclic voltammetry of the cryomilled SnSb-C composite anode at 0.1mV/s between 0.05 and 1.5 V.

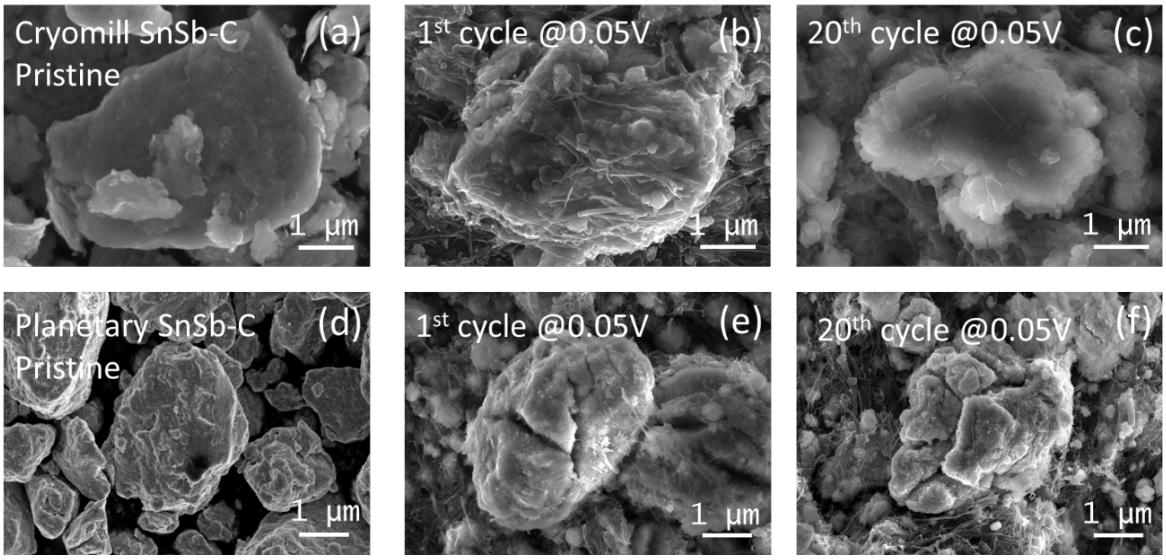

Figure 3.5 Comparison of the changes in morphologies upon cycling for cryomilled and planetary ball milled SnSb-C composite anodes. (a) The pristine cryomilled SnSb-C composite anode. Ex-situ SEM of cryomilled SnSb-C (b) after initial lithiation and (c) after 20 cycles. (d) The pristine planetary ball milled SnSb-C composite anode. Ex-situ SEM of planetary ball milled SnSb-C (e) after initial lithiation and (f) after 20 cycles. Cracking is observed in the planetary milled sample, but not in the cryo-milled material.

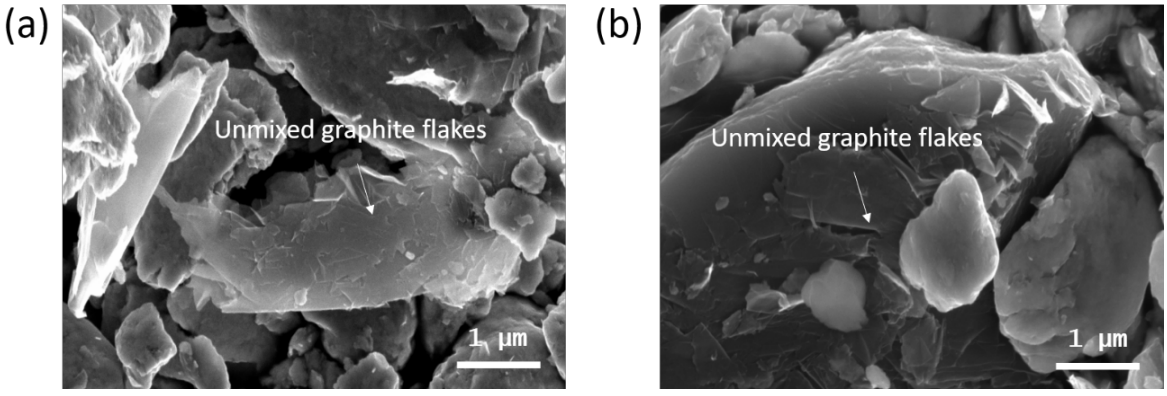

Figure 3.6 Unmixed graphite flakes found in the 8-hour planetary ball milled SnSb-C composite powder.

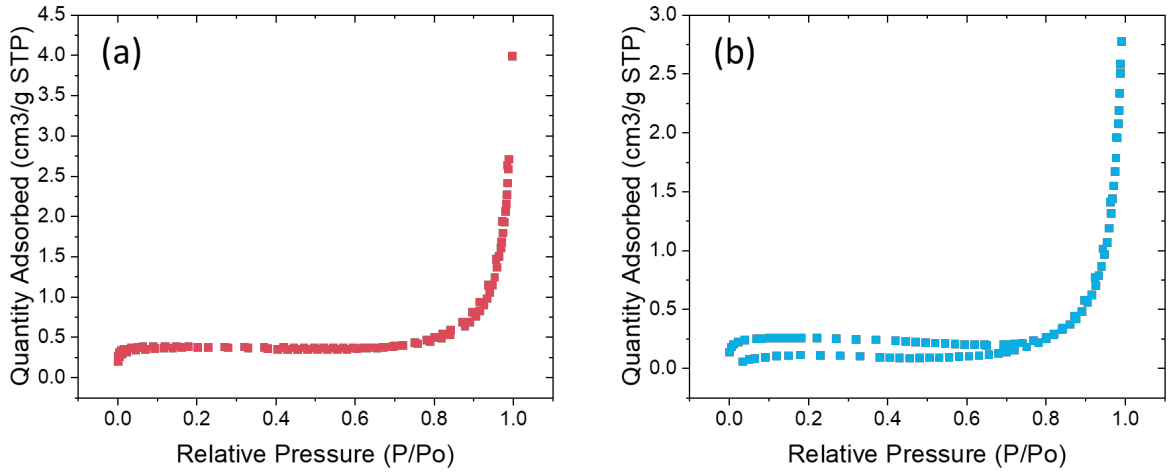

Figure 3.7 Absorption isotherm of (a) planetary ball milled sample and (b) cryomilled sample obtained from nitrogen porosimetry.

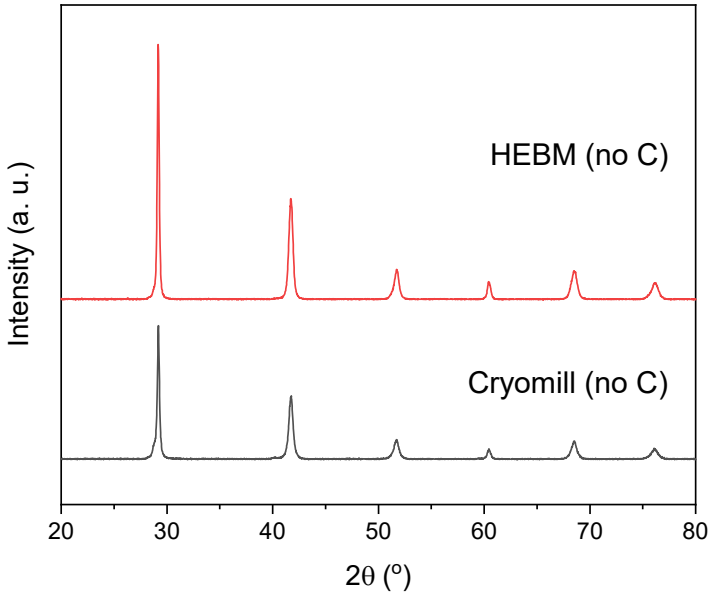

Figure 3.8 XRD comparison of the SnSb samples (without carbon addition) fabricated with high-energy ball mill and cryomill.

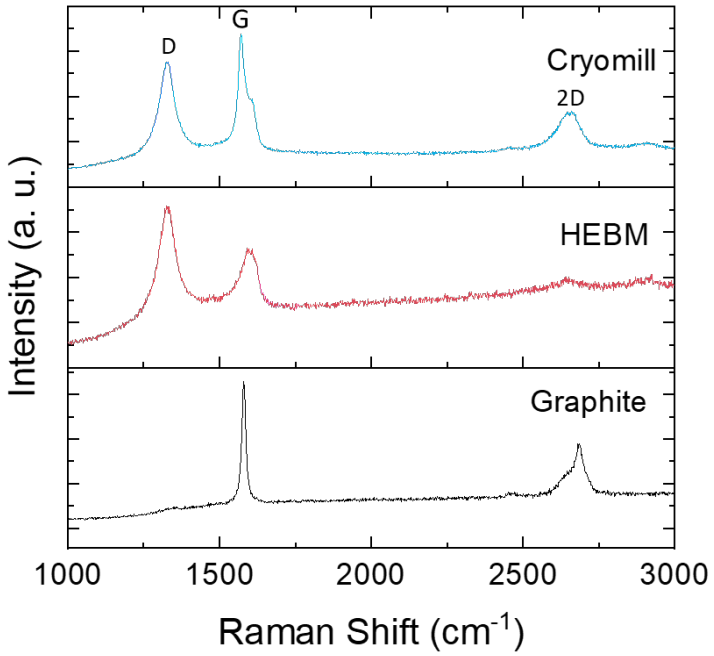

Figure 3.9 Raman spectroscopy comparison of the SnSb-C sample after cryomill and high-energy ball mill. The baseline is graphite sample without ball milling.

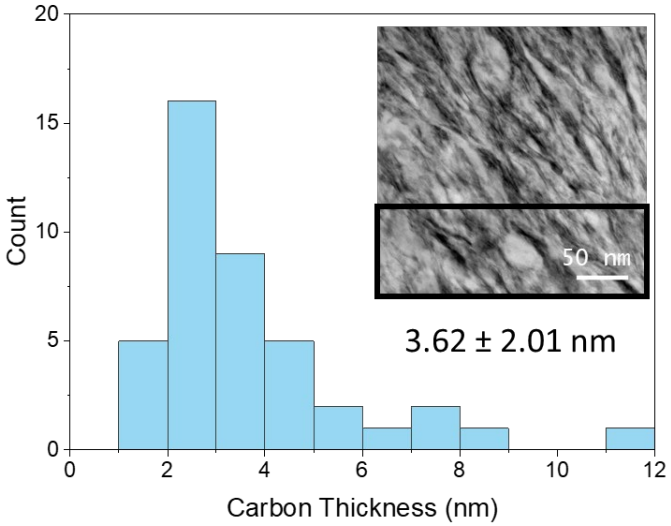

Figure 3.10 Measured carbon thickness histogram of the 4 hour cryomilled SnSb-C composite sample. 40 locations of carbon thickness were measured within the boxed region of the STEM HAADF image (Figure 3.2 c). Carbon corresponds to the dark contrast region in the HAADF image.

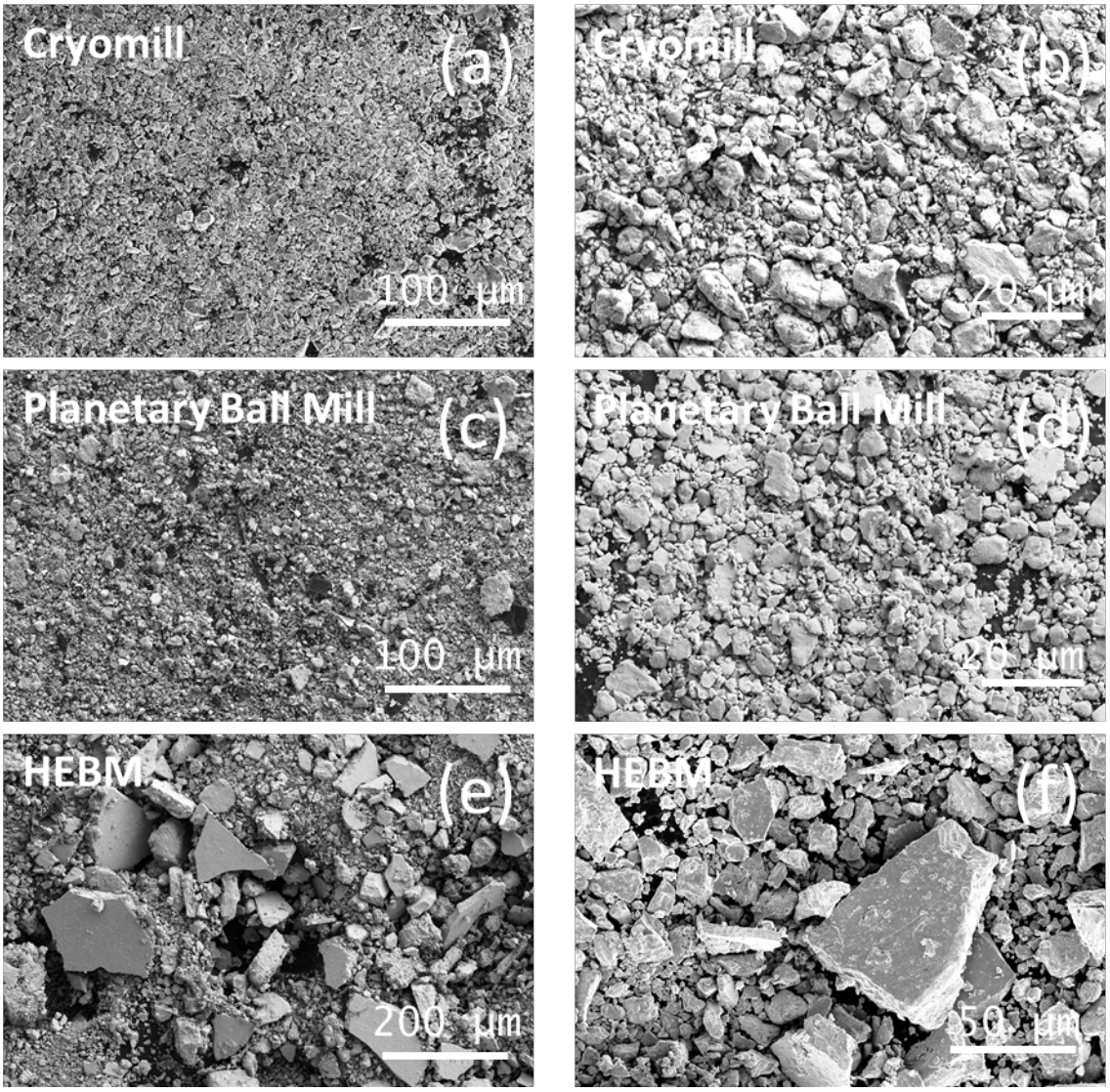

Figure 3.11 Low magnification SEM images of mechanical alloyed SnSb-C composite anodes fabricated through (a) (b) cryogenic ball mill, (b) (c) planetary ball mill, and (e) (f) high-energy ball mill.

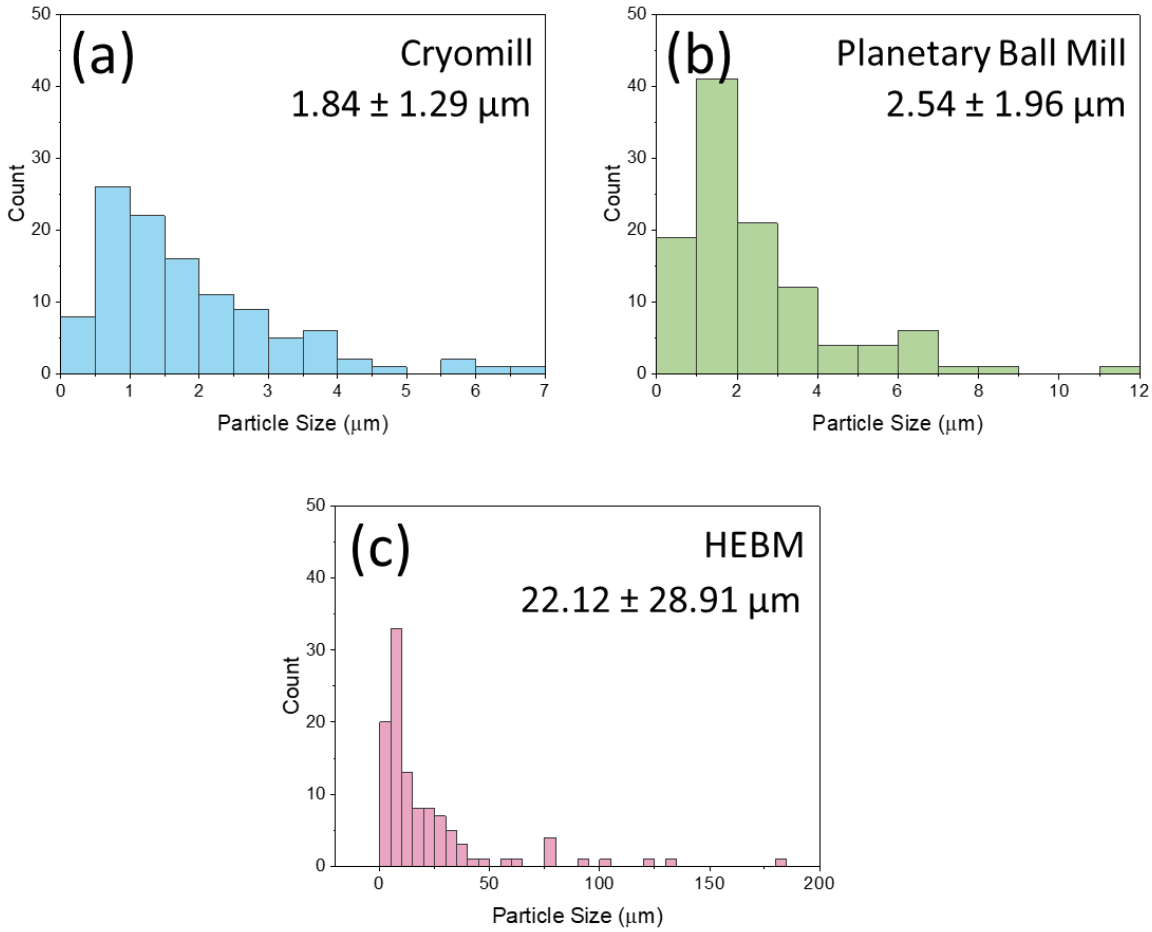

Figure 3.12 Particle size distribution of (a) cryogenic ball mill, (b) planetary ball mill, and (c) high-energy ball mill.

Acknowledgments

This work was supported as part of the Center for Synthetic Control Across Length-scales for Advancing Rechargeables (SCALAR), an Energy Frontier Research Center funded by the United States Department of Energy, Office of Science, Basic Energy Sciences under Award No. DESC0019381.

Chapter 3, in part, is a reprint of the material "Cryogenic Milling Method to Fabricate Nanostructured Anodes", Q. Yan, S. Ko, Y. Zhao, G. Whang, A. Dawson, S. Tolbert, B. Dunn, and J. Luo, as it appears in ACS Applied Energy Materials, 2020, 3, 11. The dissertation author was the primary investigator and author of this paper.

Chapter 4. Electric-Field-Assisted Bi Migration in Bi2O3-doped ZnO Polycrystalline Specimens

Introduction

Sintering, where the specimen microstructure and properties are dominated by temperature and time, is one of the main ceramic fabrication processes for thousands of years.[29] For the development of sintering technology, lower sintering temperature and shorter sintering time are always preferred, as these can increase the production rate and decrease energy consumption. In recent years, factors such as externally applied pressure and electric field have a growing importance in ceramic fabrication.[30–32] Spark plasma sintering (SPS), or field-assisted sintering technology (FAST) was developed back in the 1960s,[33] where the powder is placed in a conducting die under applied uniaxial pressure being rapidly heated with current (Joule heating of the die).[34–36] SPS/FAST is being demonstrated as a versatile consolidation method with generally decreased sintering time and temperature.[37,38] More recently, flash sintering was developed by Raj and colleagues in 2010 where electric field/current is applied onto the specimen to trigger rapid densification in 5 – 10 s at low furnace temperature,[39] and a broad range of ceramic materials was demonstrated to be compatible with this method. In general, the external applied electric field enables fast kinetics and low temperature process, which makes ceramics sintering become more energy-saving and cost-effective.

Electric field can also have many nonthermal effects on the specimen. For flash sintering, researchers have found electric field can induce anisotropic lattice expansion,[40] produce metastable phase,[41] and facilitate phase transformation[42] in selected systems. Aside from faster sintering, electric field can also induce microstructure evolution when applied to dense specimens. Chen and

colleagues have found the residual pores could migrate in the opposite direction of the applied electric field in 8 mol% Y2O3-stabilized ZrO2 (8YSZ).[43,44] Asymmetrical grain growth has also been observed in various systems, such as 3YSZ,[45] $SrTiO_3$,[46] and ZnO [47,48] after annealing under electric field. On the atomic level, Luo and colleagues have recently discovered that the applied electric current can change the microstructural evolution of Bi_2O_3-doped ZnO through an electrochemically induced grain boundary transition.[48] Specifically, when the electric field is applied to the sample, electrochemical reduction can occur on the negative electrode side and cause a grain boundary disorder-to-order transition to increase grain boundary diffusivities and induce abnormal grain growth. These interesting electric field effects can potentially enable new methods to tailor ceramic microstructure and grain boundaries.

Bi_2O_3-doped ZnO polycrystalline samples offer an ideal platform to investigate electric-field-assisted and interfacial-liquid-activated microstructural evolution. ZnO grains are electronic conducting (semiconductors), but the Bi-enriched GBs (nanoscale liquid-like interfacial phases) are ionic conducting. [132,133] When an electric field was applied to Bi_2O_3-doped ZnO polycrystalline samples, a number of interesting, far-from-equilibrium, kinetic processes can occur.[48,134] Here in Bi_2O_3-doped ZnO polycrystalline samples, we found the Bi-rich phase could migrate towards the negative electrode driven by the electric field. Consequently, the positive electrode side becomes essentially Bi-free after sufficiently long annealing, free of both the Bi-rich secondary phase and the Bi-enriched nanoscale liquid-like interfacial phase. This represents a new finding of the electric field effects on ceramic microstructure evolution of the unique GB ionic conducting systems.

Experimental Procedures

Electric field assisted sintering experiment

For sample fabrication, 0.5 mol% Bi_2O_3 – doped ZnO powders were made by ball milling ZnO (99.98% purity, 18 nm, US Nanomaterials) with bismuth acetate (≥99.99% purity, Sigma Aldrich) in isopropyl alcohol for 10 hours using a PQ-N04 planetary ball mill (Across International). The milled powders were dried in an oven for 12 hours at 80 ºC, and subsequently annealed for 1 hours at 500 ºC. Then, the treated powders were loaded into a graphite die lined with graphite foils and fabricated into dense pellets using a Thermal Technologies 3000 series SPS in vacuum (10^{-2} Torr) at 780 ºC for 5 min with uniaxial load of 50 MPa. The pellets were de-carbonized by annealing in air at 700 ºC for 9 hours. The resulting pellets reached >99% relative densities, and the pellets were ground to about 4 × 3 × 1.5 mm^3. To form electrodes on the sample, the pellets were sputtered with Pt using a Denton Discover 18 Sputter.

For the electric-field-assisted sintering experiment, an external DC current was applied across the sample at 840 ºC for 4 hours while maintaining a constant voltage of 2 V (or ~12.1 V/cm and ~17.6 mA/mm^2). The sample temperature was estimated to be ~870 ºC due to Joule heating. The current and electric potentials were recorded using a Tektronix DMM 4040 digital multimeter.

Materials Characterization

The specimen microstructure was studied using an Thermo Scientific Apreo SEM with an Oxford Symmetry EBSD detector. The TEM lamellas were fabricated using a Thermo Scientific Scios dual-bream FIB/SEM system. The grain boundary structure and elemental information were studied with JEOL JEM-300CF STEM microscope operating at 300 kV.

Results and discussion

The experiment was carried out by applying a constant 12.1 V/cm electric field on the Bi_2O_3-doped ZnO polycrystalline specimen for 4 hours. After the field-assisted sintering process,

there is obvious abnormal grain growth in the negative electrode side as shown in the Figure 4.1 b overview cross-sectional scanning electron microscopy (SEM) image and Figure 4.1 f negative electrode side zoom-in SEM image. Cross-sectional electron backscatter diffraction mapping was carried out to quantify the grain size from the positive side to the negative side as shown in Figure 5.2 a and c-e. Grains on the positive electrode side have an average grain diameter of 1.7 ± 0.7 μm (volume-weighted). In contrast, grains on the negative electrode have an average grain diameter of 58 ± 30 μm (volume-weighted), which is more than 30 times that on the positive electrode side. The cross-sectional EBSD mapping also enabled the precise quantification of the grain size variation across the specimen as shown in Figure 4.2 d. The average grain diameter variates from 1.8 to 1.6 μm for ~55% of the sample from the positive electrode side. From the negative electrode side, the grains show a bimodal microstructure where there are normal grains with ~2 μm diameter and there are abnormal grains with ~60 μm diameter. Our prior work has found this negative electrode side abnormal grain growth was due to the electrochemical induced grain boundary transitions. The reduced grain boundaries go through disorder-to-order transition that increased the grain boundary diffusivity and mobility.

Aside from the negative electrode side abnormal grain growth, it was also found that the Bi-rich phase could migrate towards the negative electrode driven by the electric field. The pristine sample showed homogeneous bismuth oxide distribution throughout the sample. After the field-assisted sintering experiment, the positive electrode side became essentially Bi-free after sufficiently long annealing under electric field as shown in Figure 4.1 a schematic diagram and Figure 4.1 c-f SEM images. There was no bright contrast Bi-rich phase near the positive electrode side of the specimen in Figure 4.1 c. Towards the middle section, the sample undergoes a transition near a porosity belt from Bi-free to Bi-rich at the ZnO grain boundaries as shown in Figure 4.1 d.

The Bi migration was further supported with low-magnification energy-dispersive X-ray spectroscopy mapping in Figure 4.2 b and the areal fraction of the bright contrast Bi-rich phase from SEM image in Figure 4.2 f. The EDS mapping showed 0 atomic% Bi on the positive electrode side, while the Bi signal was detected on the half side from the negative electrode. The quantification of the bright contrast Bi-rich phase across the specimen also show a sharp transition from Bi-free to Bi-rich near the porosity belt region, further showed the Bi migration towards the negative electrode driven by the electric field.

To further probe the grain boundary Bi content after the field-assisted sintering experiment, we examined the positive and negative electrode side grain boundary structure and elemental composition by aberration-corrected scanning transmission electron microscopy (AC STEM) and STEM EDS mapping. The TEM sample was prepared with focused ion beam (FIB), and the approximate FIB sample location were marked in the low-magnification SEM image in Figure 4.3 a, 3b, and 3e. The positive electrode side TEM sample was selected randomly across three ZnO grains (Figure 4.3 b), and the negative electrode side TEM sample was prepared at a grain boundary near an abnormal ZnO grain and normal ZnO grains (Figure 4.3 e). In the positive electrode side SEM image Figure 4.3 b and STEM HAADF image Figure 5.3c, no bright contrast Bi-rich phase was found between the ZnO grains. Nano-sized pores could be found at the ZnO grains triple-junctions in Figure 5.3c, which are likely caused by the removal of the Bi-rich phase. In contrast, no porosity could be found on the region near the negative electrode side, and the triple-junctions were filled with bismuth oxide secondary phase on both TEM level (Figure 4.3 g) and SEM level (Figure 4.7 e) magnification.

Upon zooming in on one of the grain boundaries near the positive electrode, the STEM HAADF image in Figure 5.3d shows no bright contrast was observed at GBs in the HAADF

images, indicating there is no bismuth oxide segregation at the ZnO GB. In comparison, the grain boundary near the negative electrode between an abnormal grain and a normal grain show an ordered bismuth oxide enriched intergranular film (Figure 4.3 g and Figure 4.3 e). STEM EDS was also carried out to further determine the GB elemental composition. As shown in Figure 4a and 4e, the EDS acquisition region was between two ZnO grains. The increased intensity for Bi was obvious for the grain boundary near the negative electrode, while there is no Bi signal detected for the GB near the positive electrode. The EDS line scan also indicates the Bi content increased to ~8 at% at the GB center. STEM EDS maps of two other GBs randomly selected from the positive and negative side are shown in Figure 4.6, which further supports the Bi-rich phase migration driven by the electric field.

Under a constant electric field, the gradient of the electrochemical potential can induce the migration of cations.[135] The driving force for transport in the x-direction is the electrochemical potential gradient of the ion

$$d\eta = d\mu + zfd\phi$$

where μ is the chemical potential, z is the electrical charge, and $d\phi$ is the electrical potential gradient. A similar field-induced cation migration in oxides was previously reported in $NiTO_3$, $(Co_xMg_{1-x})O$, and $BaTiO_3$. For example, it was found field-induced cation electrotransport could cause phase unmixing of $NiTiO_3$ into NiO and TiO_2 since Ni^{2+} has faster electrochemical mobility compared to Ti^{4+}; Ni was found enriched near the cathode side (same direction of the current), while anode side showed TiO_2 single phase. In the case of Bi_2O_3 – doped ZnO, there are two possible pathways for Bi migration: (1) lattice migration in ZnO and (2) grain boundary migration. At the specimen temperature of ~870 ºC, ~0.03 mol% of Bi_2O_3 can dissolve into the bulk ZnO grains.[136–138] Therefore, it can be hypothesized that the electric field induced chemical potential

gradients can drive $Bi_{Zn}^{\bullet}$ in bulk ZnO grains to migrate towards the negative electrode side. However, the low lattice solubility and bulk diffusion coefficient of Bi in ZnO [137,139] rule out the ZnO lattice as the major Bi migration pathway. The specimen consists of 0.5 mol% addition of Bi_2O_3, which is well above the Bi_2O_3 saturation in ZnO at ~870 ºC, so the majority of Bi_2O_3 exist as liquid phase between the ZnO grains at the experiment temperature. It is therefore more rational to understand the migration pathway through grain boundary transport. Previous experiments on pressure-segregation of Bi_2O_3 in ZnO showed rapid diffusion of Bi along the grain boundary allowed the de-segregated sample to fully saturate the grain boundaries in 10 min at 720 ºC ambient pressure. [137,139] In the present case, the electric field was found to drive the migration of Bi-enriched interfacial liquid within ZnO solid grains.

After the bismuth oxide phase migrated, the sample positive side changes into a Bi-free ZnO polycrystals. The Bi_2O_3 enriched grain boundaries in ZnO polycrystals are oxygen ion-conducting, while the undoped ZnO polycrystal is electron-conducting. Therefore, the positive side of the Bi_2O_3-doped ZnO region is oxidized, causing O_2 release and the generation of the porosity belt. On the other hand, the negative side are oxygen reduced and cause a grain boundary disorder-to-order transition, as shown in Figure 4.4 e. This ordered grain boundary can greatly increase the grain boundary mobilities and forming the abnormally large grains, which is in accordance with the previous study. [48]

Conclusion

This work shows that electric field can drive the migration of bismuth oxide liquid phase toward the negative electrode in Bi_2O_3-doped ZnO. The positive electrode side becomes Bi-free after sufficiently long annealing under electric field, and the observation was supported with low-magnification SEM/optical images and nanoscale AC-STEM characterization. This represents a

new finding of the electric field effects on ceramic microstructure evolution of the unique grain boundary ionic conducting systems. Electric field induced secondary phase migration can exist in other systems and alter microstructure evolution. This study suggests potential technological opportunities for novel ceramic grain boundary tailoring with electric field.

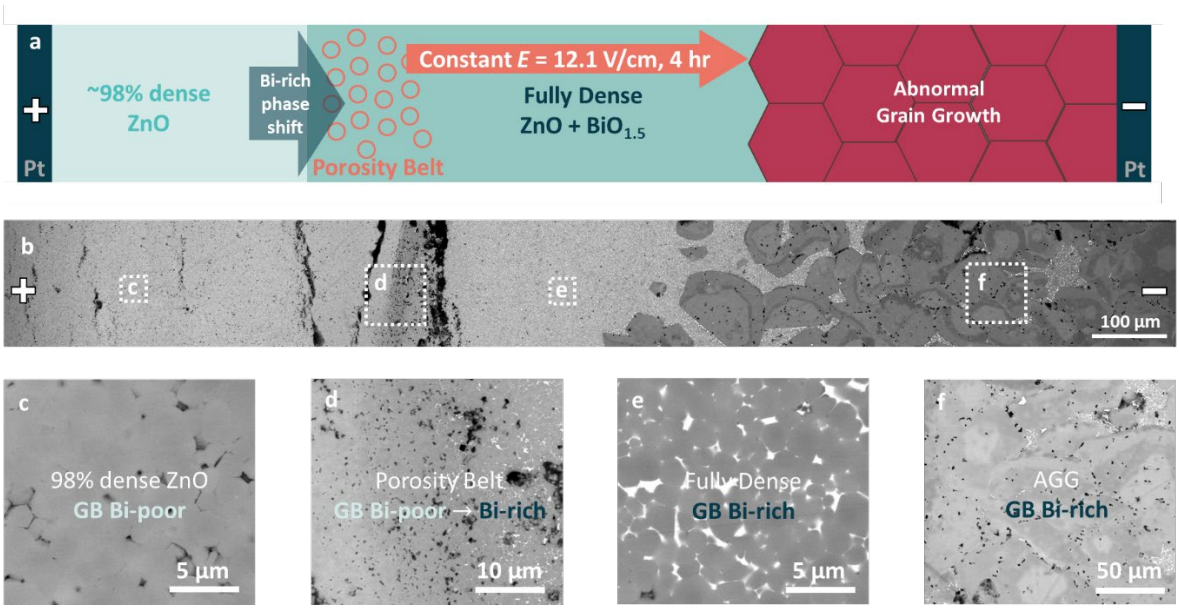

Figure 4.1 Microstructure of a Bi_2O_3-doped ZnO polycrystalline specimen annealed under an applied electric field (2 V over the specimen: ~12.1 V/cm and ~17.6 mA/mm^2). (a) A schematic illustration of the specimen showing the migration of the Bi-rich phase towards the cathode side, the formation of porosity belt, and abnormal grain growth at the cathode side. (b) Cross-sectional SEM image, showing the microstructure from anode to cathode side. (c) The region near the anode side consisted of 98% dense ZnO grains with no (bright contrast) Bi-rich secondary phase. (d) A porosity belt was observed away from the positive electrode. Bi-rich phase was observed to the right of the porosity belt (towards the negative electrode), indicating the migration of Bi-rich phase driven by the electric field. (e) The middle region was fully dense with a Bi-rich secondary phase. (f) Abnormal grain growth was observed near the cathode in the reduced region.

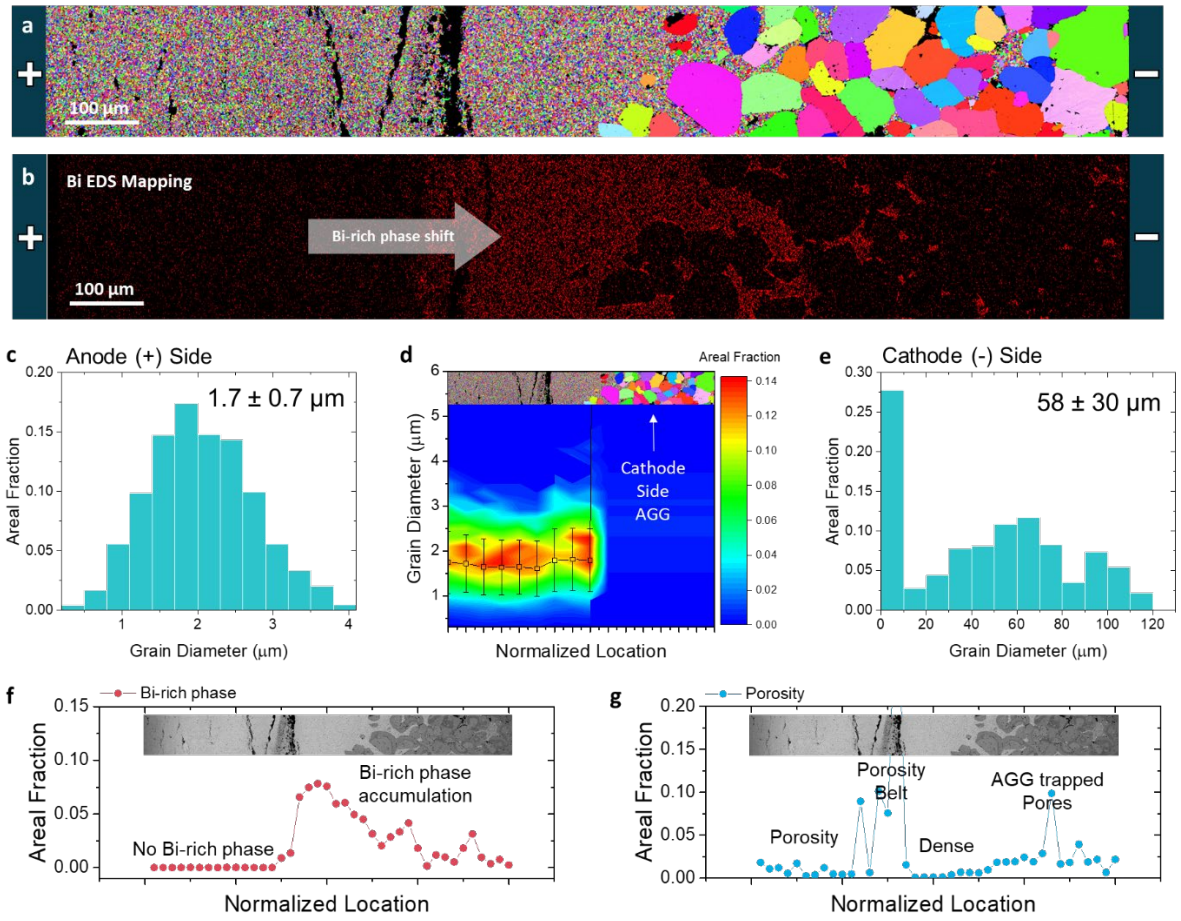

Figure 4.2 (a) EBSD maps (b) Bi EDS mapping of the Bi_2O_3-doped ZnO specimen annealed under an applied electric field. The grain diameter distribution at regions near (c) anode side and (e) cathode side. (d) Measured grain size distribution across the entire specimen. Measured areal fraction distribution across the specimen of (f) the Bi-rich secondary phase and (g) porosity.

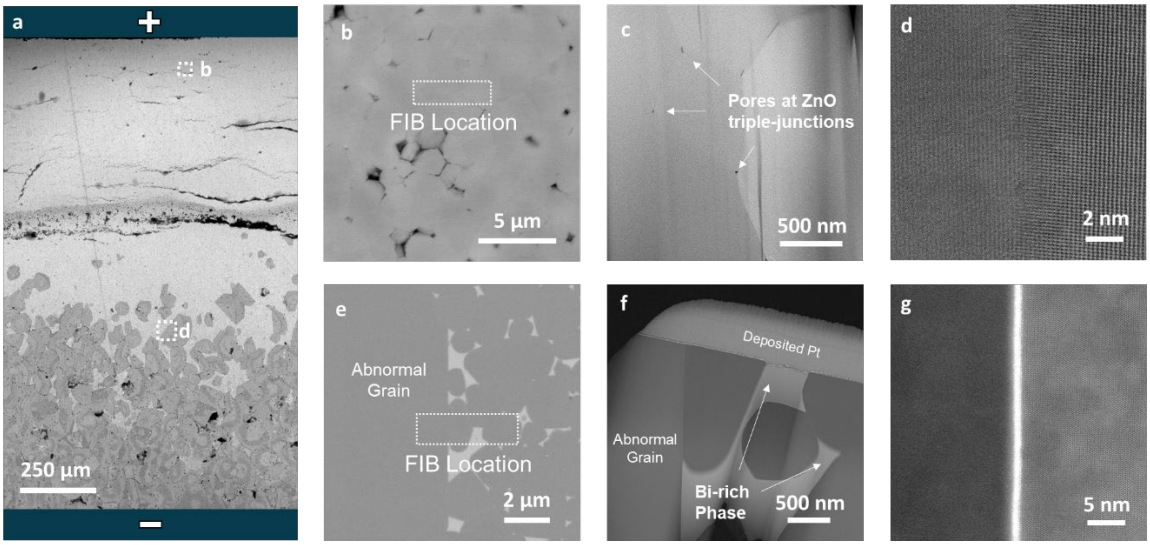

Figure 4.3 (a) Low-magnification SEM image showing the approximate FIB sample location near (b) the anode side and (e) the cathode side. Low-magnification STEM HAADF image of the grains near (c) the anode side and (f) the cathode side. Grain boundary high-magnification STEM HAADF image at (d) the anode side and (g) the cathode side. Near the anode side, no Bi-rich phase was observed, and some pores were found at ZnO triple-grain junctions

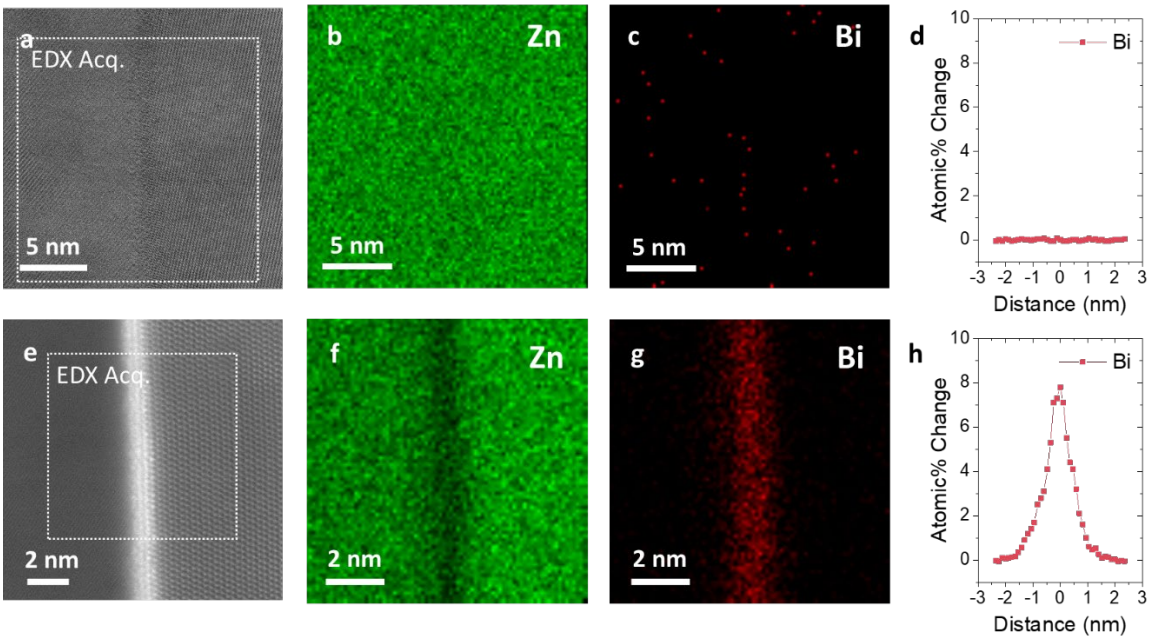

Figure 4.4 AC STEM energy-dispersive X-ray spectroscopy (EDS) mapping of the representative anode side and cathode side grain boundaries. STEM HAADF images and EDS mappings of (a) (b) (c) a Bi-free GB near the anode side and (e) (f) (g) a Bi-rich GB near the cathode side. Line profile across the GB on (d) anode side and (h) cathode side showing the changes in the atomic percentages of Bi with respect to the bulk composition.

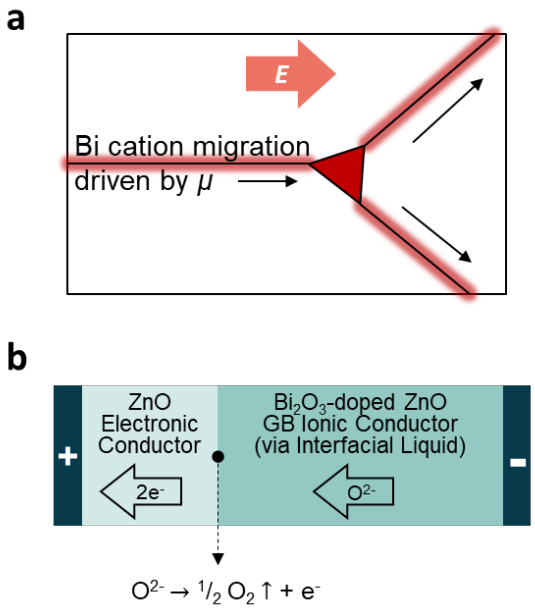

Figure 4.5 (a) A schematic illustration of the proposed Bi diffusion mechanism at a triple-junction of ZnO grains. The red lines indicate the Bi-rich GBs and the red triangle indicates the Bi-rich secondary phase at triple junction. At GB, the Bi-rich interfacial liquid moves, driven by the chemical potential gradient. (b) A schematic illustration of the Bi_2O_3-doped ZnO polycrystalline specimen annealed under an applied electric field. After the Bi migrated, the anode side changes to a ZnO electronic conductor while the cathode side is an ionic conductor (via interfacial liquid). The porosity belt observed at the electronic conductor – ionic conductor junction corresponds to the oxidation reaction that produces O_2.

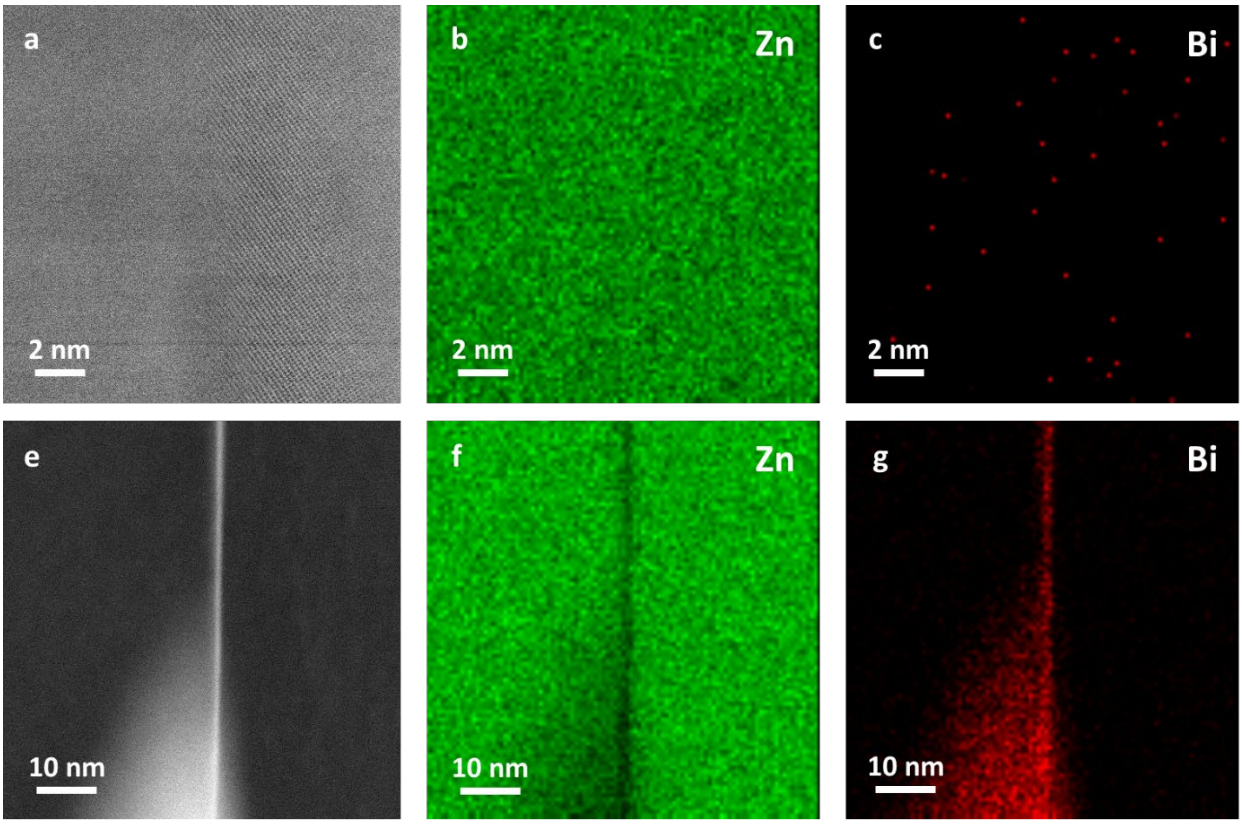

Figure 4.6 AC STEM energy-dispersive X-ray spectroscopy (EDS) mapping of the two additional representative anode side and cathode side grain boundaries. STEM HAADF images and EDS mappings of **(a) (b) (c)** a Bi-free GB near the anode side and **(e) (f) (g)** a Bi-rich GB near the cathode side.

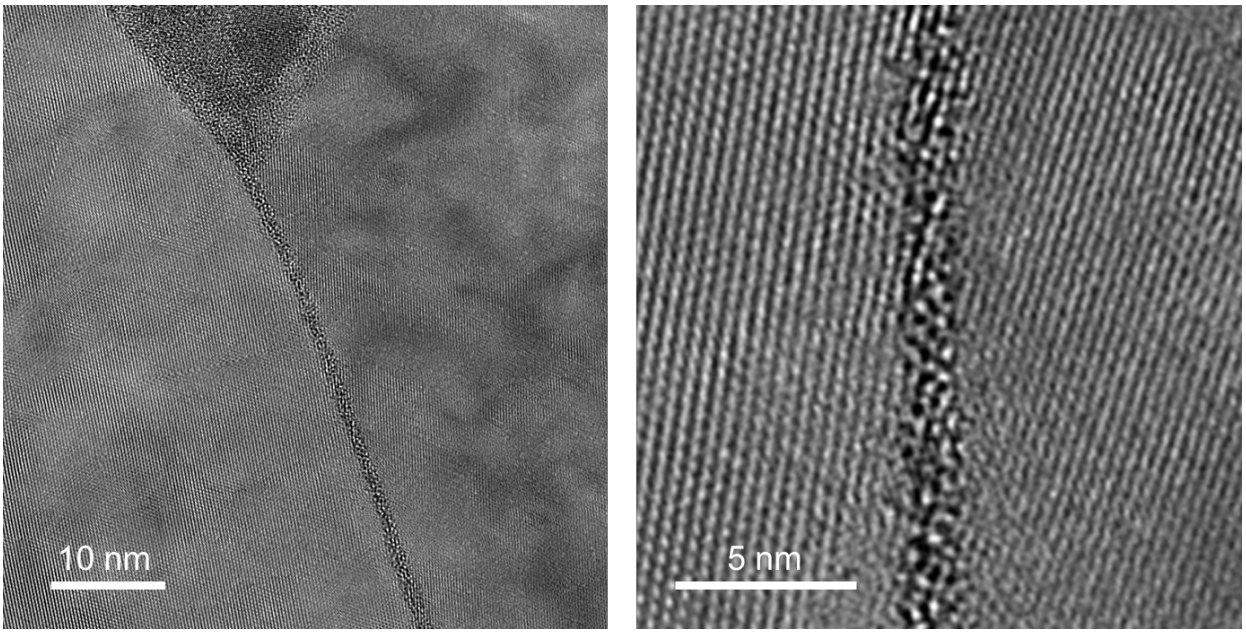

Figure 4.7 TEM images of a representative Bi-doped ZnO anode side grain boundary (right side of the porosity belt in Figure 4.1 a). The images show a disordered GB.

Acknowledgments

This work is supported by the Aerospace Materials for Extreme Environments program of the U.S. Air Force Office of Scientific Research (AFOSR) under the grants nos. FA9550-19-1-0327.

Chapter 4, in part, is a reprint of the material "Electric-Field-Assisted Bi Migration in Bi_2O_3-doped ZnO Polycrystalline Specimens", coauthored with J. Luo. It is currently being prepared for submission for publication of the material. The dissertation author was the primary researcher and author of this material.

Chapter 5. Ceramic Microstructure Control with Electric Field

Introduction

Electric fields and currents are crucial for innovative sintering technologies and energy storage applications.[29] In general, field-assisted ceramic sintering methods showed decreased temperature and sintering time compared to conventional processes. [30–32] Field-assisted sintering technology (FAST), or spark plasma sintering (SPS) was demonstrated as a versatile method to sinter high-temperature ceramics.[34–36] The rapid heating and sintering time are enabled with the current passing through the conductive die with uniaxial pressure. For flash sintering, the ultrafast densification (in seconds) at reduced sintering temperature is enabled by directly passing a current through the sample. More recently, an ultra-fast high-temperature sintering method was reported to densify ceramics in ~10 seconds with Joule-heating carbon strips.[39] For novel sintering processes, the externally applied electric fields can generate nonthermal effects that affect materials properties, such as microstructure changes[45,47,48], porosity migration[43,44], and facilitate phase transformation.[42] In energy storage applications, electric field also plays important role in solid electrolytes used in solid oxide fuel cells and solid-state batteries, where extreme fields can cause expedited degradation and device failure.[45]

On the atomic level, it was discovered that an applied electric field can change the microstructural evolution through an electrochemically induced GB transition.[48] In Bi_2O_3-ZnO, cathode side reduction was found to cause a GB disorder-to-order transition, and subsequently induces abnormal grain growth. Previous studies on grain boundaries proposed that GBs can be viewed as two-dimensional interfacial phases (complexions) that can have transitions to affect various materials properties.[74,87,140–142] It can be hypothesized that this electrochemically induced GB transition can exist in other systems and influence microstructural evolutions. Therefore,

understanding electric field effects on microstructure and material properties will not only improve existing field-assisted sintering processes, but also provide potential possibilities to tailor microstructure and other physical properties.

In this study, we use ZnO as a model system to demonstrate the feasibility of tailoring ceramic microstructure with electrical fields induced GB transformation. After sintering under a constant electric field, a gradual increase of grain size was observed from cathode to anode side, and the grain size gradient can be controlled with the electric field and sintering time. With spatially resolved photoluminescence spectroscopy mapping and defects chemistry calculation, we found electric field can induce defects polarization in ZnO and subsequently alter the GB structure. Based on the scanning transmission electron microscopy and ab initio molecular dynamics, the anode side GBs cores were enriched with zinc vacancies, and these V_{Zn}-rich GBs were calculated to have higher GB diffusivities. This work brings fundamental knowledge on both GB complexion (phase-like) transitions and electric field effects on microstructure, thereby pointing to a new direction of physical properties control via electrochemically induced GB transformation.

Method

ZnO powders (99.98% purity, 18 nm, US Nanomaterials) was first sintered into dense pellet with spark plasma sintering (SPS) at 840 ºC for 5 min under a uniaxial pressure of 50 MPa in vacuum (10^{-2} Torr) using a graphite die. The pellet was then annealing in air at 700 ºC for 9 hours for residual carbon removal, and reach >99% relative densities. The pellets were ground to around $4 \times 3 \times 1.5$ mm^3 and Pt was sputtered onto the two sides to form electrodes.

For the sintering experiment with electric field, an external DC current was applied across the sample while maintaining a constant voltage. The furnace temperature and sintering time are all

labeled with the corresponding sample. Tektronix DMM 4040 digital multimeters were used to record the current and electric potential readings.

The pellet cross-section microstructure was characterized with a scanning electron microscope (Apreo SEM, FEI) equipped with an Oxford Symmetry EBSD detector. The TEM lamellas were fabricated using a Thermo Scientific Scios dual-beam focused ion beam/SEM system. The atomic-level grain boundary structure was studied with a aberration-corrected electron microscope JEOL JEM-300CF operating at 300 kV.

To study the defects polarization of the sintered ZnO, spatially resolved photoluminescence spectroscopy was conducted on the sample cross-section on a Leica SP5 confocal microscope. The wavelength range was from 400 to 700 nm.

Creating and controlling graded microstructure

Using undoped ZnO as a model system, we successfully demonstrated the feasibility of creating and controlling graded microstructures via an applied electric field. An example of a graded microstructure created via annealing a ZnO polycrystalline specimen under an applied electric is shown in Figure 5.1. In this case, a constant voltage of 3.84 V was applied onto a dense polycrystal ZnO specimen under a furnace temperature of 600 ^{o}C for 4 h. Figure 5.1a shows the cross-section morphology of the specimen after the field-assisted sintering process. The ZnO grain sizes were found to gradually increase from the negative electrode to the positive electrode. Electron backscatter diffraction mapping was carried out to quantify the grain size variation across the specimen. The averaged grain diameters on the anode side were 7.4 ± 3.8 μm, which is about 5 times larger than the cathode side grain size of 1.0 ± 0.5 μm. Figure 5.1e further shows the continuous grain size variation from the cathode to the anode side. These large grain variations

across a 1.2 mm thick specimen cannot cause by the temperature gradient, since the sharp temperature transition is inconceivable for a homogeneous material.

The graded microstructure can also be controlled by changing the applied electric field as shown in Figure 5.1c and 5.1d. A smaller grain size variation was observed at a lower applied electric field of 20.2 V/cm at the same furnace temperature of 600 ºC. The anode side grain size decreased to 3.5 ± 1.72 μm. Due to the large contribution from Joule heating, the specimen temperature also decreased from ~1380 ºC to ~1214 ºC (estimated based on black body radiation). Figure 5.1d further illustrates an example of (true non-thermal) effect of changing electric field on altering the graded microstructures, where the specimen temperatures were kept similar by carefully tuning the furnace temperature to compensate for the decreased specimen temperature. At a similar sample temperature of ~1400 ºC and a lower applied electric field of ~24.3 V/cm, the anode side averaged grain diameter decreased to 4.0 ± 1.9 μm. These cases together showcase that the graded microstructure can be controlled via changing the applied electric field.

To further study the grain growth kinetics, the microstructure evolution of ZnO annealed under a constant electric field of 20.2 V/cm (total 2.8V) for the different duration was studied. Grain growth can be expressed using the equation:

$$d_t^n - d_0^n = kt \quad (1)$$

where d_t and d_0 are the grain size at time t and t = 0, respectively, n is the grain growth exponent, and k is a constant. For undoped ZnO, n = 3 was consistently observed in the previous grain growth studies[143,144], which indicates the growth occurs by volume diffusion. The constant k scales with the grain boundary mobility. The pristine dense ZnO specimen fabricated with spark plasma sintering showed a slightly larger grain sizes at the center of the specimen (1.3 ± 0.6 μm) compared to the surface regions (0.8 ± 0.3 μm). Increasing the annealing time under the same electric field

gradually increased grain sizes from the anode side, with little changes in grain sizes at the cathode side, as shown in Figure 5.2d. For the sample sintered for 32 hours under 20.2 V/cm electric field (Figure 5.2a), the anode side grain diameter increased to 4.8 ± 2.3 μm, which is much larger compared to the cathode side grain diameter (1.9 ± 0.9 μm). Using the anode and cathode side grain diameter at different sintering time in Figure 5.2e, the k constants that scales with grain boundary mobility can be calculated as shown in Figure 5.2f. The k constant on the anode side was fitted to be 3.8, which is more than 30 times greater than the cathode side k constant (0.11). This result indicates that the anode side grain boundary mobility was greatly enhanced during the sintering process with electric field.

Electric Field Induced Defects Polarization

To have a fundamental understanding on the mechanism for this anode side enhanced grain growth under electric field, the defect chemistry of ZnO need to be considered. In this study, we adopted the defect chemistry proposed by Tuller[145,146], where zinc interstitial was proposed as the predominant donor defect. Therefore, in our calculation we assume the Frenkel reaction ($Zn_{Zn} \leftrightarrow Zn_i^{\times} + V_{Zn}^{\times}$) predominates over the Schottky reaction ($Nil \leftrightarrow V_O^{\times} + V_{Zn}^{\times}$). Also, since the bulk oxygen tracer diffusivity is more than 2 orders of magnitude lower than the Zn tracer diffusivity[147,148], we further assumed oxygen as rigid sublattice, and only consider the migration of zinc cations for simplification.

During the field-assisted sintering experiment, ZnO is placed between two ion-blocking Pt electrodes, so there is no net ionic current at steady-state. The applied electric field drives Zn ion from anode to cathode and form a chemical potential gradient of Zn. The corresponding flux Ji can be calculated as the product of mobility and driving forces

$$j_i = -\frac{\sigma_i}{zF}\frac{d\eta_i}{dx} = -\frac{\sigma_i}{zF}\left(\frac{d\mu_i}{dx} + zF\frac{d\phi}{dx}\right) \quad (2)$$

where σ is electrical conductivity, z is the charge of the mobile specie, F is faraday constant, η is the electrochemical potential, μ is the chemical potential, and ϕ is the electric potential. Under room temperature in air, the two most abundant charged specie are electron and doubly charged zinc interstitial, and the charge neutrality is satisfied with $n = 2[Zn_i^{\cdot\cdot}]$. At steady-state, there is no ion flux due to the blocking electrodes. Therefore the boundary conditions of the sample with thickness l is $J_i(0,t) = J_i(l,t) = 0$, which gives

$$\frac{d\mu_i}{dx} = -2F\frac{d\phi}{dx} \tag{3}$$

or

$$\Delta\mu_i = -2F\Delta\phi \tag{4}$$

The zinc chemical potential change can represent a local P_{O2} change across the sample assume thermodynamic equilibrium is achieved. Subsequently, we can sketch the electric potential and the corresponding major carrier chemical potential. If we further assume the sample middle point P_{O2} is 0.2 atm (remain unchanged as in air), the chemical potential from the defect concentration change can be calculated from the equation

$$\Delta\mu_i = RTln\left(\frac{c_i'}{c_i''}\right) \tag{5}$$

where R is the gas constant, T is specimen temperature, and c_i is the defect concentration. For a total 3.8 V applied across the sample, the estimated defect concentration is shown in Figure 5.3f based on the quantitative Brouwer Diagram calculated from Tuller's defect chemistry model. Near the middle of the sample, the charge balance is being maintained between electrons and doubly ionized zinc interstitials. On the cathode side, the singly ionized zinc interstitials become dominate over the doubly charged ones when the local P_{O2} is smaller than 1×10^{-20} atm. Toward the anode side when the local P_{O2} is greater than 1×10^{5} atm, the singly charged zinc vacancy and hole become

dominate. Such transition from n-type electron conductor to p-type hole conductor upon the application of electric field was also discovered in previous studies.[45,149–151]

To probe the defect concentration across the sample, we used spatially resolved photoluminescence spectroscopy to quantify zinc vacancies across the ZnO sample annealed under a voltage of 3.8 V (E = 26.9 V/cm) for 4 h as shown in Figure 5.3a. For ZnO, zinc vacancies give rise to the green luminescence centered around 2.35 eV (530 nm).[152–154] The photoluminescence intensity mapping at the 530 nm wavelength clearly showed the increased intensity near the anode side indicating a higher zinc vacancies concentration towards the anode electrode. The trend can also be visualized via the heat map (Figure 5.3c), the extracted photoluminescence spectra (Figure 5.3d), and the spectra peak intensities (Figure 5.3e). The peak intensity of the green emission near the anode side is more than two times higher than the peak intensity near the cathode side (Figure 5.3d). The observed anode side zinc vacancies enrichment also matches the defects concentration estimation based on Tullers' defects chemistry model, which further verifies that electric field can induce defects polarization in ZnO.

Grain Boundary Oxidation Transition

To elucidate the atomic-level mechanism of the electric field induced anode side grain boundary mobility enhancement, the grain boundaries structures were examined with aberration-corrected scanning transmission electron microscopy (AC-STEM), in conjunction with energy dispersive X-ray spectroscopy (EDS). Three different GBs were characterized from both cathode and anode side of the ZnO specimen after sintering under an applied electric field of 3.8 V for 4 hours. Clean and stoichiometric GBs were observed for all three GBs on the cathode side as shown in the HAADF images from Figure 5.4b to 5.4d. No dark or bright contrast was observed near the GB region. In comparison, all three anode side GBs showed dark contrast as shown in Figure 5.4h

to 4j, which suggests Zn-depleted and O-rich GBs. AC-STEM EDS mapping was conducted to confirm the atomic composition of GBs. Figure 5.4i and 4m EDS atomic percentage mapping of anode side GBs further shows the grain boundary region is zinc poor and oxygen rich, which the cathode side GB appears to be stoichiometric (Figure 5.4h to 5.4j). The line profile was extracted across the GB showing the changes in oxygen atomic% as shown in Figure 5.4g and 5.4n. For the anode side GB, the O composition increased by ~11% at the grain boundary region compared to bulk region. In contrast, for the cathode side GB, there was no obvious change in oxygen and zinc composition across the GB. Combined with the photoluminescence results, it can be inferred that the electric field induced defects polarization can cause a preferential Zn vacancy segregation at the anode side grain boundaries.

Conclusion

In summary, we use ZnO as a model system to demonstrate the feasibility of tailoring ceramic microstructure with electrical fields induced GB transformation. After sintering under a constant electric field, a gradual increase of grain size was observed from cathode to anode side, and the grain size gradient can be controlled with the electric field and sintering time. Spatially resolved photoluminescence spectroscopy shows zinc vacancies enrichment near the anode side. Grain boundary STEM and EDS mapping further shows that the electric field induced defects polarization can cause a preferential Zn vacancy segregation at the anode side grain boundaries. This work brings fundamental knowledge on both GB complexion (phase-like) transitions and electric field effects on microstructure, thereby pointing to a new direction of physical properties control via electrochemically induced GB transformation.

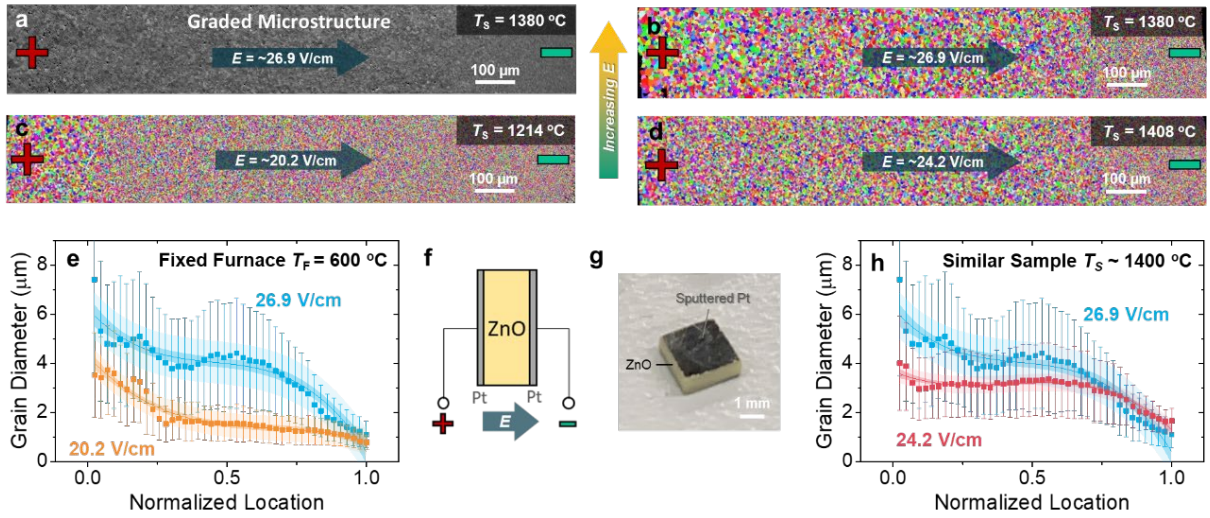

Figure 5.1. Creating and controlling graded microstructures with applied electric fields. (a) cross-section SEM image and (b) EBSD mapping of a ZnO specimen annealed under 26.9 V/cm electric field at a sample temperature of 1380 ºC, where a gradient in the grain size was observed. The graded microstructures can be altered by (c) changing electric field to 20.2 V/cm at a fixed furnace temperature of 600 oC, where the specimen temperatures were different due to the Joule heating) or (d) carefully selecting the conditions to keep similar specimen with 24.2 V/cm electric fields (to show true field effects). The detailed grain size distribution across the sample with (e) fixed furnace temperature, and (h) similar sample temperature. The error bar in the plot shows the standard deviation of the grain size in the corresponding section. (f) A schematic illustration of the experimental setup. (g) Image of a dense pristine ZnO specimen with the two surfaces sputtered with Pt as electrodes.

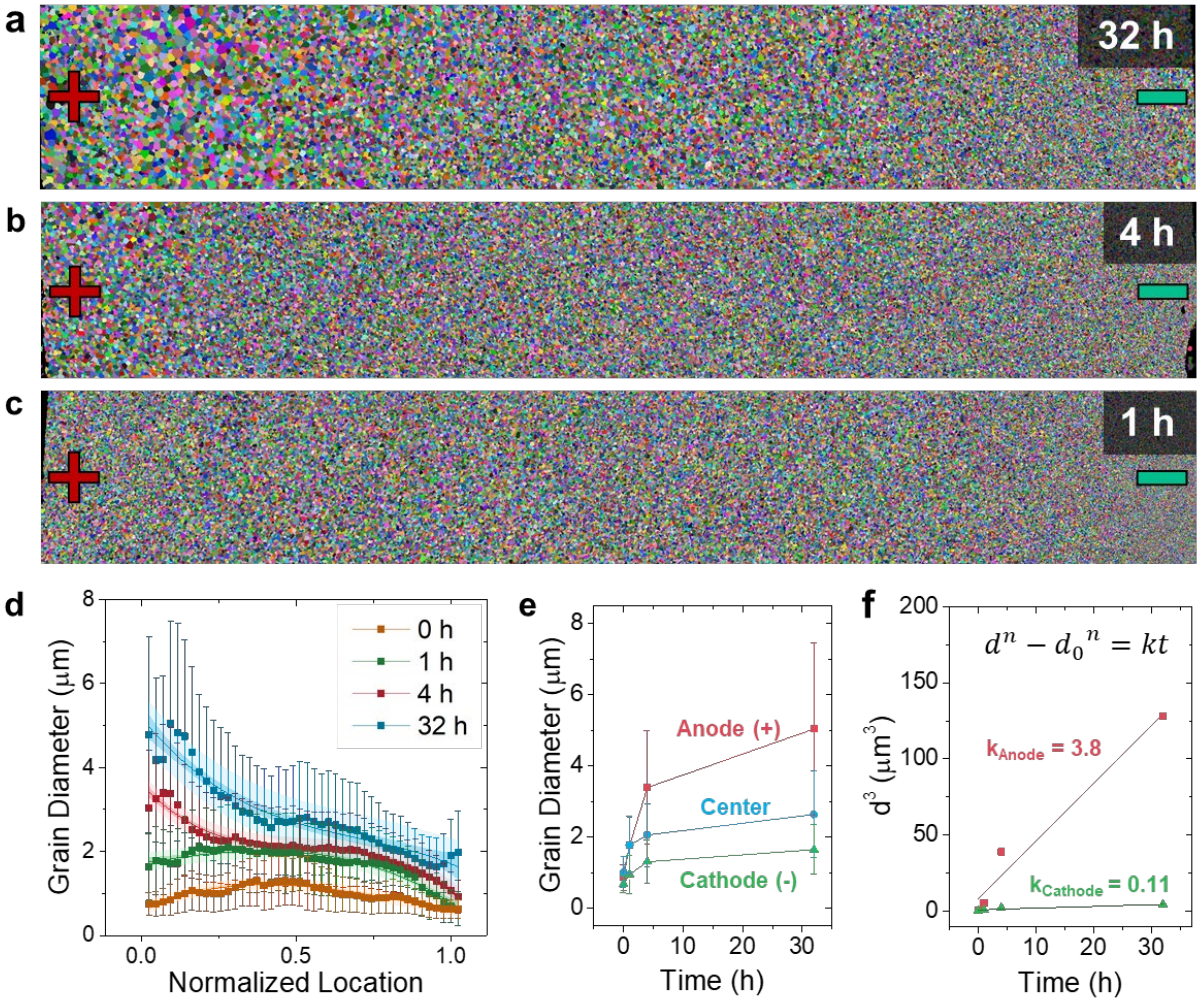

Figure 5.2. Kinetics study of the microstructural evolution of ZnO annealed under a electric field. EBSD maps of the ZnO specimen annealed for (a) 32 h, (b) 4 h, and (c) 1 h under a constant applied voltage of 2.8 V (E = 20.2 V/cm). (b) Grain size distribution of the ZnO specimens annealed for different durations under the same applied field. The error bar shows the standard deviation of the grain diameter of the corresponding section. (e) The averaged grain diameter of the anode side, center and the cathode side of the specimen sintered under the same field for different time periods. (f) Fitting of grain growth kinetics at the anode vs. cathode side, showing a > 30 x greater k at the anode side.

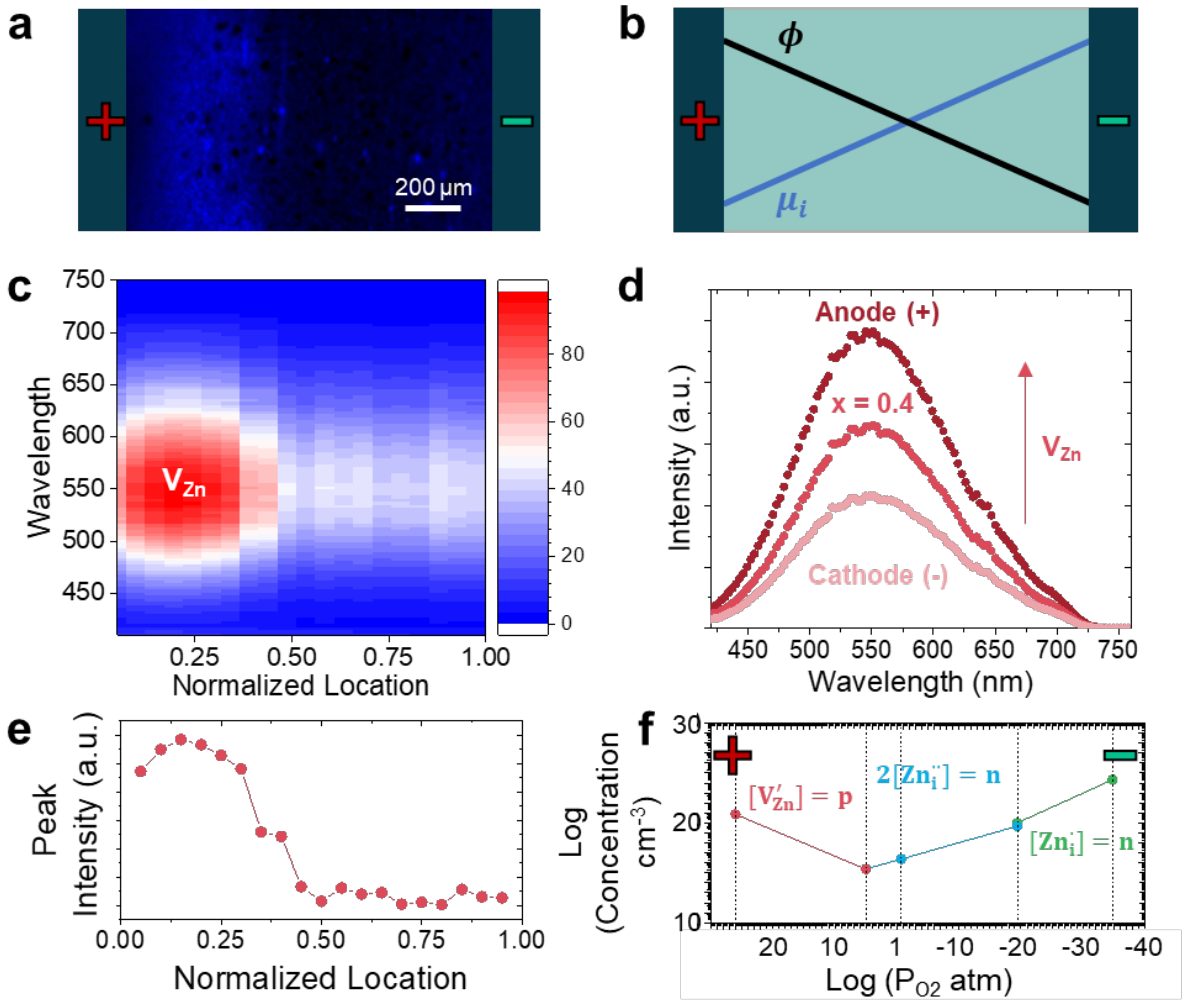

Figure 5.3. Photoluminescence spectroscopy of the ZnO annealed with a constant field, showing the enrichment of Zn vacancies in the anode region. (a) Photoluminescence intensity mapping at the 550 nm wavelength of the ZnO annealed under a voltage of 2.8 V (E = 20.2 V/cm) for 32 h. (c) heat map of the 20 integrated spectra across the sample (red: high intensity, blue: low intensity). (d) the photoluminescence spectra at anode, x=0.4 (out of 1 from anode side), and cathode side. (e) (e) the peak intensity of photoluminescence spectra across the sample.

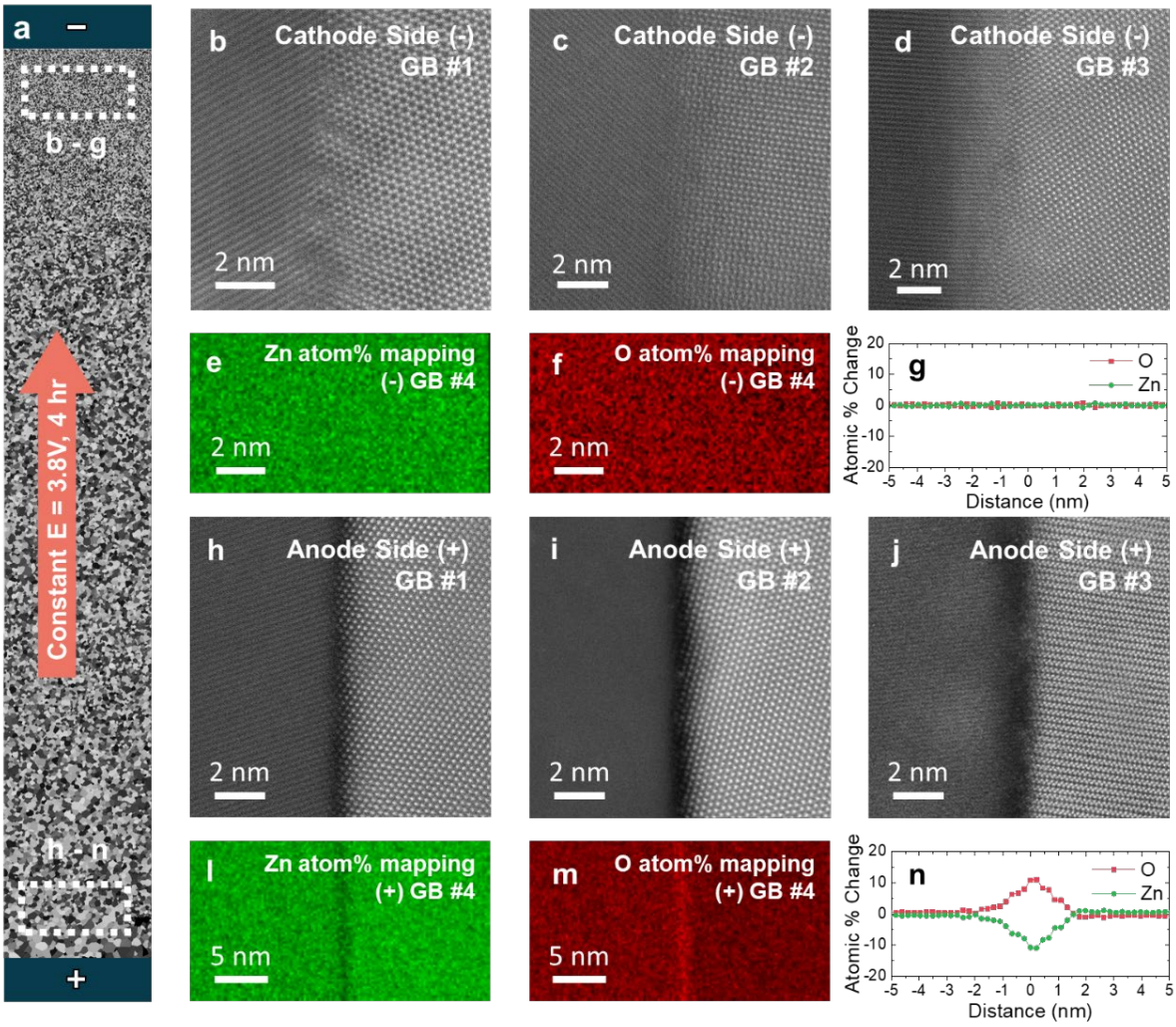

Figure 5.4. Aberration-corrected scanning transmission electron microscopy (AC STEM) high-angle annular dark-field (HAADF) images of representative cathode side and anode side grain boundaries (GBs). (a) An EBSD map showing the approximate location of the focused ion beam (FIB) sample site. Cathode (-) side GB (a) STEM HAADF image and (b) Zn and (c) O maps (in at%), showing stoichiometric GB. Anode (+) side GB (d) STEM HAADF image and (e) Zn and (f) O maps, showing oxygen-rich GB. (e), (g) Line profiles across (e) cathode side GB, and (i) anode side GB, showing the changes in the oxygen and zinc atomic percentages.

Acknowledgments

This work is supported by the Aerospace Materials for Extreme Environments program of the U.S. Air Force Office of Scientific Research (AFOSR) under the grants nos. FA9550-19-1-0327.

Chapter 5 contains unpublished material co-authored with J. Luo. The dissertation author was the primary author of this chapter.

Reference

(1) Dunn, B.; Kamath, H.; Tarascon, J.-M. Electrical Energy Storage for the Grid: A Battery of Choices. *Science (80-.).* **2011**, *334* (6058), 928–935. https://doi.org/10.1126/science.1212741.

(2) Armand, M.; Tarascon, J.-M. Building Better Batteries. *Nature* **2008**, *451* (7179), 652–657.

(3) Obrovac, M. N.; Chevrier, V. L. Alloy Negative Electrodes for Li-Ion Batteries. *Chem. Rev.* **2014**, *114* (23), 11444–11502. https://doi.org/10.1021/cr500207g.

(4) Park, C. M.; Kim, J. H.; Kim, H.; Sohn, H. J. Li-Alloy Based Anode Materials for Li Secondary Batteries. *Chem. Soc. Rev.* **2010**, *39* (8), 3115–3141. https://doi.org/10.1039/b919877f.

(5) Cook, J. B.; Detsi, E.; Liu, Y.; Liang, Y. L.; Kim, H. S.; Petrissans, X.; Dunn, B.; Tolbert, S. H. Nanoporous Tin with a Granular Hierarchical Ligament Morphology as a Highly Stable Li-Ion Battery Anode. *ACS Appl. Mater. Interfaces* **2017**, *9* (1), 293–303. https://doi.org/10.1021/acsami.6b09014.

(6) Yang, H.; Fan, F.; Liang, W.; Guo, X.; Zhu, T.; Zhang, S. A Chemo-Mechanical Model of Lithiation in Silicon. *J. Mech. Phys. Solids* **2014**, *70* (1), 349–361. https://doi.org/10.1016/j.jmps.2014.06.004.

(7) Huang, S.; Fan, F.; Li, J.; Zhang, S.; Zhu, T. Stress Generation during Lithiation of High-Capacity Electrode Particles in Lithium Ion Batteries. *Acta Mater.* **2013**, *61* (12), 4354–4364. https://doi.org/10.1016/j.actamat.2013.04.007.

(8) Sieradzki, K.; Corderman, R. R.; Shukla, K.; Newman, R. C. Computer Simulations of Corrosion: Selective Dissolution of Binary Alloys. *Philos. Mag. A* **1989**, *59* (4), 713–746.

(9) Pickering, H. W.; Wagner, C. Electrolytic Dissolution of Binary Alloys Containing a Noble Metal. *J. Electrochem. Soc.* **1967**, *114* (7), 698.

(10) Chen, Q.; Sieradzki, K. Spontaneous Evolution of Bicontinuous Nanostructures in Dealloyed Li-Based Systems. *Nat. Mater.* **2013**, *12* (12), 1102–1106. https://doi.org/10.1038/nmat3741.

(11) Wagner, M. R.; Raimann, P. R.; Trifonova, A.; Moeller, K.-C.; Besenhard, J. O.; Winter, M. Electrolyte Decomposition Reactions on Tin-and Graphite-Based Anodes Are Different. *Electrochem. Solid State Lett.* **2004**, *7* (7), A201.

(12) Park, A. R.; Park, C. M. Cubic Crystal-Structured SnTe for Superior Li- and Na-Ion Battery Anodes. *ACS Nano* **2017**, *11* (6), 6074–6084. https://doi.org/10.1021/acsnano.7b02039.

(13) Park, M. G.; Lee, D. H.; Jung, H.; Choi, J. H.; Park, C. M. Sn-Based Nanocomposite for Li-Ion Battery Anode with High Energy Density, Rate Capability, and Reversibility. *ACS Nano* **2018**, *12* (3), 2955–2967. https://doi.org/10.1021/acsnano.8b00586.

(14) Lee, D. H.; Park, C. M. Tin Selenides with Layered Crystal Structures for Li-Ion Batteries: Interesting Phase Change Mechanisms and Outstanding Electrochemical Behaviors. *ACS Appl. Mater. Interfaces* **2017**, *9* (18), 15439–15448. https://doi.org/10.1021/acsami.7b01829.

(15) Yan, Q.; Ko, S.-T.; Zhao, Y.; Whang, G.; Dawson, A.; Tolbert, S.; Dunn, B.; Luo, J. Cryogenic Milling Method to Fabricate Nanostructured Anodes. *ACS Appl. Energy Mater. 3* (11), 11285–11292. https://doi.org/10.1021/acsaem.0c02209.

(16) Cook, J. B.; Lin, T. C.; Detsi, E.; Weker, J. N.; Tolbert, S. H. Using X-Ray Microscopy to Understand How Nanoporous Materials Can Be Used to Reduce the Large Volume Change in Alloy Anodes. *Nano Lett.* **2017**, *17* (2), 870–877. https://doi.org/10.1021/acs.nanolett.6b04181.

(17) Detsi, E.; Petrissans, X.; Yan, Y.; Cook, J. B.; Deng, Z.; Liang, Y. L.; Dunn, B.; Tolbert, S. H. Tuning Ligament Shape in Dealloyed Nanoporous Tin and the Impact of Nanoscale Morphology on Its Applications in Na-Ion Alloy Battery Anodes. *Phys. Rev. Mater.* **2018**, *2* (5), 32–37. https://doi.org/10.1103/PhysRevMaterials.2.055404.

(18) Dalavi, S.; Guduru, P.; Lucht, B. L. Performance Enhancing Electrolyte Additives for Lithium Ion Batteries with Silicon Anodes. *J. Electrochem. Soc.* **2012**, *159* (5), A642.

(19) Zhang, Q.; Zhang, C.; Luo, W.; Cui, L.; Wang, Y.-J.; Jian, T.; Li, X.; Yan, Q.; Liu, H.; Ouyang, C.; Chen, Y.; Chen, C.-L.; Zhang, J. Sequence-Defined Peptoids with □OH and □COOH Groups As Binders to Reduce Cracks of Si Nanoparticles of Lithium-Ion Batteries. *Adv. Sci.* **2020**, *7* (18), 2000749. https://doi.org/https://doi.org/10.1002/advs.202000749.

(20) Philippe, B.; Dedryvère, R.; Gorgoi, M.; Rensmo, H.; Gonbeau, D.; Edström, K. Improved Performances of Nanosilicon Electrodes Using the Salt LiFSI: A Photoelectron Spectroscopy Study. *J. Am. Chem. Soc.* **2013**, *135* (26), 9829–9842. https://doi.org/10.1021/ja403082s.

(21) Zhang, J.; Xia, Y. Co-Sn Alloys as Negative Electrode Materials for Rechargeable Lithium Batteries. *J. Electrochem. Soc.* **2006**, *153* (8), A1466.

(22) Yao, H.; Zheng, G.; Li, W.; McDowell, M. T.; Seh, Z.; Liu, N.; Lu, Z.; Cui, Y. Crab Shells as Sustainable Templates from Nature for Nanostructured Battery Electrodes. *Nano Lett.* **2013**, *13* (7), 3385–3390. https://doi.org/10.1021/nl401729r.

(23) Kim, J. W.; Ryu, J. H.; Lee, K. T.; Oh, S. M. Improvement of Silicon Powder Negative Electrodes by Copper Electroless Deposition for Lithium Secondary Batteries. *J. Power Sources* **2005**, *147* (1–2), 227–233. https://doi.org/10.1016/j.jpowsour.2004.12.041.

(24) Antitomaso, P.; Fraisse, B.; Stievano, L.; Biscaglia, S.; Aymé-Perrot, D.; Girard, P.; Sougrati, M. T.; Monconduit, L. SnSb Electrodes for Li-Ion Batteries: The Electrochemical Mechanism and Capacity Fading Origins Elucidated by Using Operando Techniques. *J. Mater. Chem. A* **2017**, *5* (14), 6546–6555. https://doi.org/10.1039/C6TA10138K.

(25) Chao, S. C.; Song, Y. F.; Wang, C. C.; Sheu, H. S.; Wu, H. C.; Wu, N. L. Study on Microstructural Deformation of Working Sn and SnSb Anode Particles for Li-Ion Batteries by in Situ Transmission X-Ray Microscopy. *J. Phys. Chem. C* **2011**, *115* (44), 22040–22047. https://doi.org/10.1021/jp206829q.

(26) Kohandehghan, A.; Cui, K.; Kupsta, M.; Memarzadeh, E.; Kalisvaart, P.; Mitlin, D. Nanometer-Scale Sn Coatings Improve the Performance of Silicon Nanowire LIB Anodes. *J. Mater. Chem. A* **2014**, *2* (29), 11261–11279. https://doi.org/10.1039/c4ta00993b.

(27) Ye, J. C.; An, Y. H.; Heo, T. W.; Biener, M. M.; Nikolic, R. J.; Tang, M.; Jiang, H.; Wang, Y. M. Enhanced Lithiation and Fracture Behavior of Silicon Mesoscale Pillars via Atomic Layer Coatings and Geometry Design. *J. Power Sources* **2014**, *248*, 447–456. https://doi.org/10.1016/j.jpowsour.2013.09.097.

(28) Luo, J. Let Thermodynamics Do the Interfacial Engineering of Batteries and Solid Electrolytes. *Energy Storage Mater.* **2019**, *21*, 50–60.

(29) Kingery, W. D.; Bowen, H. K.; Uhlmann, D. R. *Introduction to Ceramics*; John wiley \& sons, 1976; Vol. 17.

(30) Reeja-Jayan, B.; Luo, J. Far-from-Equilibrium Effects of Electric and Electromagnetic Fields in Ceramics Synthesis and Processing. *MRS Bull.* **2021**, *46* (1), 26–35.

(31) Jha, S. K.; Raj, R. The Effect of Electric Field on Sintering and Electrical Conductivity of Titania. *J. Am. Ceram. Soc.* **2014**, *97* (2), 527–534. https://doi.org/10.1111/jace.12682.

(32) Jha, S. K.; Phuah, X. L.; Luo, J.; Grigoropoulos, C. P.; Wang, H.; García, E.; Reeja-Jayan, B. The Effects of External Fields in Ceramic Sintering. *J. Am. Ceram. Soc.* **2018**, jace.16061. https://doi.org/10.1111/jace.16061.

(33) Goetzel, C. G.; Demarchi, V. S. ELECTRICALLY ACTIVATED PRESSURE SINTERING OF TI POWDERS. PT. 2. *Powder Met Int* **1971**, *3* (3), 134–136.

(34) Grasso, S.; Sakka, Y.; Maizza, G. Electric Current Activated/Assisted Sintering (ECAS): A Review of Patents 1906--2008. *Sci. Technol. Adv. Mater.* **2009**, *10* (5), 53001.

(35) Guillon, O.; Gonzalez-Julian, J.; Dargatz, B.; Kessel, T.; Schierning, G.; Räthel, J.; Herrmann, M. Field-Assisted Sintering Technology/Spark Plasma Sintering: Mechanisms, Materials, and Technology Developments. *Adv. Eng. Mater.* **2014**, *16* (7), 830–849.

(36) Mamedov, V. Spark Plasma Sintering as Advanced PM Sintering Method. *Powder Metall.* **2002**, *45* (4), 322–328.

(37) Garay, J. E. Current-Activated, Pressure-Assisted Densification of Materials. *Annu. Rev. Mater. Res.* **2010**, *40*, 445–468.

(38) He, J.; Tritt, T. M. Advances in Thermoelectric Materials Research: Looking Back and Moving Forward. *Science (80-.).* **2017**, *357* (6358).

(39) Cologna, M.; Rashkova, B.; Raj, R. Flash Sintering of Nanograin Zirconia In< 5 s at 850 C. *J. Am. Ceram. Soc.* **2010**, *93* (11), 3556–3559.

(40) Lebrun, J.-M.; Hellberg, C. S.; Jha, S. K.; Kriven, W. M.; Steveson, A.; Seymour, K. C.; Bernstein, N.; Erwin, S. C.; Raj, R. In-Situ Measurements of Lattice Expansion Related to Defect Generation during Flash Sintering. *J. Am. Ceram. Soc.* **2017**, *100* (11), 4965–4970.

(41) Lebrun, J.-M.; Morrissey, T. G.; Francis, J. S. C.; Seymour, K. C.; Kriven, W. M.; Raj, R. Emergence and Extinction of a New Phase during On--off Experiments Related to Flash Sintering of 3 YSZ. *J. Am. Ceram. Soc.* **2015**, *98* (5), 1493–1497.

(42) Jha, S. K.; Lebrun, J. M.; Raj, R. Phase Transformation in the Alumina--Titania System during Flash Sintering Experiments. *J. Eur. Ceram. Soc.* **2016**, *36* (3), 733–739.

(43) Chen, I. W.; Kim, S. W.; Li, J.; Kang, S. J. L.; Huang, F. Ionomigration of Neutral Phases in Ionic Conductors. *Adv. Energy Mater.* **2012**, *2* (11), 1383–1389. https://doi.org/10.1002/aenm.201200011.

(44) Kim, S.-W.; Kang, S.-J. L.; Chen, I.-W. Ionomigration of Pores and Gas Bubbles in Yttria-Stabilized Cubic Zirconia. *J. Am. Ceram. Soc.* **2013**, *96* (4), 1090–1098. https://doi.org/10.1111/jace.12233.

(45) Dong, Y.; Wang, H.; Chen, I. W. Electrical and Hydrogen Reduction Enhances Kinetics in Doped Zirconia and Ceria: I. Grain Growth Study. *J. Am. Ceram. Soc.* **2017**, *100* (3), 876–886. https://doi.org/10.1111/jace.14615.

(46) Rheinheimer, W.; Fülling, M.; Hoffmann, M. J. Grain Growth in Weak Electric Fields in Strontium Titanate: Grain Growth Acceleration by Defect Redistribution. *J. Eur. Ceram. Soc.* **2016**, *36* (11), 2773–2780.

(47) Zhang, Y.; Jung, J. Il; Luo, J. Thermal Runaway, Flash Sintering and Asymmetrical Microstructural Development of ZnO and ZnO-Bi2O3 under Direct Currents. *Acta Mater.* **2015**, *94*, 87–100. https://doi.org/10.1016/j.actamat.2015.04.018.

(48) Nie, J.; Hu, C.; Yan, Q.; Luo, J. Discovery of Electrochemically Induced Grain Boundary Transitions. *Nat. Commun.* **2021**, *12* (1), 1–10.

(49) Ohtani, H.; Ishida, K. A Thermodynamic Study of the Phase Equilibria in the Bi-Sn-Sb System. *J. Electron. Mater.* **1994**, *23* (8), 747–755.

(50) Manasijević, D.; Vřešťál, J.; Minić, D.; Kroupa, A.; Živković, D.; Živković, Ž. Phase Equilibria and Thermodynamics of the Bi–Sb–Sn Ternary System. *J. Alloys Compd.* **2007**, *438* (1), 150–157. https://doi.org/https://doi.org/10.1016/j.jallcom.2006.08.021.

(51) Wang, C. T.; He, Y.; Langdon, T. G. The Significance of Strain Weakening and Self-Annealing in a Superplastic Bi–Sn Eutectic Alloy Processed by High-Pressure Torsion. *Acta Mater.* **2020**, *185*, 245–256. https://doi.org/https://doi.org/10.1016/j.actamat.2019.11.064.

(52) Pearson, C. E.; others. The Viscous Properties of Extruded Eutectic Alloys of Lead-Tin and Bismuth-Tin. *J. Inst. Met.* **1934**, *54* (1), 111–124.

(53) Campbell, C. E.; Kattner, U. R.; Liu, Z.-K. File and Data Repositories for Next Generation CALPHAD. *Scr. Mater.* **2014**, *70*, 7–11. https://doi.org/https://doi.org/10.1016/j.scriptamat.2013.06.013.

(54) Zhou, N.; Luo, J. Developing Grain Boundary Diagrams for Multicomponent Alloys. *Acta Mater.* **2015**, *91*, 202–216.

(55) Shi, X.; Luo, J. Developing Grain Boundary Diagrams as a Materials Science Tool: A Case Study of Nickel-Doped Molybdenum. *Phys. Rev. B* **2011**, *84* (1), 14105.

(56) Luo, J.; Shi, X. Grain Boundary Disordering in Binary Alloys. *Appl. Phys. Lett.* **2008**, *92* (10), 101901.

(57) Luo, J. Developing Interfacial Phase Diagrams for Applications in Activated Sintering and beyond: Current Status and Future Directions. *J. Am. Ceram. Soc.* **2012**, *95* (8), 2358–2371.

(58) Jeurgens, L. P. H.; Wang, Z.; Mittemeijer, E. J. Thermodynamics of Reactions and Phase Transformations at Interfaces and Surfaces. *Int. J. Mater. Res.* **2009**, *100* (10), 1281–1307.

(59) Yang, K.; Tang, J.; Liu, Y.; Kong, M.; Zhou, B.; Shang, Y.; Zhang, W.-H. Controllable Synthesis of Peapod-like Sb@C and Corn-like C@Sb Nanotubes for Sodium Storage. *ACS Nano* **2020**, *14* (5), 5728–5737. https://doi.org/10.1021/acsnano.0c00366.

(60) Liu, Z.; Yu, X. Y.; Lou, X. W.; Paik, U. Sb@C Coaxial Nanotubes as a Superior Long-Life and High-Rate Anode for Sodium Ion Batteries. *Energy Environ. Sci.* **2016**, *9* (7), 2314–2318. https://doi.org/10.1039/c6ee01501h.

(61) Guo, X.; Xie, X.; Choi, S.; Zhao, Y.; Liu, H.; Wang, C.; Chang, S.; Wang, G. Sb 2 O 3/MXene (Ti 3 C 2 T x) Hybrid Anode Materials with Enhanced Performance for Sodium-Ion Batteries. *J. Mater. Chem. A* **2017**, *5* (24), 12445–12452.

(62) Sengupta, S.; Mitra, A.; Dahiya, P. P.; Kumar, A.; Mallik, M.; Das, K.; Majumder, S. B.; Das, S. Investigation on Lithium Conversion Behavior and Degradation Mechanisms in Tin Based Ternary Component Alloy Anodes for Lithium Ion Batteries. *J. Alloys Compd.* **2017**, *721*, 236–248.

(63) Xie, J.; Song, W.; Zheng, Y.; Liu, S.; Zhu, T.; Cao, G.; Zhao, X. Preparation and Li-Storage Properties of SnSb/Graphene Hybrid Nanostructure by a Facile One-Step Solvothermal Route. *Int. J. Smart Nano Mater.* **2011**, *2* (4), 261–271.

(64) Yuan, Z.; Wang, L.; Wang, G.; Yang, Z.; Dong, L.; Yu, X. Composites of SnSb Nanoparticles Embedded in Porous Carbon Nanofibers Wrapped with Reduced Graphene Oxide for Sodium Storage. *ACS Appl. Nano Mater.* **2021**, *4* (1), 826–833.

(65) Du, Z.; Jiang, Z.; Guo, C. Thermodynamic Optimizing of the Li--Sn System. *Int. J. Mater.*

Res. **2006**, *97* (1), 10–16.

(66) Okamoto, H.; Okamoto, H. *Phase Diagrams for Binary Alloys*; ASM international Materials Park, OH, 2000; Vol. 44.

(67) Huggins, R. A. Lithium Alloy Negative Electrodes. *J. Power Sources* **1999**, *81*, 13–19.

(68) Dahn, J. R.; Courtney, I. A.; Mao, O. Short-Range Sn Ordering and Crystal Structure of Li4. 4Sn Prepared by Ambient Temperature Electrochemical Methods. *Solid State Ionics* **1998**, *111* (3–4), 289–294.

(69) Kim, T.; Choi, W.; Shin, H.-C.; Choi, J.-Y.; Kim, J. M.; Park, M.-S.; Yoon, W.-S. Applications of Voltammetry in Lithium Ion Battery Research. *J. Electrochem. Sci. Technol.* **2020**, *11* (1), 14–25.

(70) Bard, A. J.; Faulkner, L. R. *Electrochemical Methods: Fundamentals and Applications, 2nd Edition*; John Wiley \& Sons, Incorporated, 2000.

(71) Wang, J.; Fan, F.; Liu, Y.; Jungjohann, K. L.; Lee, W.; Mao, S. X.; Liu, X.; Zhu, T. Structural Evolution and Pulverization of Tin Nanoparticles during Lithiation-Delithiation Cycling. **2014**, *161* (11), 3019–3024. https://doi.org/10.1149/2.0041411jes.

(72) Weker, J. N.; Liu, N.; Misra, S.; Andrews, J. C.; Cui, Y.; Toney, M. F. In Situ Nanotomography and Operando Transmission X-Ray Microscopy of Micron-Sized Ge Particles. *Energy Environ. Sci.* **2014**, *7* (8), 2771–2777. https://doi.org/10.1039/c4ee01384k.

(73) Clarke, D. R. On the Equilibrium Thickness of Intergranular Glass Phases in Ceramic Materials. *J. Am. Ceram. Soc.* **1987**, *70* (1), 15–22.

(74) Dillon, S. J.; Tang, M.; Carter, W. C.; Harmer, M. P. Complexion: A New Concept for Kinetic Engineering in Materials Science. *Acta Mater.* **2007**, *55* (18), 6208–6218. https://doi.org/https://doi.org/10.1016/j.actamat.2007.07.029.

(75) Luo, J. Stabilization of Nanoscale Quasi-Liquid Interfacial Films in Inorganic Materials: A Review and Critical Assessment. *Crit. Rev. solid state Mater. Sci.* **2007**, *32* (1–2), 67–109.

(76) Luo, J.; Wang, H.; Chiang, Y.-M. Origin of Solid-State Activated Sintering in Bi2O3-Doped ZnO. *J. Am. Ceram. Soc.* **1999**, *82* (4), 916–920.

(77) Gupta, V. K.; Yoon, D.-H.; Meyer III, H. M.; Luo, J. Thin Intergranular Films and Solid-State Activated Sintering in Nickel-Doped Tungsten. *Acta Mater.* **2007**, *55* (9), 3131–3142.

(78) Dash, J. G. Surface Melting. *Contemp. Phys.* **1989**, *30* (2), 89–100.

(79) Yu, Z.; Cantwell, P. R.; Gao, Q.; Yin, D.; Zhang, Y.; Zhou, N.; Rohrer, G. S.; Widom, M.; Luo, J.; Harmer, M. P. Segregation-Induced Ordered Superstructures at General Grain Boundaries in a Nickel-Bismuth Alloy. *Science (80-.).* **2017**, *358* (6359), 97–101.

(80) Mukhopadhyay, A.; Sheldon, B. W. Deformation and Stress in Electrode Materials for Li-Ion Batteries. *Prog. Mater. Sci.* **2014**, *63* (January), 58–116. https://doi.org/10.1016/j.pmatsci.2014.02.001.

(81) Zhang, S.; Zhao, K.; Zhu, T.; Li, J. Electrochemomechanical Degradation of High-Capacity Battery Electrode Materials. *Prog. Mater. Sci.* **2017**, *89*, 479–521. https://doi.org/10.1016/j.pmatsci.2017.04.014.

(82) McDowell, M. T.; Lee, S. W.; Nix, W. D.; Cui, Y. 25th Anniversary Article: Understanding the Lithiation of Silicon and Other Alloying Anodes for Lithium-Ion Batteries. *Adv. Mater.* **2013**, *25* (36), 4966–4985. https://doi.org/10.1002/adma.201301795.

(83) Shariat, P.; Vastava, R. B.; Langdon, T. G. An Evaluation of the Roles of Intercrystalline and Interphase Boundary Sliding in Two-Phase Superplastic Alloys. *Acta Metall.* **1982**, *30* (1), 285–296. https://doi.org/10.1016/0001-6160(82)90068-2.

(84) Hubert, P. J.; Kathiresan, K.; Wakabayashi, K. Filler Exfoliation and Dispersion in Polypropylene/as-Received Graphite Nanocomposites via Cryogenic Milling. *Polym. Eng. Sci.* **2011**, *51* (11), 2273–2281. https://doi.org/10.1002/pen.22001.

(85) Xu, H.; Li, S.; Chen, X.; Zhang, C.; Liu, W.; Fan, H.; Yu, Y.; Huang, Y.; Li, J. Sn-Alloy Foil Electrode with Mechanical Prelithiation: Full-Cell Performance up to 200 Cycles. *Adv. Energy Mater.* **2019**, *9* (42). https://doi.org/10.1002/aenm.201902150.

(86) Yoon, M.; Dong, Y.; Hwang, J.; Sung, J.; Cha, H.; Ahn, K.; Huang, Y.; Kang, S. J.; Li, J.; Cho, J. Reactive Boride Infusion Stabilizes Ni-Rich Cathodes for Lithium-Ion Batteries. *Nat. Energy* **2021**, *6* (April). https://doi.org/10.1038/s41560-021-00782-0.

(87) Tang, M.; Carter, W. C.; Cannon, R. M. Grain Boundary Transitions in Binary Alloys. *Phys. Rev. Lett.* **2006**, *97* (7), 75502.

(88) Cantwell, P. R.; Tang, M.; Dillon, S. J.; Luo, J.; Rohrer, G. S.; Harmer, M. P. Grain Boundary Complexions. *Acta Mater.* **2014**, *62*, 1–48.

(89) Luo, J. Interfacial Engineering of Solid Electrolytes. *J. Mater.* **2015**, *1* (1), 22–32. https://doi.org/https://doi.org/10.1016/j.jmat.2015.03.002.

(90) Yan, Q.; Whang, G.; Wei, Z.; Ko, S.-T.; Sautet, P.; Tolbert, S. H.; Dunn, B. S.; Luo, J. A Perspective on Interfacial Engineering of Lithium Metal Anodes and Beyond. *Appl. Phys. Lett.* **2020**, *117* (8), 80504. https://doi.org/10.1063/5.0018417.

(91) Kayyar, A.; Qian, H.; Luo, J. Surface Adsorption and Disordering in LiFePO 4 Based Battery Cathodes. *Appl. Phys. Lett.* **2009**, *95* (22), 221905.

(92) Kang, B.; Ceder, G. Battery Materials for Ultrafast Charging and Discharging. *Nature* **2009**, *458* (7235), 190–193.

(93) Hu, T.; Yang, S.; Zhou, N.; Zhang, Y.; Luo, J. Role of Disordered Bipolar Complexions on

the Sulfur Embrittlement of Nickel General Grain Boundaries. *Nat. Commun.* **2018**, *9* (1), 1–10.

(94) Luo, J.; Cheng, H.; Asl, K. M.; Kiely, C. J.; Harmer, M. P. The Role of a Bilayer Interfacial Phase on Liquid Metal Embrittlement. *Science (80-.).* **2011**, *333* (6050), 1730–1733. https://doi.org/10.1126/science.1208774.

(95) Yu, Z.; Cantwell, P. R.; Gao, Q.; Yin, D.; Zhang, Y.; Zhou, N.; Rohrer, G. S.; Widom, M.; Luo, J.; Harmer, M. P. Segregation-Induced Ordered Superstructures at General Grain Boundaries in a Nickel-Bismuth Alloy. *Science (80-.).* **2017**, *358* (6359), 97–101. https://doi.org/10.1126/science.aam8256.

(96) Huang, J.; Liu, H.; Zhou, N.; An, K.; Meng, Y. S.; Luo, J. Enhancing the Ion Transport in LiMn1. 5Ni0. 5O4 by Altering the Particle Wulff Shape via Anisotropic Surface Segregation. *ACS Appl. Mater. Interfaces* **2017**, *9* (42), 36745–36754.

(97) Huang, J.; Luo, J. A Facile and Generic Method to Improve Cathode Materials for Lithium-Ion Batteries via Utilizing Nanoscale Surface Amorphous Films of Self-Regulating Thickness. *Phys. Chem. Chem. Phys.* **2014**, *16* (17), 7786–7798.

(98) Liu, Y.; Meirer, F.; Williams, P. A.; Wang, J.; Andrews, J. C.; Pianetta, P. {\it TXM-Wizard}: A Program for Advanced Data Collection~and Evaluation in Full-Field Transmission X-Ray Microscopy. *J. Synchrotron Radiat.* **2012**, *19* (2), 281–287. https://doi.org/10.1107/S0909049511049144.

(99) Endo, M.; Kim, C.; Nishimura, K.; Fujino, T.; Miyashita, K. Recent Development of Carbon Materials for Li Ion Batteries. *Carbon N. Y.* **2000**, *38* (2), 183–197. https://doi.org/10.1016/S0008-6223(99)00141-4.

(100) Dong, Z.; Zhang, R.; Ji, D.; Chernova, N. A.; Karki, K.; Sallis, S.; Piper, L.; Stanley Whittingham, M. The Anode Challenge for Lithium-Ion Batteries: A Mechanochemically Synthesized Sn-Fe-C Composite Anode Surpasses Graphitic Carbon. *Adv. Sci.* **2016**, *3* (4), 1–8. https://doi.org/10.1002/advs.201500229.

(101) Ferguson, P. P.; Le, D. B.; Todd, A. D. W.; Martine, M. L.; Trussler, S.; Obrovac, M. N.; Dahn, J. R. Nanostructured Sn30Co30C40 Alloys for Lithium-Ion Battery Negative Electrodes Prepared by Horizontal Roller Milling. *J. Alloys Compd.* **2014**, *595*, 138–141. https://doi.org/10.1016/j.jallcom.2014.01.159.

(102) Liu, N.; Lu, Z.; Zhao, J.; Mcdowell, M. T.; Lee, H. W.; Zhao, W.; Cui, Y. A Pomegranate-Inspired Nanoscale Design for Large-Volume-Change Lithium Battery Anodes. *Nat. Nanotechnol.* **2014**, *9* (3), 187–192. https://doi.org/10.1038/nnano.2014.6.

(103) Wang, B.; Li, X.; Zhang, X.; Luo, B.; Zhang, Y.; Zhi, L. Contact-Engineered and Void-Involved Silicon/Carbon Nanohybrids as Lithium-Ion-Battery Anodes. *Adv. Mater.* **2013**, *25* (26), 3560–3565. https://doi.org/10.1002/adma.201300844.

(104) Kim, H.; Cho, J. Superior Lithium Electroactive Mesoporous Si@Carbon Core-Shell

Nanowires for Lithium Battery Anode Material. *Nano Lett.* **2008**, *8* (11), 3688–3691. https://doi.org/10.1021/nl801853x.

(105) Mizutani, S.; Inoue, H. Anode Active Material Method of Manufacturing the Same and Nonaqueous Electrolyte Secondary Battery Using the Same, 2010.

(106) Fan, Q.; Chupas, P. J.; Whittingham, M. S. Characterization of Amorphous and Crystalline Tin-Cobalt Anodes. *Electrochem. Solid-State Lett.* **2007**, *10* (12), 274–278. https://doi.org/10.1149/1.2789418.

(107) Ferguson, P. P.; Martine, M. L.; George, A. E.; Dahn, J. R. Studies of Tin-Transition Metal-Carbon and Tin-Cobalt-Transition Metal-Carbon Negative Electrode Materials Prepared by Mechanical Attrition. *J. Power Sources* **2009**, *194* (2), 794–800. https://doi.org/10.1016/j.jpowsour.2009.05.031.

(108) Suryanarayana, C. Mechanical Alloying and Milling. *Prog. Mater. Sci.* **2001**, *46* (1–2), 1–184. https://doi.org/10.1016/S0079-6425(99)00010-9.

(109) Dhital, S.; Shrestha, A. K.; Gidley, M. J. Effect of Cryo-Milling on Starches: Functionality and Digestibility. *Food Hydrocoll.* **2010**, *24* (2–3), 152–163. https://doi.org/10.1016/j.foodhyd.2009.08.013.

(110) Devi, A. F.; Fibrianto, K.; Torley, P. J.; Bhandari, B. Physical Properties of Cryomilled Rice Starch. *J. Cereal Sci.* **2009**, *49* (2), 278–284. https://doi.org/10.1016/j.jcs.2008.11.005.

(111) Loick, C.; Gartz, D.; Wattebled, L.; Harren, J. Process for Producing Improved Absorbent Polymers by Means of Cryogenic Grinding. Google Patents 2014.

(112) Witkin, D. B.; Lavernia, E. J. Synthesis and Mechanical Behavior of Nanostructured Materials via Cryomilling. *Prog. Mater. Sci.* **2006**, *51* (1), 1–60. https://doi.org/10.1016/j.pmatsci.2005.04.004.

(113) Kumar, N.; Biswas, K. Cryomilling: An Environment Friendly Approach of Preparation Large Quantity Ultra Refined Pure Aluminium Nanoparticles. *J. Mater. Res. Technol.* **2019**, *8* (1), 63–74. https://doi.org/10.1016/j.jmrt.2017.05.017.

(114) He, T.; He, X.; Tang, P.; Chu, D.; Wang, X.; Li, P. The Use of Cryogenic Milling to Prepare High Performance Al2009 Matrix Composites with Dispersive Carbon Nanotubes. *Mater. Des.* **2017**, *114*, 373–382. https://doi.org/10.1016/j.matdes.2016.11.008.

(115) Li, J. L.; Xiong, Y. C.; Wang, X. D.; Yan, S. J.; Yang, C.; He, W. W.; Chen, J. Z.; Wang, S. Q.; Zhang, X. Y.; Dai, S. L. Microstructure and Tensile Properties of Bulk Nanostructured Aluminum/Graphene Composites Prepared via Cryomilling. *Mater. Sci. Eng. A* **2015**, *626*, 400–405. https://doi.org/10.1016/j.msea.2014.12.102.

(116) Yang, J.; Winter, M.; Besenhard, J. O. Small Particle Size Multiphase Li-Alloy Anodes for Lithium-Ionbatteries. *Solid state ionics* **1996**, *90* (1–4), 281–287.

(117) Seo, J. U.; Park, C. M. Nanostructured SnSb/MOx (M = Al or Mg)/C Composites: Hybrid Mechanochemical Synthesis and Excellent Li Storage Performances. *J. Mater. Chem. A* **2013**, *1* (48), 15316–15322. https://doi.org/10.1039/c3ta13972g.

(118) Whittingham, M. S. History, Evolution, and Future Status of Energy Storage. *Proc. IEEE* **2012**, *100* (SPL CONTENT), 1518–1534. https://doi.org/10.1109/JPROC.2012.2190170.

(119) Fecht, H. J. Nanostructure Formation by Mechanical Attrition. *Nanostructured Mater.* **1995**, *6* (1–4), 33–42. https://doi.org/10.1016/0965-9773(95)00027-5.

(120) Meyers, M. A.; Mishra, A.; Benson, D. J. Mechanical Properties of Nanocrystalline Materials. *Prog. Mater. Sci.* **2006**, *51* (4), 427–556. https://doi.org/10.1016/j.pmatsci.2005.08.003.

(121) Zhang, X.; Wang, H.; Narayan, J.; Koch, C. C. Evidence for the Formation Mechanism of Nanoscale Microstructures in Cryomilled Zn Powder. *Acta Mater.* **2001**, *49* (8), 1319–1326. https://doi.org/10.1016/S1359-6454(01)00051-9.

(122) Mohamed, F. A. A Dislocation Model for the Minimum Grain Size Obtainable by Milling. *Acta Mater.* **2003**, *51* (14), 4107–4119. https://doi.org/10.1016/S1359-6454(03)00230-1.

(123) Vigolo, B.; Penicaud, A.; Coulon, C.; Sauder, C.; Pailler, R.; Journet, C.; Bernier, P.; Poulin, P. Macroscopic Fibers and Ribbons of Oriented Carbon Nanotubes. *Science (80-.).* **2000**, *290* (5495), 1331–1334. https://doi.org/10.1126/science.290.5495.1331.

(124) Shaffer, B. M. S. P.; Windle, A. H. Fabrication and Characterization of Carbon Nanotube / Poly (Vinyl Alcohol) Composites **. **1999**, 937–941.

(125) Lee, J. H.; Marroquin, J.; Rhee, K. Y.; Park, S. J.; Hui, D. Cryomilling Application of Graphene to Improve Material Properties of Graphene/Chitosan Nanocomposites. *Compos. Part B Eng.* **2013**, *45* (1), 682–687. https://doi.org/10.1016/j.compositesb.2012.05.011.

(126) Omidi, M.; Khodabandeh, A.; Nategh, S.; Khakbiz, M. Wear Mechanisms Maps of CNT Reinforced Al6061 Nanocomposites Treated by Cryomilling and Mechanical Milling. *Tribol. Int.* **2017**, *110* (October 2016), 151–160. https://doi.org/10.1016/j.triboint.2017.01.033.

(127) Woo, D. J.; Hooper, J. P.; Osswald, S.; Bottolfson, B. A.; Brewer, L. N. Low Temperature Synthesis of Carbon Nanotube-Reinforced Aluminum Metal Composite Powders Using Cryogenic Milling. *J. Mater. Res.* **2014**, *29* (22), 2644–2656. https://doi.org/10.1557/jmr.2014.300.

(128) Xing, T.; Ramireddy, T.; Li, L. H.; Gunzelmann, D.; Zeng, H.; Qi, W.; Zhou, S.; Chen, Y. Lithium Storage in Disordered Graphitic Materials: A Semi-Quantitative Study of the Relationship between Structure Disordering and Capacity. *Phys. Chem. Chem. Phys.* **2015**, *17* (7), 5084–5089. https://doi.org/10.1039/c4cp05589f.

(129) Ferrari, A. C.; Robertson, J. Resonant Raman Spectroscopy of Disordered, Amorphous, and

Diamondlike Carbon. *Phys. Rev. B* **2001**, *64* (7), 75414. https://doi.org/10.1103/PhysRevB.64.075414.

(130) Ferrari, A. C.; Robertson, J. Interpretation of Raman Spectra of Disordered and Amorphous Carbon. *Phys. Rev. B* **2000**, *61* (20), 14095–14107. https://doi.org/10.1103/PhysRevB.61.14095.

(131) Azeez, A. A.; Rhee, K. Y.; Park, S. J.; Kim, H. J.; Jung, D. H. Application of Cryomilling to Enhance Material Properties of Carbon Nanotube Reinforced Chitosan Nanocomposites. *Compos. Part B Eng.* **2013**, *50*, 127–134. https://doi.org/10.1016/j.compositesb.2013.01.010.

(132) Miller Jr, P. H. The Electrical Conductivity of Zinc Oxide. *Phys. Rev.* **1941**, *60* (12), 890.

(133) Kul'bakin, I.; Belousov, V.; Fedorov, S.; Vorobiev, A. Solid/Melt ZnO--Bi2O3 Composites as Ion Transport Membranes for Oxygen Separation from Air. *Mater. Lett.* **2012**, *67* (1), 139–141.

(134) Zhang, Y.; Nie, J.; Luo, J. Flash Sintering Activated by Bulk Phase and Grain Boundary Complexion Transformations. *Acta Mater.* **2019**, *181*, 544–554.

(135) Schmalzried, H. *Chemical Kinetics of Solids*; John Wiley \& Sons, 2008.

(136) Safronov, G. M. Equilibrium Diagram of the Bismuth Oxide-Zinc Oxide System. *Russ. J. Inorg. Chem.* **1971**, *16*, 460–461.

(137) Lee, J.-R.; Chiang, Y.-M.; Ceder, G. Pressure-Thermodynamic Study of Grain Boundaries: Bi Segregation in ZnO. *Acta Mater.* **1997**, *45* (3), 1247–1257.

(138) Luo, J.; Chiang, Y. M. Equilibrium-Thickness Amorphous Films on { 11$\bar{2}$0 } Surfaces of Bi2O3-Doped ZnO. *J. Eur. Ceram. Soc.* **1999**, *19* (6–7), 697–701. https://doi.org/10.1016/s0955-2219(98)00299-4.

(139) Wang, H.; Chiang, Y.-M. Thermodynamic Stability of Intergranular Amorphous Films in Bismuth-Doped Zinc Oxide. *J. Am. Ceram. Soc.* **1998**, *81* (1), 89–96.

(140) Cantwell, P. R.; Tang, M.; Dillon, S. J.; Luo, J.; Rohrer, G. S.; Harmer, M. P. Grain Boundary Complexions. *Acta Mater.* **2014**, *62* (1), 1–48. https://doi.org/10.1016/j.actamat.2013.07.037.

(141) Kaplan, W. D.; Chatain, D.; Wynblatt, P.; Carter, W. C. A Review of Wetting versus Adsorption, Complexions, and Related Phenomena: The Rosetta Stone of Wetting. *J. Mater. Sci.* **2013**, *48* (17), 5681–5717.

(142) Baram, M.; Chatain, D.; Kaplan, W. D. Nanometer-Thick Equilibrium Films: The Interface between Thermodynamics and Atomistics. *Science (80-.).* **2011**, *332* (6026), 206–209.

(143) Senda, T.; Bradt, R. C. Grain Growth in Sintered ZnO and ZnO-Bi2O3 Ceramics. *J. Am.*

Ceram. Soc. **1990**, *73* (1), 106–114.

(144) GUPTA, T. K.; COBLE, R. L. Sintering of ZnO: I, Densification and Grain Growth. *J. Am. Ceram. Soc.* **1968**, *51* (9), 521–525. https://doi.org/10.1111/j.1151-2916.1968.tb15679.x.

(145) Wuensch, B. J.; Tuller, H. L. Lattice Diffusion, Grain Boundary Diffusion and Defect Structure of Zno. *J. Phys. Chem. Solids* **1994**, *55* (10), 975–984. https://doi.org/10.1016/0022-3697(94)90117-1.

(146) Han, J.; Mantas, P. Q.; Senos, A. M. R. Defect Chemistry and Electrical Characteristics of Undoped and Mn-Doped ZnO. *J. Eur. Ceram. Soc.* **2002**, *22* (1), 49–59. https://doi.org/10.1016/S0955-2219(01)00241-2.

(147) Erhart, P.; Albe, K. First-Principles Study of Migration Mechanisms and Diffusion of Oxygen in Zinc Oxide. *Phys. Rev. B - Condens. Matter Mater. Phys.* **2006**, *73* (11), 1–9. https://doi.org/10.1103/PhysRevB.73.115207.

(148) Erhart, P.; Albe, K. Diffusion of Zinc Vacancies and Interstitials in Zinc Oxide. *Appl. Phys. Lett.* **2006**, *88* (20), 201918.

(149) Dong, Y.; Chen, I. W. Electrical and Hydrogen Reduction Enhances Kinetics in Doped Zirconia and Ceria: II. Mapping Electrode Polarization and Vacancy Condensation in YSZ. *J. Am. Ceram. Soc.* **2018**, *101* (3), 1058–1073. https://doi.org/10.1111/jace.15274.

(150) Dong, Y.; Chen, I. W. Oxygen Potential Transition in Mixed Conducting Oxide Electrolyte. *Acta Mater.* **2018**, *156*, 399–410. https://doi.org/10.1016/j.actamat.2018.06.014.

(151) Dong, Y.; Chen, I. Mobility Transition at Grain Boundaries in Two-step Sintered 8 Mol% Yttria-stabilized Zirconia. *J. Am. Ceram. Soc.* **2018**, *101* (5), 1857–1869. https://doi.org/10.1111/jace.15362.

(152) McCluskey, M. D.; Jokela, S. J. Defects in ZnO. *J. Appl. Phys.* **2009**, *106* (7). https://doi.org/10.1063/1.3216464.

(153) Schmidt-Mende, L.; MacManus-Driscoll, J. L. ZnO - Nanostructures, Defects, and Devices. *Mater. Today* **2007**, *10* (5), 40–48. https://doi.org/10.1016/S1369-7021(07)70078-0.

(154) Janotti, A.; Van De Walle, C. G. Fundamentals of Zinc Oxide as a Semiconductor. *Reports Prog. Phys.* **2009**, *72* (12). https://doi.org/10.1088/0034-4885/72/12/126501.